Quantum Optoelectronic Detection and Mixing in the Nanowire Superconducting Structure

by

Zhizhong Yan

A thesis
presented to the University of Waterloo
in fulfillment of the
thesis requirement for the degree of
Doctor of Philosophy
in
Electrical and Computer Engineering

Waterloo, Ontario, Canada, 2009

I hereby declare that I am the sole author of this thesis. This is a true copy of the thesis, including any required final revisions, as accepted by my examiners.

I understand that my thesis may be made electronically available to the public.

Abstract

The recent advancement of superconducting nano devices has allowed for making a Superconducting Nanowire Single Photon Detector (SNSPD), whose extraordinary features have strongly motivated the research community to exploit it in many practical applications. In this thesis, an experimental setup for testing the SNSPD has been established. It contains an in-house packaging that meets the requirements of RF/microwave and optoelectronic characterizations. The quantum efficiency and detection efficiency measurements have confirmed that our approach is satisfactory. The dark count performance has reached the anticipated level. The factors affecting rise and fall times of the photoresponses are addressed.

Based on the successful setup, the characterizations including dc, small signal ac measurements have been undertaken. The measurements are aimed at quantitatively investigating Cooper pair density in the superconducting nanowire. The experimental method involves a two-step, small signal S-parameter measurement either in the presence or absence of optical powers. The subsequent measurements by varying the temperature and dc bias current have achieved remarkable understanding on the physical properties of SNSPD nanowires. Then, the electrically induced nonlinearity is studied via the large signal RF & microwave measurements. The experiments are a set of one-tone and two-tone measurements, in which either the RF driving power is varied at a fixed frequency, or vice versa. Two major nonlinear microwave circuit analysis methods, i.e. time-domain transient and hybrid-domain harmonic balance analysis, are employed. The simulation result reveals the optimized conditions of reaching the desired nonlinearity.

Finally, we have successfully measured the optoelectronic mixing products in an electrically pumped optoelectronic mixer, which has identical structures as that of the SNSPD. The experiments confirm that this mixer is not only sensitive to the classical light intensities, but also to that of the single photon level. Meanwhile, the quantum conversion matrices is derived to interpret the quantum optoelectronic mixing effects.

Acknowledgements

First my deep appreciation goes to my supervisor, Professor A. Hamed Majedi. I sincerely feel grateful for his persistent support, friendship, encouragement, trust and stimulating discussions. His insightful advices has led me to many research achievements, invaluable opportunities and experience.

I am strongly indebted to Professor Safieddin Safavi-Naeini, who has been my mentor, Co/supervisors, for his keen encouragement, concern during and beyond the period.

I sincerely thank Professor Xuemin (Sherman) Shen, my current co-supervisor who has constantly given me invaluable encouragement and general advice.

I would like to express my sincere appreciation to Professor Sujeet K. Chaudhuri for a lot of insightful advice and invaluable help during my entire course of PhD studies.

I also express my special acknowledgement to my committee member, Professor Adrian Lupascu, who is pleased to take the post from Professor Gregor Weihs, my internal-external comprehensive examiner. Special thanks to my external examiner, Professor John S. Preston. I deeply acknowledge all of them to spend their valuable time on my thesis defense.

Much of the experimental results in this thesis could not have been achieved without the consistent and professional technical help: from Michael Ditty of Institute for Quantum Computing; from undergraduate lab of electrical and computer engineering department, special thanks to Laura Winger for her prompt coordination with the testing equipment; from Bill Jolley, Centre for Integrated RF Engineering (CIRFE); from Denis Grégoire and Jean-Marc Moreau, and Nicola Gill, of Agilent Technologies Canada Inc, for their expertise in the field and generosity of lending the expensive equipment, which are so all critical to the success of the experiments.

I sincerely thank the staff members from Electrical and Computer Engineering, Wendy Boles, Lisa Szepaniak, Annette Dietrich, and Anne Jenson, and all; and Institute for Quantum Computing, Lorna Kropf, Wendy Reibel, Andrew Dale, and all, for their warm and prompt assistance.

Many thanks to my colleagues at Integrated Quantum Optoelectronic Lab, Jean-Luc Orgiazzi and Haig Atikian for sharing their expertise and offering assistance during the entire experimental stage; to Jayran Amirloo, Mohsen Keshavarz Akhlaghi, Hamid Reza Mohebbi, and Behnood Ghamsari for useful discussions and collaborations.

I acknowledge the partial financial support from Ontario Graduate Scholarship, and Institute for Quantum Computing, and University of Waterloo.

No word can exactly describe my deepest gratitude to my family. It is my greatest fortune to have my extraordinarily amazing, nice wife, Tao Xiao, who has given and is giving me unconditional love, unwavering support, and considerate understanding. I would like to express my deep gratitude to my dear mother and father. I would also like to say special thanks to my mother-in-law and father-in-law for their help, encouragement and understanding to my beloved wife and myself.

Lastly, many thanks to all my dear friends, their persistent support and encouragements in the past eight years. It were them who have accompanied with me in my long journey at University of Waterloo.

Dedication

To my forever beloved grandmother

Contents

List of Tables

List of Figures

List of Symbols

α	The heat transfer coefficient $\alpha(W/m^2 \cdot K)$
α_0	The temperature exponential for low temperature superconductors
β	The total dc and ac current bias ratio with respect to I_c^{GL}
β_a	The ac bias current ratio with respect to I_c^{GL}
β_b	The dc bias current ratio with respect to I_c
β_d	The dc bias current ratio with respect to I_c^{GL}
β_i	The relative current amplitude of the $i-th$ harmonic to that of bulk critical current
χ	The Cooper pair velocity ratio to its maximum velocity $\frac{v_s}{v_m}$
χ_0	The hotspot size of a 1-D superconducting wire
$\Delta(T)$	The temperature dependent BCS energy gap
$\delta(t-t_0)$	The Dirac Delta function
Δ_0	The BCS energy gap at zero temperature in the absence of optical power
η_n	The thermal healing length of a 1-D normal state wire
η_S	The thermal healing length of a 1-D superconducting wire

η_{eff} The system level quantum efficiency for photo induced current

$\Gamma_2(t)$ The transient reflection coefficient from the TL load port

Γ The one port complex reflection coefficient

γ The figure of merit of the thin film quality

$\Gamma(t)$ The real transient reflection coefficient in the time domain

γ_0 The normal state electron specific heat

$\hbar$ The reduced Planck Constant

λ_o The optical penetration depth

λ The wavelength of electrical or optical electromagnetic wave

λ_0 The superconducting penetration depth

Λ_k The kinetic inductivity of a superconducting wire

λ_L The London superconducting penetration depth

λ_{GL} The Ginsburg-Landau superconducting penetration depth

μ The nonequilibrium chemical potential

μ_0 The permeability of free-space($= 4\pi \times 10^{-7}\ H \cdot m^{-1}$)

ω_d The damped resonance frequency

ω_o The undamped LC resonance frequency

$\Phi(t)$ The total kinetic inductance flux stored in the $L_k(t)$

ρ_{20K} The normal state resistivity at 20 K temperature

ρ The amplitude of the complex reflection coefficient Γ

ρ_n The normal state resistivity

τ_{eff}^{QP} The effective quasiparticle lifetime

τ_d The superconducting energy gap relaxation time

θ The phase angle of the complex reflection coefficient Γ

$\tilde{L}_k^n$ The n-th Fourier expansion term of the $L_k(t)$

$\tilde{V}_o(\omega)$ The Fourier transform of $V_o(t)$

$\wp(t)$ The time varying optical power

ξ_0 The superconducting coherent length

$\zeta(T)$ The nonequilibrium gap parameter ratio

A The cross section area of the nanowire

a_0 The granular size of the NbN thin film

$b_1(t)$ The time domain reflection measured by a 50 Ω equipment

C_{ph} The phonon specific heat

d The thickness of SNSPD nanowire

DE The detection efficiency of the SNSPD

DQE The device level quantum efficiency

f_1 The electrical pumping frequency to the optoelectronic mixer in some ten MHz

f_2 The optical modulation or repetition rate frequency in hundreds of MHz

f_{opt} The optical carrier frequency in several hundreds of THz

$g_1(t)$ The input power from source into TL

h Planck Constant $6.628 \times 10^{-34}\ J \cdot \sec$

$h\,(t-t_0)$ The Heaviside function

$i_b(t)$ The total bias current including both dc and ac contributions

I_b The dc bias current to a SNSPD

I_c The critical current of SNSPD, also called zero voltage maximum current

I_c^{GL} The critical current for the bulk superconducting material

$I_{ph}\,(t)$ The transient photocurrent induced in the SNSPD nanowires

I_{ret} The return current of SNSPD

J_c The critical current density of superconducting nanowire

k_B The Boltzmann constant $1.3806503 \times 10^{-23}\ m^2 \cdot kg \cdot s^{-2} \cdot K^{-1}$

L The length of one segment of SNSPD nanowire

l The total length of the SNSPD nanowire

L_k The total kinetic inductance of the superconducting nanowire

$L_k^{'}$ The normalized kinetic inductance

L_m The magnetic inductance of SNSPD

L_{k0} The zero bias static total kinetic inductance of a SNSPD

$L_{k2n}^{'}$ The $2n^{th}$ order expansion of the nonlinear L_k

L_{TL} The total length of a transmission line connecting the SNSPD to the measurement equipment

l_{tr} The mean free path

m_e the mass of the normal electron (9.1×10^{-31}) kg

$n_\mu\,(T)$ The nonequilibrium Cooper pair density at a given temperature

N_Φ The photon density in the superconducting volume V

N_s The normalized Cooper pair density

n_s^T The initial Cooper pair density without bias current

n_{s0} The Cooper pair density at zero temperature in the absence of optical power

Q Quality factor of the equivalent RLC resonant circuitry

q_e The electron charge 1.6×10^{-19} C

QE The quantum efficiency of photon detector

R_n Room temperature SNSPD normal state total resistance

R_s Superconducting state SNSPD equivalent serial resistance induced by quasi-particle tunneling

R_{s0} The maximum resistance under a given temperature and a given input power range

$S_{TL}(t)$ The time domain two-port TL S-parameter matrix

T_b The ambient temperature

T_c Superconductor critical temperature

T_c' The reduced critical temperature

V The volume of the nanowire

$V_i(t)$ The input RF ac signal applied to the nonlinear load of TL from the source

v_m The maximum velocity for the Cooper pair current flow

$V_o(t)$ The simulated intrinsic photoresponse

$V_o^{L_k}$ The reflected harmonics induced solely by a sinusoidal current flowing in L_k

$V_o'(t)$ The reverse Fourier transformation of extrinsic photoresponse including unideal TL effect

$V_s(t)$ The absorbed photon induced voltage source

v_s The moving velocity for the Cooper pair current flow

v_{ph} The phase velocity of TEM mode wave propagating along the TL

V_{si} The one tone excitation amplitude

w The width of SNSPD nanowire

Z_0 The characteristic impedance of transmission line

Z_d The intrinsic impedance of the free space

$\mathbf{I}_S$ The current vector for the driving source subnetwork in Harmonic-Balance Analysis

$\mathbf{I}_L$ The current vector for the linear subnetwork in Harmonic-Balance Analysis

$\mathbf{I}_{NL}$ The current vector for the nonlinear subnetwork in Harmonic-Balance Analysis

Chapter 1

Introduction

The discovery of superconductivity in 1911 by H. Kamerlingh Onnes [1] has opened a new era of research, which is aimed at understanding the fundamental physics and potential applications of superconductors. Low transition temperature superconductors (LTS) can be well accounted for by Bardeen-Cooper-Shrieffer (BCS) microscopic theory [2] four decades after. In the middle of 1980's, some alloy of rare earth elements exhibits transition temperatures in the liquid nitrogen temperatures ($\sim$ 77 K), namely high temperature superconductors (HTS). LTS and HTS are mainly used in two fields: first, high current applications such as NMR magnets; Second, electronic devices such as infrared and millimeter wave detectors [3].

Superconducting electronic devices and circuits have found abundant applications by the introduction of a variety of junctions, such as superconducting to normal state junctions (SNS) [4]; and superconducting insulator superconducting junctions, or Josephson Junction [5]. The latter junctions are widely used in (1) rapid single flux quantum logic ICs [6]-[7]; (2) superconducting qubits including flux [8], charge [9] and phase qubits [10]-[11]. These qubits are quantum two level systems [12], and can be scaled up by being fabricated on a integrated circuit chip [13]-[14]; (3) The junction structure has also led to a large number of successful devices in microwave and optoelectronic applications, including parametric amplifiers [15]-[20], millimeter wave detectors/mixers [21]-[23], hot electron bolometer

detectors [24]-[26].

In the recent decade, a junction-less superconducting photon detector have been achieved by using NbN meander lines, thanks to the progress on nanofabrication technologies that allows for fabricating superconducting nano devices [27]. In 2001, an ultra thin NbN superconducting meander line has exhibited remarkable sensitivity as an optical single photon detector [28]-[29]; particularly when they reduced the film thickness to about 4 nm, the best superconducting single photon detector (SSPD) showed up to 30% Quantum Efficiency (QE) [30] for 1310 nm wavelength photons at 4.2 K. Considering nano-metric size in a SSPD [31]-[32], hereafter we refer SSPD to Superconducting Nanowire Single Photon Detector (SNSPD) for the entire scope of this thesis. In the following section, we will undertake a brief survey on different types single photon detectors. These devices show great potential applications in single and entangled photon source characterization, quantum metrology and quantum key distribution (QKD) [33].

1.1 An Overview of Single Photon Detectors

So far, Single Photon Detectors (SPD) have found applications in astronomy [34]-[35], biology and biochemistry [36]-[37], VLSI quality control to scan and debug semiconducting chips by detecting hot-electron radiations from the deep submicron channel of transistors [38]-[39]; telecommunication wavelength (1.3-1.55 μm) photon-counting detectors in optical communication links [40]; Quantum Key Distribution (QKD) for quantum communications [41]-[42] and linear optics quantum computation [43].

The SPDs can be classified by the materials they are made with, including semiconductor, e.g. Si, Ge or InGaAs, Avalanche Photon Diodes (APDs); Superconducting SPDs, such as: superconducting transition edge photon detectors [44]-[46]; superconducting kinetic-inductance detectors [47]; superconducting tunneling junction detectors (Tungsten) [48]-[49]; Superconducting Nanowire Single

Table 1.1: The comparison of all types of the single photon detector made of different materials (in which 'Semi' denotes semiconductor, 'Alk' denotes Alkali metal, and 'Sup' denotes superconductor), measured at wavelength $\lambda = 1.3$ μm.

Detector Model	Counting rate (Hz)	QE (%)	Jitter (ps)	Dark counts (s^{-1})	NEP ($W \cdot Hz^{-1/2}$)	Type
InGaAs (APD)(Fujitsu)	1×10^6	~ 20	$> 10^2$	$\sim 6 \times 10^3$	$\sim 10^{-17}$	Semi
R5509-43 PMT (Hamamatsu)	9×10^6	1	150	$\sim 1.6 \times 10^4$	$\sim 10^{-16}$	Alk
SPCM-AQR-16 Si-APD(EG&G)	5×10^6	0.01	350	25	$\sim 10^{-16}$	Semi
Mepsicron-II (Quantar)	1×10^6	0.001	100	0.1	NA	Semi
Al S-TJD	5×10^3	60	NA	NA	NA	Sup
W S-TES (NIST)	2×10^4	> 16	NA	< 0.001	$< 10^{-19}$	Sup
SNSPD (current)	2×10^9	> 30	18	< 0.01	$< 10^{-18}$	Sup
SNSPD (projected)	30×10^9	~ 50	< 18	< 0.001	$< 10^{-21}$	Sup

Photon Detector [32]; and vacuum Photomultiplier Tubes (PMTs). Table 1.1 lists these typical SPDs and compares their performances in terms of counting rate, QE, jitter time and noise equivalent power (NEP).

Table 1.2 compares two major categories of SPDs that are widely used for single photon and entangled photon counting systems. Semiconductor (e.g. Si or InGaAs) APDs exhibit longer recovery time, resulting in only a few MHz counting rate [34, 37]. The slower counting speed can prevent the Quantum Communication (QC) from achieving higher transfer bandwidth [41]. Superconducting photodetectors, on the other hand, require very low operating temperature, but they both have much wider sensitive wavelength range than their semiconducting counterparts; and their dark count rate is extremely low.

Table 1.2: The comparison of main superconducting and semiconducting SPDs, collected from ref. [22, 50, 51]

	Semiconducting SPDs		Superconducting SPDs	
Detectors	Si	InGaAs	SNSPD (NbN)	TES (W)
Temperatures (K)	300	200	$2 \sim 4.2$	0.1
Wavelength (μm)	0.25-1.1	1.1-1.8	0.4-5.6	0.1-5
Time resolution (ps)	48	~ 300	18	3×10^5
Quantum efficiency	25%@0.7μm	14%@1.54μm	6%@1.54μm	$> 80\%$@1.5μm
Apertures (μm)	200	30-80	SM fiber [1]	SM fiber
Dark count rates (cps)	$< \times 10^4$	$> 3 \times 10^4$	< 1	< 0.001
Data rate	$<$ 3 MHz	<15MHz	$\cong$ 2GHz	$\sim$ 20 KHz
Counting dynamic range ($\#h\nu$)	1-3000	NA	$> 10^8$	50
Electrical quenching	Yes (0.3 ns)	Yes (0.3 ns)	No	No
Photon number resolving	Limited	No	No [2]	Yes
Ruggedness	Very high	High	Low	Low
Yield	High	Low	Very low	Very low

[1] SM fiber is the telecom wavelength single mode (SM) fiber.

[2] Here we only consider the SNSPD as a single element/segment structure. Therefore, it does not exhibit photon number resolving capability when operated in the conventional dc current bias mode.

The comparison shows that semiconducting SPDs can work at higher temperatures, but their dark count rate is high; and their sensitive wavelength spectra is limited by their bandgap structures, leading to a narrower optical spectral bandwidth. Although InGaAs SPDs can detect photons of wavelengths up to 1.8 μm, they suffer from high dark count rates even in the cryogenic temperature range. In contrast, SNSPDs have drawn considerable attention because of their particular characteristics of high counting rates, low phase jitters, low dark counts[53]-[54], and loose constraint on operating temperature compared to the TES photon detectors [44]-[46]. Despite the advantages of superconducting SPDs, their active area can only be coupled to the size of SM fiber core, whose diameter is less than 10 μm; in addition, both of their yield are rather low, resulting in the excessive cost for the manufacture.

Due to these desirable features of the SNSPD, tremendous efforts have been dedicated to it recently. Here we try to summarizes them in the following fields: (1) increasing SNSPD system QE at 1550 nm wavelength by integrating an optical resonating cavity [52], or increasing optical coupling by employing an optical traveling waveguide [55]. (2) developing its photon number resolving by using multi-segment and multi-element micro structures [56]-[57]. (3) fabricating larger active area SNSPDs on MgO substrate [58]-[59]; (4) seeking fast rising and falling time and GHz counting possibility [32, 60]. (5) expanding SNSPD sensitive wavelength range [61]. In general, all of above approaches strongly require the nanofabrication facilities and high quality NbN thin films. More importantly, less state of the art electrical engineering approaches are directly involved. In this PhD work, we are making alternative attempts to solve the remaining problems by extensively taking advantage of RF/microwave and photonic technologies, such as electrically pumped optoelectronic mixing.

1.2 Motivations and Challenges

As we can see from Table 1.2, in the range of telecommunication wavelengths, SNSPDs demonstrate much higher data rates and lower dark counts. They become very promising to improve the performance of S-APD QKD system [62]. To vastly implement SNSPDs in a practical system, at least two technical challenges have to be overcome. First, the raw SNSPD has to be prepared ready and friendly for end users; Second, high QE SNSPD must be readily available.

Therefore, the main motivation is to establish an experimental setup that allows us to perform optoelectronic characterization of a raw SNSPD device. This entails a packaging solution to fulfill the cryogenic, optical and electrical requirements. The entire setup should have standard fiber optical interface to admit photon flux, and read out electronics for photon counting.

To combat the constrictions geometrically [63] and non-geometrically [64] imposed by the fabrication that limit QE of a given SNSPD, one can use a quantum optoelectronic mixer as a novel photon detection scheme, in which a strong electrical RF pumping is applied in conjunction with high dc bias. In the mixer, a nonzero ac voltage can drive the device into quasiparticle conduction state, which facilitates their tunneling through the constrictions or barriers in the device. Those barriers are considered to be one major form of the constrictions that impose the QE limitation to the SNSPD.

Three steps are required to reach the goal. First, the nonlinearity of superconducting nanowire must be measured and studied by varying dc bias, temperature and the optical power of a cw irradiation. The achievement of this step forms the initial understanding of superconducting Cooper pair static nonlinearity. Second, we need to study the electrically induced strong nonlinearity by applying high power RF signals in the forms of single-tone and two-tone sinusoids. By performing RF power level scan, and inspecting the higher orders of harmonic and mixing products, we can obtain knowledge to achieve strong nonlinearity. Such nonlinearity will be suitable for maximizing the mixing effects in the nanowire. Third, by combining the

results from the first two steps, we will be able to find a proper condition that leads to an electrically pumped optoelectronic mixing effect. Varying the temperature, dc and ac bias conditions, we anticipate to discover the specific set of conditions, on which single photon optoelectronic mixing can be achieved.

1.3 Organization of This Thesis

After the overview of superconducting detection technologies and the motivation of the PhD project, we then elaborate our approach to conduct optoelectronic characterization in the quantum optical regime in chapter two.

In chapter three, we report on the weak signal RF/microwave measurement in conjunction with dc characterization, perform the measurement in the presence and absence of the optical irradiation. The quantum regime described by μ^* model and bolometric regime are identified by varying the temperature. The effective T_c is introduced to reflect the optical heating.

In chapter four, we have performed a large signal RF measurement to test the nonlinearity of the nanowire. The single tone and two tone measurement were conducted. We attempt to use nonlinear microwave circuit analysis methods, i.e. time domain transient simulation; and time-frequency hybrid domain harmonic balance method. We compared our both simulation approaches to the experimental measurements.

In chapter five, we mainly exploit the results from the preceding chapters to conduct optoelectronic mixings. We use conversion matrices analyzing approach, and quantum superconducting kinetic photocurrent theory. The experimental results confirm that the optoelectronic mixing products are indeed generated by the strong nonlinear RF pumping power, and the weak photocurrents proportional to incoming photon numbers are induced by the single optical photons. In the last chapter, the concluding remarks and potential future works will be mentioned.

Chapter 2

SNSPD Packaging and Optoelectronic Characterization

Single photon optical detectors become highly on-demand not only to exploit quantum nature of the light but also to reach the ultimate sensitivity limit in any optical measurements. The SNSPD has been already used to perform these tasks, e.g. characterization of single photon sources [65]-[67] and non-invasive VLSI chip testing. SNSPD is a potential candidate for applications in fiber optical Quantum Key Distribution (QKD) [68] and ultra-high-speed communication as they are unique so far due to their high speed, low dark count rate and low timing jitter. The high speed makes them to be the best choice for high rate secret key distribution systems [30]; the low dark count rate is important for the long-haul QKD system [69]; and the ultra-low timing jitter makes them a suitable choice for the high speed optical communication systems [70].

SNSPDs are not only ultra-high sensitive devices, but also possess a relatively large dynamic range [51]. This makes them to be a suitable choice for applications that both high sensitivity and large dynamic range is required, such as a long-haul QKD system.

The optoelectronic characterization refers to as measurement of the quantum efficiency, detection efficiency, speed, dark count, jitter time and other SPD char-

acteristics. In this chapter, we first elaborate some principles of single photon detection, then present the results on characterization of SNSPDs via the following steps. First, we introduce our experimental setup, some details of the equipment used and our packaging method that provides us a reliable optoelectronic microwave cryogenic operation. Next, we present the basic optoelectronic characterization results including quantum efficiency and dark count measurements. Lastly, we spend a section on how the photoresponse measured as a voltage signal can be different from the cryogenic cable selections.

2.1 SNSPD Photon Detection

The SNSPDs are fabricated with Niobium Nitride (NbN) thin film on sapphire or MgO substrates. The thin film is patterned into meander nanowires to form the detection area. The size of the area is usually a few tens of square micrometers [28, 31, 51]. The photon detection mechanism of SNSPDs has been developed as a particle based model, in which the incident photons are treated as independent particles. When a photon has been absorbed, the localized heating results in a small hotspot. The localized superconductivity is suppressed or even destroyed, because the photon energy $\hbar\omega > 2\Delta$ introduces a local disequilibrium perturbation with a large number of excited quasiparticles, leading to an increase of the average electron temperature close to or above T_C. The bias superconducting current is thus expelled from the hotspot volume to the "sidewalks" between the hotspot and the edges of the film. If the bias current exceeds the critical current in the sidewalks, a local resistive barrier is formed across the entire width of the nano-wire, resulting in a voltage signal. The conclusion of this view is the so-called "hotspot" model [29, 51] to interpret the single photon detection process by the SNSPD.

Figure 2.1 illustrates the hotspot model of the single photon detection mechanism. The hotspot model matches well with the experimental observations for high energy particles such as α or γ particles. When the wavelength of a photon be-

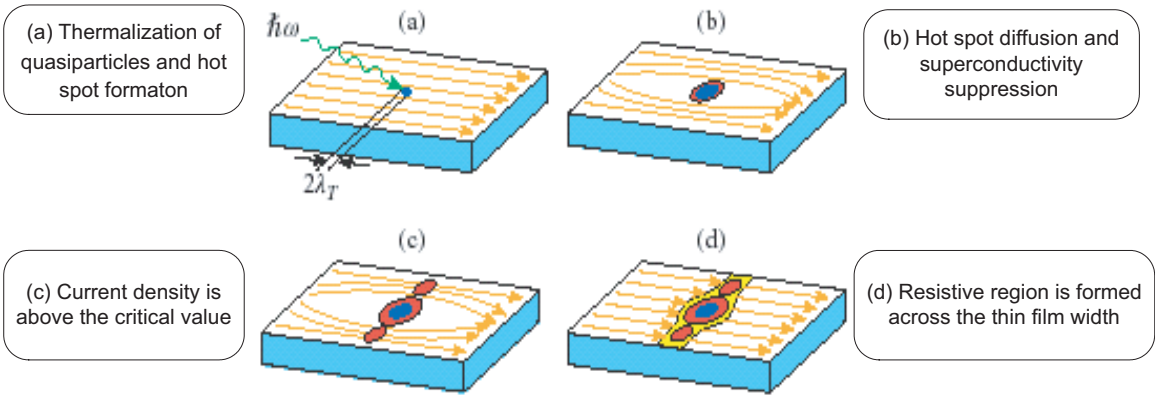

Figure 2.1: The hotspot formation illustration of the SNSPD single photon detection mechanism.

comes longer, this model starts to disagree with quantum efficiency measurements [71], because the diameter of the hotspot generated by the incident photon flux becomes smaller than the required size. The SNSPD photoresponse is thus expected to abruptly disappear at a given bias current density ratio (β_b) at a certain wavelength. However, this prediction is failed to have experimental support, although Semenov *et al.* [72] propose a refined hotspot model by assuming the energy gap and coherence length (ξ) of NbN are exceptionally reduced. The hot-spot detection model only results in a deterministic photon registration event; and it does not account for the quantum nature of the single photons.

For the origin of dark counts, the theory of a phase slip center (PSC), induced either by thermal or by quantum fluctuations, seems to be a promising approach. It has been argued that one dimensional quantum phase slip is not an observable, given the width of SNSPD nano-structured wires [73]-[74]. The thermal PSC can occur only at a temperature very close to its critical point. Therefore, quantum PSC seems to be more likely a mechanism of the dark count.

The above complexities prevent us from developing a conclusive model for the SNSPD photon detection and dark count on the basis of the first principle. Yet, one can still perform experimental operations to characterize the device. The results

obtained from the characterization may shed light for the further understanding the physics of this device.

2.2 Experimental Setup

In this section, we first introduce the equipment used in the experimental setup to perform the characterization measurements; then we illustrate the details of our packaging method including optical and electrical connections; finally we briefly describe the cool down process.

Our characterization setup is illustrated in figure 2.2-(a). The cryostat with customized optical and electrical connections is shown in Fig. 2.2-(b). The raw SNSPD device is mounted in a microwave cryogenic package. The package is mounted on the cold plate of a ST-500 cryostat from Janis Research Corporation. The coherent photon source is id300 DFB pulse laser whose wavelength can be chosen to be either 1310 nm or 1550 nm; its maximum repetition rate is 500 MHz and its optical pulse width is 300 pico-second. The laser trigger is TTL, and controlled by a Tektronix AFG3252 function generator, which can generate trigger signals up to 240 MHz. The laser pulses are attenuated through a digital variable attenuator FVA-3100 from EXFO. The bias-Tee frequency ranges from 10 MHz to 6 GHz. We use Keithley 2400 SourceMeter® as the bias source because the SourceMeter provides fast and accurate I-V measurement and also flexibility in choosing between voltage and current source biasing, but to have a low noise operation careful grounding and EMC considerations should be taken into account. The photon counter is SR400 two channel gated photon counter from Stanford Research Systems. The oscilloscope is DSA71604 Tektronix digital serial analyzer. It has four independent channels equipped with 100 Msamples record length, 16 GHz analogue bandwidth and 50 GS/s sampling rate. The temperature is monitored by Lakeshore 332 cryogenic temperature monitor/controller. The optical pulses are guided by single mode fiber customized by Fiber Connectors Inc to make sure the performance under high

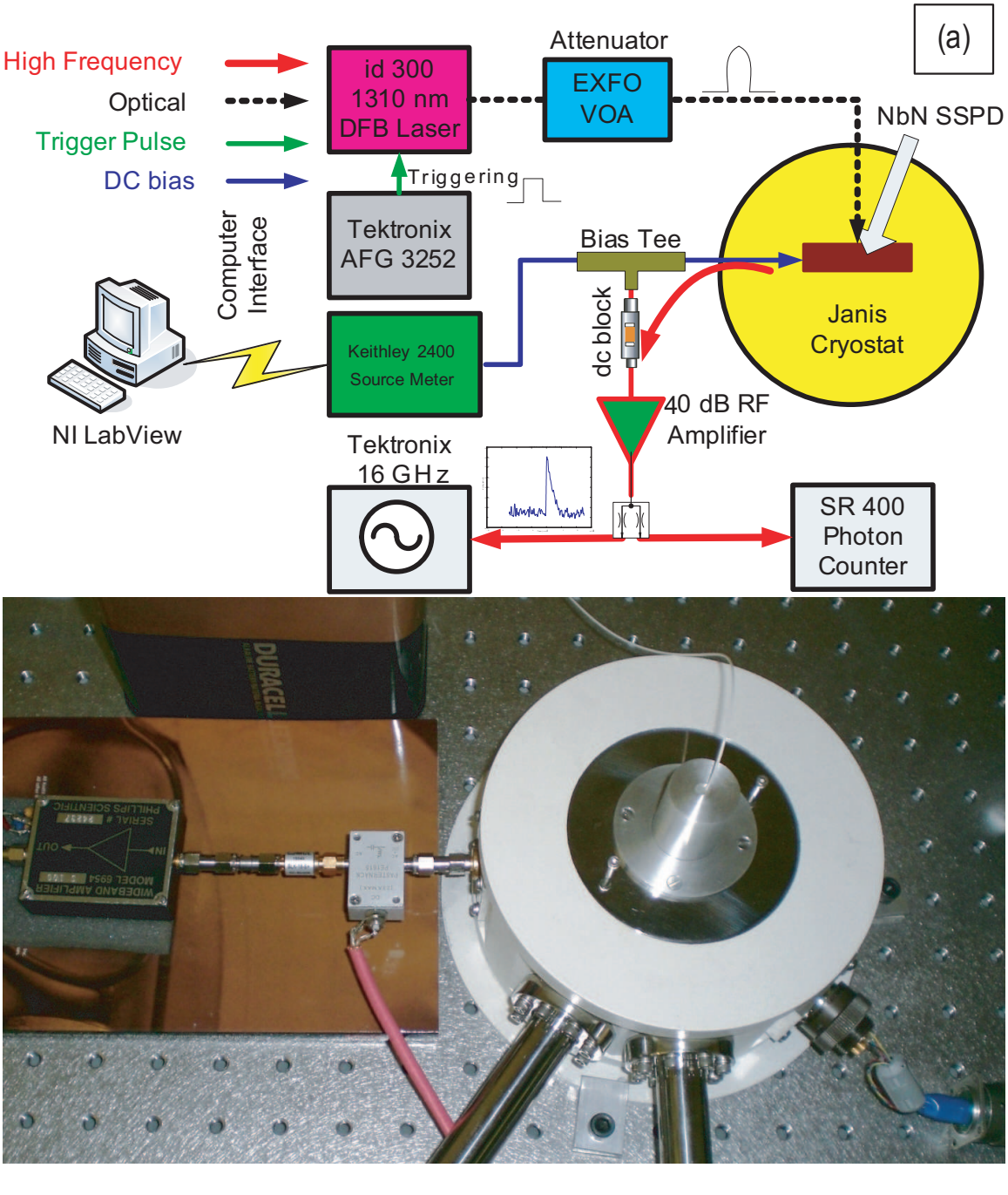

Figure 2.2: The experimental setup (a) block diagram; (b) picture of the cryostat.

vacuum and cryogenic environment.

The SNSPD device is fabricated by Superconducting Nanotechnology, Moscow, Russia. The NbN thin film is 4 nm thick; and the meander line width is patterned to be 120 nm. The $10 \times 10 \mu m^2$ active area has a filling factor of 60 %. Fig. 2.3-(a) shows a SEM image of the SNSPD. The active area is located in the middle of the two triangles. The substrate is R-plane sapphire. The gold film with 200 nm thickness has been patterned to form a coplanar waveguide. The base of the package and its cover (with an optical input) are made of ETP copper (see Fig. 2.3-(b)). The package is first plated with nickel and then gold to make the thermal resistance between the package and the cold plate as low as possible. The SNSPD is fitted in a pocket in the middle of the base (see Fig. 2.3-(c)). The interface between the pocket and the SNSPD has a thin layer of cryogenic thermal grease applied to it to affix the device and to minimize the thermal resistance across the interface.

Considering the dielectric constant of the Teflon in a SMA connector may change due to the cryogenic temperatures, we use a K-connector. The microwave center pin is connected to the pads of the SNSPD by a gold wire/ribbon which is glued at both ends by silver epoxy. The thermal cure time is 60 minutes in nitrogen environment at 90 °C. The ground pad is directly connected to the wall of the package by the gold wire. Our optical alignment method is similar to what has been reported by Stevens *et al.* [66]. An infrared LED is initially used to find the right position of the center of the active area. We drill a hole at the center of the base of the package, right below the active area between the two triangles. A microscope objective lens together with a CCD camera captures a magnified image of the active area of the SNSPD through the hole. The illumination from this LED helps CCD camera capture the infrared image (see Fig. 2.3-(d)).

Then we install our fiber connector base on the cover of the package. The connector base is made by customizing a standard FC/PC single mode fiber connector/adapter. The fiber is connected by a standard single mode Fiber FC/PC

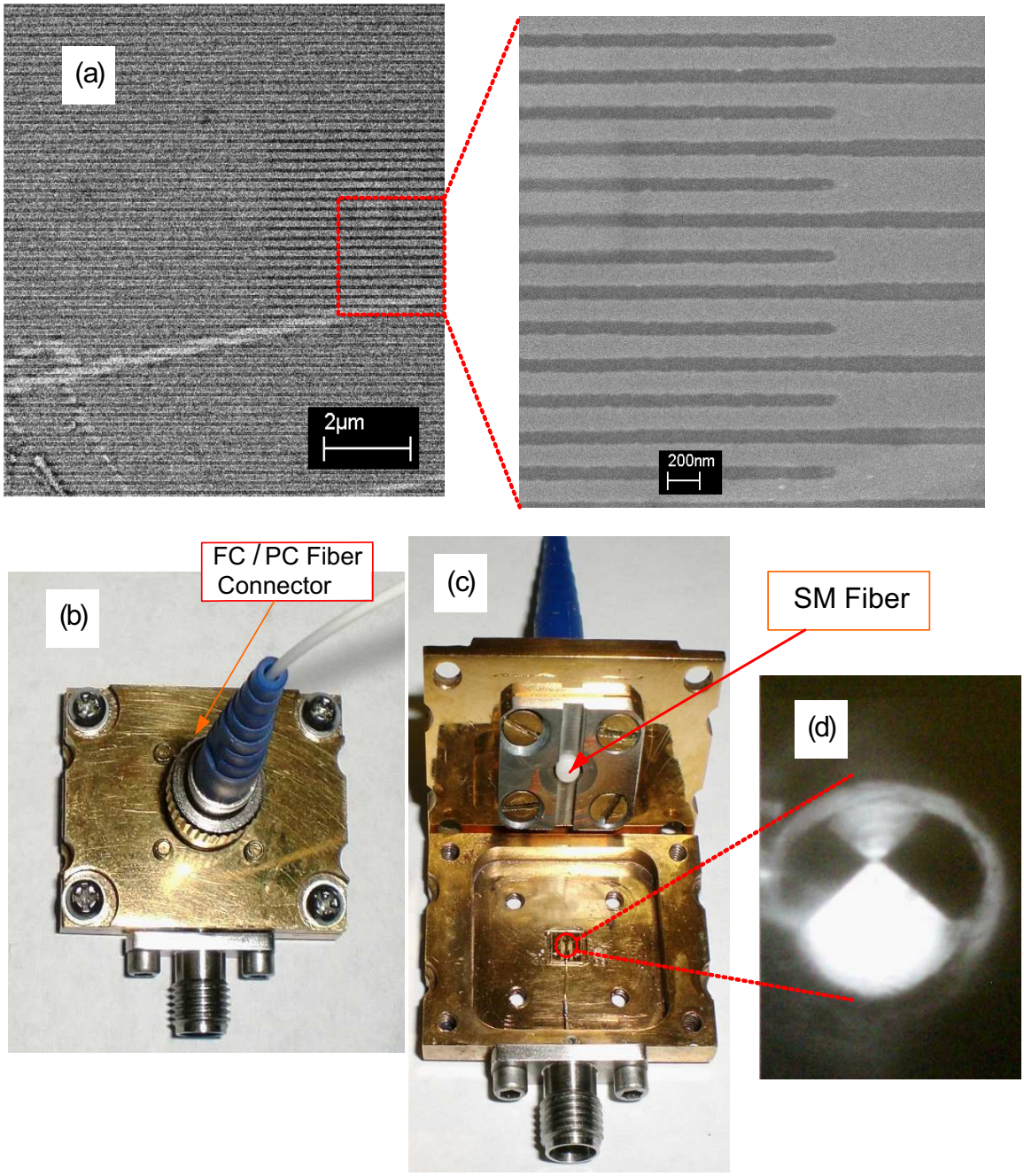

Figure 2.3: illustration of the SNSPD and its package: (a) SEM image of the $10 \times 10 \mu m^2$ active area; (b) The package with cover installed; (c) The package when the cover is open; (d) The microscope infrar image of the SNSPD active area for the optical alignment.

connector. The end of the fiber would be in the center of a 2500 μm ferrule. Now the finished cover is mounted on the base of the package. The distance between the end of the ferrule to the surface of the active area is made to be 300 μm. This distance is chosen due to the consideration of the thermal contraction as well as the optical spot size to maximize the optical coupling. Then shining the fiber with a 10 dBm 1310 nm laser and by using our hole and imaging system to observe the location of bright spot on the SNSPD, we try to do the adjustments. The optical alignment is done when the bright spot overlaps with the active area center marker.

After finishing the optical alignment, the package will be mounted in the cryostat. During the cooling down process, both the Keithley SourceMeter and Lakeshore temperature controller are controlled by the LabView® software through RS-232 and IEEE-4888 interfaces. The packaged SNSPD is loaded in the ST-500 cryostat. We pump down the pressure of the cryostat down to 1.6^{-6} mbar. The initial pumping down needs about 24 hours to make sure the trapped air molecules are evacuated as much as possible.

To load a packaged SNSPD in the high vacuum chamber of ST-500 has remarkable advantages, because the ultra high vacuum frees oxygen, which causes the aging effect to the NbN thin film. The aging effect is most probably induced by the slow oxidization of nanowire, if it is exposed to the oxygen molecules under a long period of time. As a result, the critical current of a given device at 4.2 k will gradually decrease. Ultimately, the device will have fluctuating detection efficiency, or even malfunction.

After the vacuum of ST-500 reaches the desired level, a continuous liquid helium flow is supplied into a hollow copper coil around the ST-500 cold plate. Fig. 2.4 depicts the measurement of the resistance during the cooling process as a function of time. The cold plate temperature is monitored by the Lakeshore 332 temperature monitor/controller; and plotted in the same figure. In all of the measurements in this chapter, the base temperature is always kept at 4.2 K ($\sim$1 atm pressure) by adjusting the helium flow knob on the transfer line. The transfer line requires

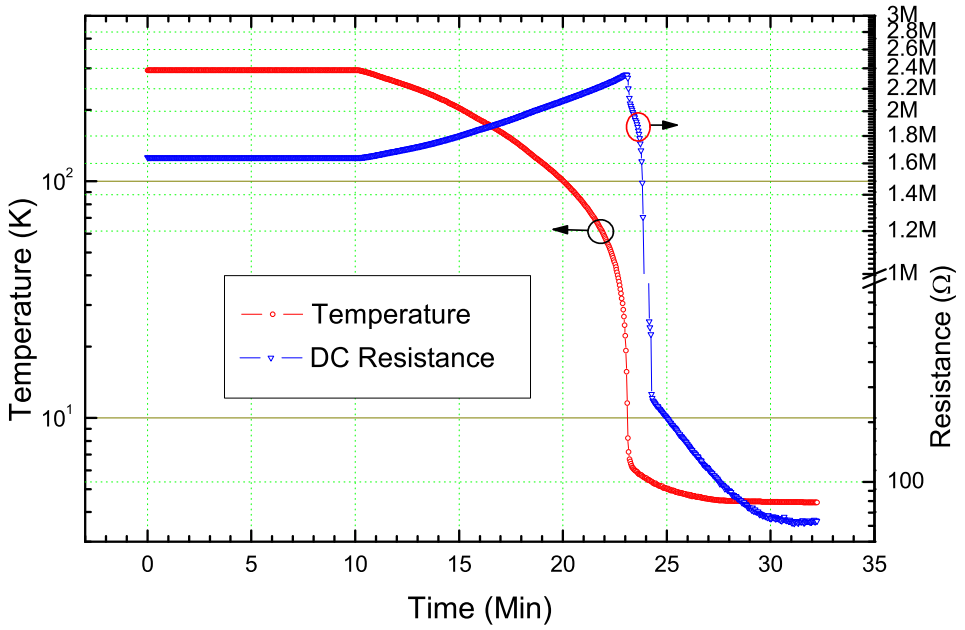

Figure 2.4: ST-500 cooling and measured resistance of a SNSPD from its normal state down to superconducting sate.

vacuum level of 4×10^{-4} mbar. It must be pumped down prior to the helium transfer. The initial cooling to the cold plate needs about some twenty minutes, but a time lag is required to reach the sample temperature stabilization. The reliable measurement usually can be guaranteed after half an hour.

Fig. 2.5 shows the measured resistance curve during typical liquid Helium cooling down process. The initial normal state resistance at the room temperature monotonically increases to the maximum value at about 18 K. The maximum value of the resistance varies from device to device [1]. The superconductor critical temperature T_c is measured approximately at about 9 K, because of the fast cooling speed when the cold plate drops below 30 K (close to 1/10 of the Debye temperature for the Copper, leading to the exponential reduction of its thermal capacity). The transition width is larger than 1 K. More accurate measurement of critical tem-

[1]The Residual Resistivity Ratio (RRR) is the ratio of the dc resistance measured at 300 K over that at 20 K. It is usually smaller than one for amorphous and polycrystalline thin films, such as a few nm thick NbN thin films, because the transportation of electrical charge carriers is limited by the hopping process between local crystalline cites assisted by the thermal activations.

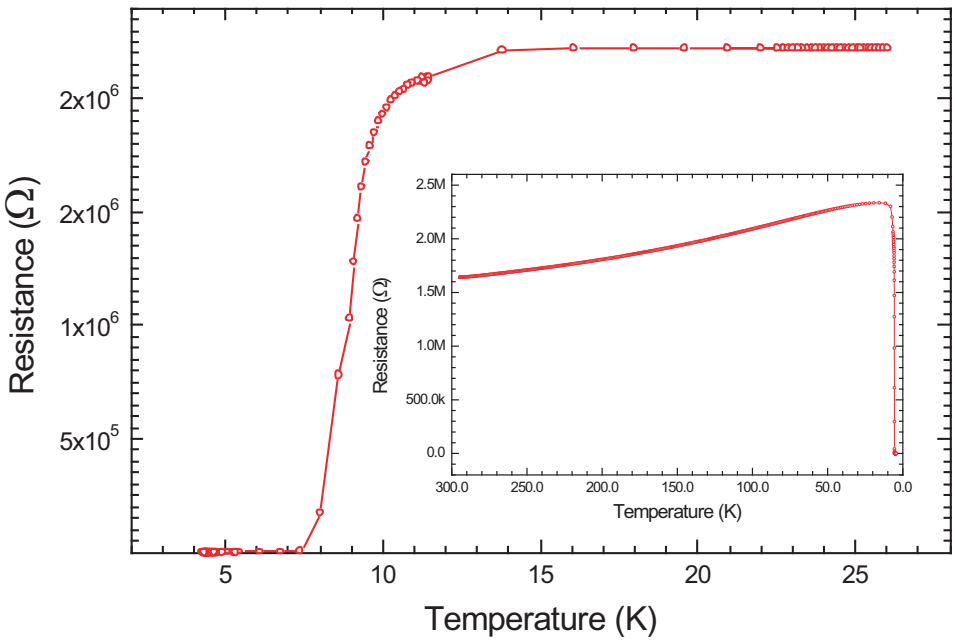

Figure 2.5: Measured resistance vs. temperature, the inset shows the transition from the room temperature normal state to the cryogenic temperature superconducting state.

perature can be achieved by using the temperature controller to heat up the cold plate temperature while keeping the base temperature below T_c. We will discuss and report the results in the following chapter.

2.3 Experimental Results

Based on the preceding experimental setup, we have carried out the optoelectronic characterization of the SNSPD. The first step is to determine the critical current I_c when the device is in a stabilized temperature of about 4.2K. We measured I_c by slightly increasing the Keithley SourceMeter current output to the maximum (before the device latching occurs). The critical current has been found to be 29.53 μA. Likewise, the return current (I_{ret}) that manifests the formation of hot-spot plateau can be obtained by switching the SourceMeter output to the voltage mode and measuring the bias current above the voltage value where the I_c is located.

The detailed discussion on its physical origin has been reported by Skocpol *et al.* [75]. We have determined the value of I_{ret} to be 5.66 μA on average at 4.2 K based on its definition by Johnson et al. [76].

The photon counting period is 60 seconds for all of the dark count and photon response measurements. The pulsed laser source repetition rate is 1 MHz. The laser pulse is attenuated by the variable attenuator ranging from -63 dB to -1 dB. The corresponding average number of photons per pulse at the output of the attenuator varies from 1 to 10^6 photons per pulse.

The optical coupling efficiency includes two basic sources of loss: the loss of fiber connectors and optical fiber; and the loss due to the 300 μm free space between fiber-end and the active area of SNSPD. Considering the total length of the single mode fiber is just about three meters in our setup, the former contribution is less than 1 dB and the contribution due to the later one becomes dominant.

We have experimentally confirmed that the loss of optical fiber is negligible by measuring a known optical power level transmitted through the whole system. Even in perfect optical alignment, the short free space distance between the fiber-end and the active area inserts more than 19 dB optical coupling loss. This loss has been calculated by knowledge of the device active area and the optical spot size on the surface of the device.

In order to calculate the Device Quantum Efficiency (DQE)[2], we first obtain the net photon count by subtracting the total photon count with the dark count; then the total incident photon number that enters the optical fiber has been normalized to the device active area by considering the optical coupling coefficient. The ratio

[2]In the literature of SNSPD, Quantum Efficiency (QE) is more often used as a measure of how sensitive a SNSPD can be. QE can be understood as the maximum DQE achievable under a given set of conditions for the given device, usually read at the highest dc bias ratio. Sometimes when the optical coupling is of the interest, a system level QE is used, namely SQE. SQE is similar to the DQE, but only the total photon number entering the packaged SNSPD, without the normalization, is taken as the denominator. The ideal value of SQE should be identical to that of DQE. In practice, SQE is strongly limited by the packaging technique.

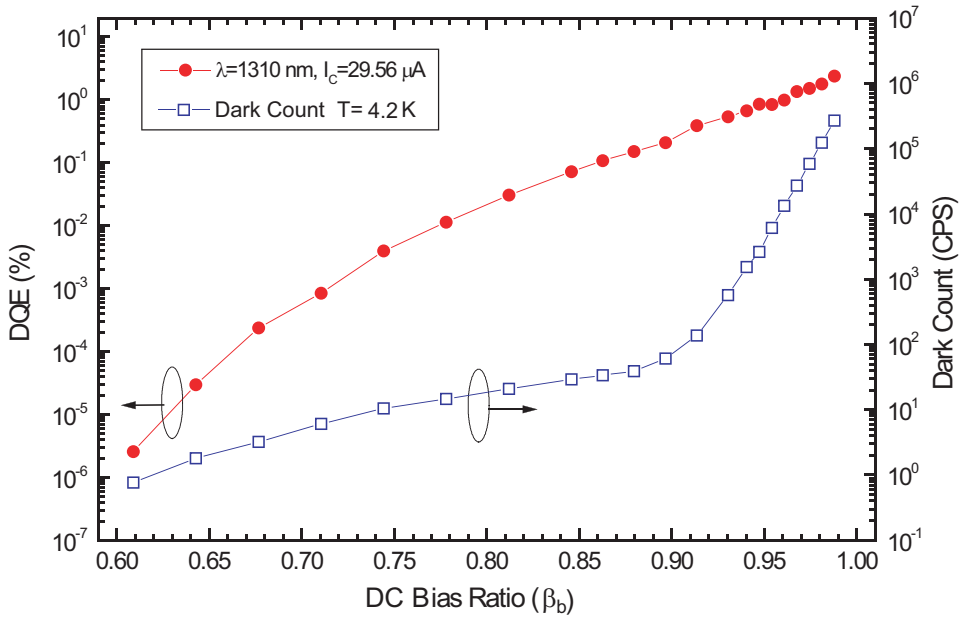

Figure 2.6: The measured device quantum efficiency (DQE) and dark count rate vs. dc bias current ratio β_b.

of the net photon count n_{net} over the normalized total photon number n_{tot} on the device active area is expressed as a percentage number, namely Detection Efficiency (DE).

The DQE is the value of DE when the average $n_{tot} = 1$. Both DE and DQE have to be measured under a certain set of condition, including the DUT temperature T, incident photon wavelength λ, and dc bias ratio β_b. To ensure the single photon operation regime, the average photon number was set to be much lower than one per pulse per device active area. Under the same experimental conditions, we have measured the dark count just by turning on the shutter of the variable attenuator. The measurement result is shown in the Fig. 2.6 with a right side y-axis. Two distinct slopes have been identified. When the bias current ratio is between 60 % to 90 %, the dark count rate ranges from 1 to 100 Counts Per Second (CPS); whereas when the bias ratio is above 90 %, the dark count increases dramatically until it reaches to 2×10^5 CPS at the bias ratio of 98.8 %. Recently, Leoni *et*

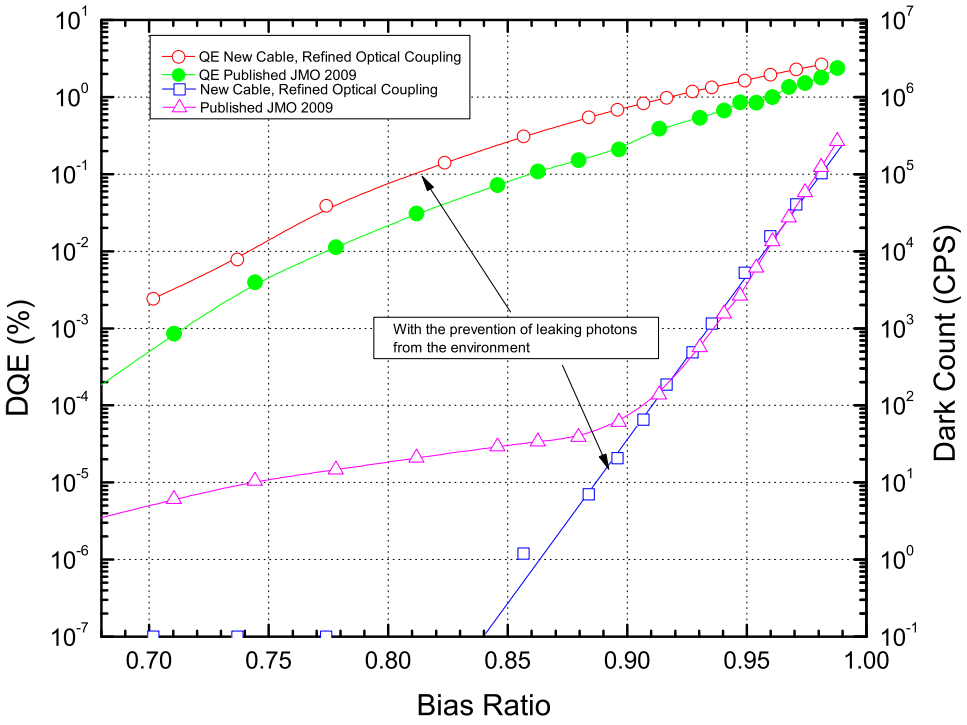

Figure 2.7: The newly measured DQE and dark count vs. bias ratio resulted from the improved measurement setup by blocking the optical leaking via the fibers.

al. [77] have reported their dark count characterization result that is in the same magnitude when the bias current is close to I_c. Their dark count also shows a floor when $\frac{I_b}{I_c} <= 0.75$.

In order to find the origin of the double slope of our dark count curve, it is important to re-examine the setup we have used. Since the above measurement was performed in a regular lab without completely shut down the light sources, such as the light bulbs; the instruments employed in the experiment also contribute some unwanted photons that may couple to the detector through the bendings of the optical single mode fiber. To confirm this, we use a thick black plastic sheet to cover the entire fiber path from the id-300 DFB laser output to the customized top cover fiber insertion port. Fig. 2.7 shows the comparison with the previous experimental results where fiber was not protected from introducing environmental photons undesirably coupled to the single detection system. From the plot, we can see that the dark count drops below one count per second at the bias ratio of 85%.

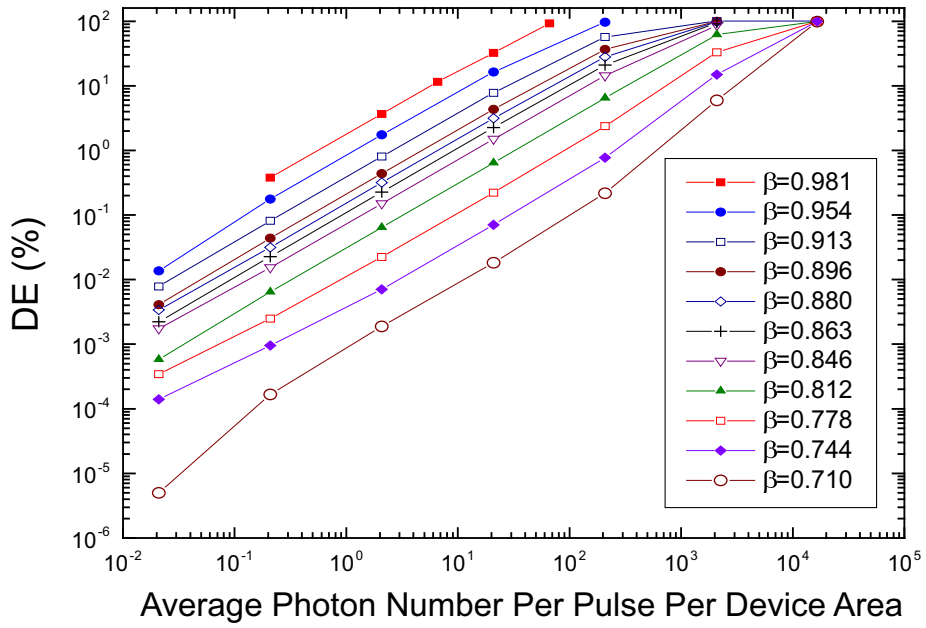

Figure 2.8: The detection efficiency vs. the number of photons per pulse per device active area under different bias ratios.

At 90% ratio, dark count is just about 10 CPS, whereas QE is still at 1% without decreasing significantly. So this regime can be a good operating point for a practical QKD system. More impressively, the QE is also enhanced at the lower bias ratio because the dark count at those bias ratios has been significantly suppressed, as a result the net photon count increases.

Fig. 2.8 shows the detection efficiency (DE) at different levels of photon number per pulse per device active area. The largest linear dynamic range occurs when the bias ratio is about 80%. When the bias current ratio is very close to the critical current, e.g. 99 % of bias ratio, at a repetition rate of 1 MHz, the number of dark counts becomes comparable to the number of photon counts, so the highest bias ratio shown in the figure is 98 %. In addition, the detection efficiency reaches 100% at high intensities where the average number of photons per pulse is much higher than one. Moreover, we observed at a relatively low bias ratio, e.g. 70 %, the device detection efficiency decreases dramatically.

2.4 SNSPD Photoresponse Measurement and Simulation

The photon detection event is registered when a voltage peak is measured to be higher than a preset threshold value. The voltage signals can be used to trigger a photon counter, such as SR-400. They also ignite the start/stop signal to determine the timing jitter[3] histogram. Therefore, the photoresponse time is very important. In this section, we start with an equivalent circuit model to simulate the intrinsic response, then compare it with the measurements, based on two types of cryogenic coaxial cables. Each transmission bandwidth of them is different, resulting in different the rise and fall times, even with the same device and same bias conditions.

2.4.1 Equivalent Circuit Model

The equivalent circuit model is constructed on the basis of photon detection process revealed in ref. [78]. When a photon is absorbed at a certain local spot of the nanowire, one hotspot is developed (regardless of how many numbers of photons are absorbed). The abrupt change of L_k under dc bias current consequently results in a ultrafast voltage impulse. The detailed discussions on how the impulse voltage is generated are reported in the Appendix A. The photon induced voltage source is illustrated in the figure of the circuit model as $V_s(t)$. To evaluation of its amplitude by the time variation of L_k, readers can refer to Appendix B. The ideal photoresponse $V_o(t)$ can be simulated by solving the differential equation

$$L_k C \frac{d^2}{dt^2} V_o^{ph}(t) + \left(R_s C + \frac{L_k}{Z_0} \right) \frac{d}{dt} V_o^{ph}(t) + \left(\frac{R_s}{Z_0} + 1 \right) V_o^{ph}(t) = V_s(t) \qquad (2.1)$$

The proposed equivalent circuitry is shown in Fig. 2.9. The values of the model components are determined by the two-step S-parameter measurements. The de-

[3]To characterize SNSPD jitter time, one has to use the photon source whose pulse width must be shorter than the jitter time of SNSPD. In current setup, the pulse width of id-301 is 300 ps. So it is unlikely to be suitable to find sub-100 ps jitter time of SNSPDs.

Table 2.1: Model Parameters Used in SNSPD Photoresponse Voltage Simulations

Description	Value
Serial resistance R_s	20Ω
Transient voltage V_s	1.53 volt
Stray capacitance C	1.2 $\times 10^{-12}$F
Kinetic inductance L_k	200 $\times 10^{-9}$ H
Impedance of Transmission Line Z_0	50Ω

tailed procedures and principles will be elaborated in the following chapter. Fig. 2.10 demonstrates an ideal photoresponse without considering any interconnection frequency dispersion. The circuit model parameters are tabulated in Table 2.1. The measured voltage response is in fact a system level response. In other words, it also depends on the equivalent circuit response to the impulse excitation, the transfer function of cryogenic microwave cables, and other interconnections. For example, Fig. 2.12 shows a typical photoresponse, captured in the SNSPD optoelectronic characterization measurements. The simulated intrinsic rise time is about 130 ps based on the equivalent circuitry depicted in Fig. 3.1. The measured photoresponse exhibits a slight bipolar voltage partly due to the bias-T, which is acting as a high pass filter to suppress the dc and low frequency components. However, the measured rise times at the system level are different caused by the choice of cryogenic cable, provided that the rest of interconnecting components are identical. In the following subsection, we will investigate one of the major factors that decides the rise time as well as its relative amplitude.

2.4.2 Photoresponse Rise and Fall Time

We have examined the rise time of the photon/dark count voltage responses from our packaged SNSPD under proper bias conditions. The rise time and fall time of the measured photoresponse are a system level quantity. Fig. 2.12 and Fig. 2.13

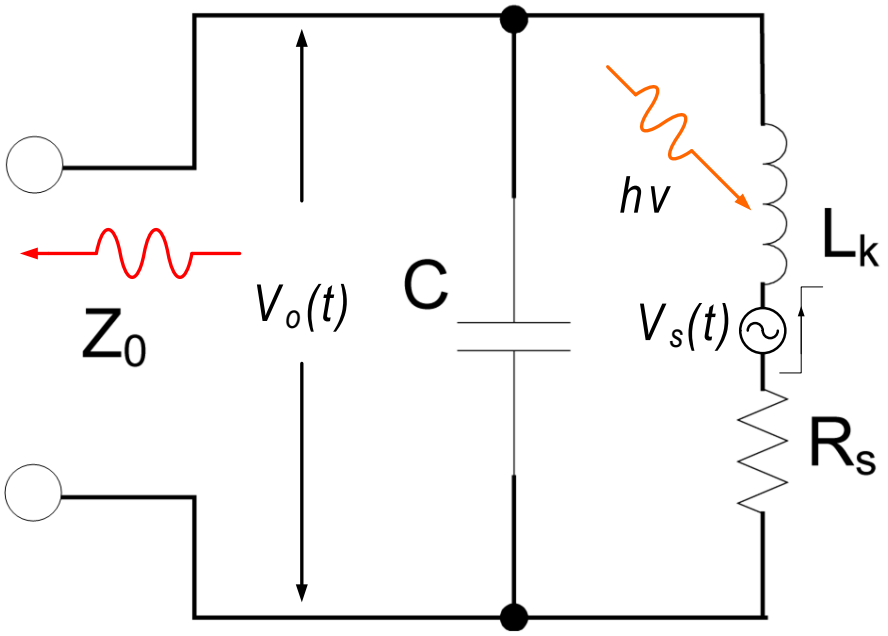

Figure 2.9: The equivalent circuit to account for SNSPD photoresponses when a photon denoted as hν is absorbed by the nanowire denoted as L_k; voltage response $V_o(t)$ is propagating along the transmission, whose impedance is denoted as Z_o. When the bias current $I_b < I_r$, no hotspot can be formed. therefore, no photoresponse is anticipated to be measured.

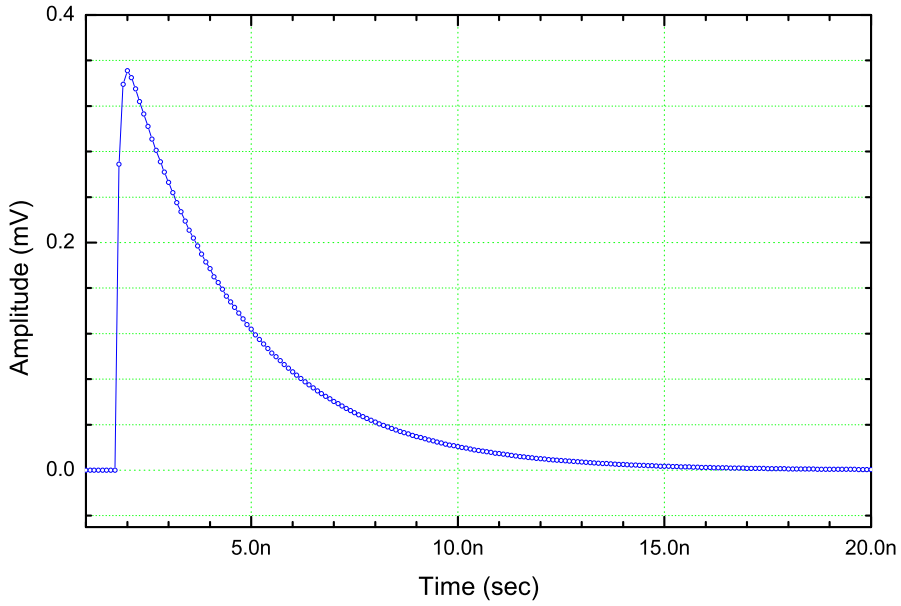

Figure 2.10: The simulated photoresponses based on the equivalent circuitry in the absence of interconnection dispersions.

demonstrate two screen shots obtained for two types of cryogenic cables. The mean rise time of the waveforms ranges from 600 to 800 ps for the former plot; while 240 to 310 ps for the latter. Both screenshots are obtained by the Tektronix DSA71604 via its build-in algorithm.

Two screenshot measurements only manifest the system level photoresponse. It relies on the entire chain transfer characteristics. The cryogenic cable, the amplifier, the bias-T, and the bandwidth of the oscilloscope are critical path nodes that contribute to systematic rise and fall time, particularly the rise time.

While keeping the same RF/microwave amplifier in all of our measurements, we compared two sets of measurements based on two types of cryogenic cable. Their transfer function in the frequency domain (up to 10 GHz) can be represented by S_{21}. Fig. 2.11 illustrates S-parameter measurements of both types of cables as a two port network. The flexible one indicates the core of the cable is made of stainless steel, so is the shield; the semirigid indicates that the core and shield are made of carbon steel with silver coating, resulting in better performance.

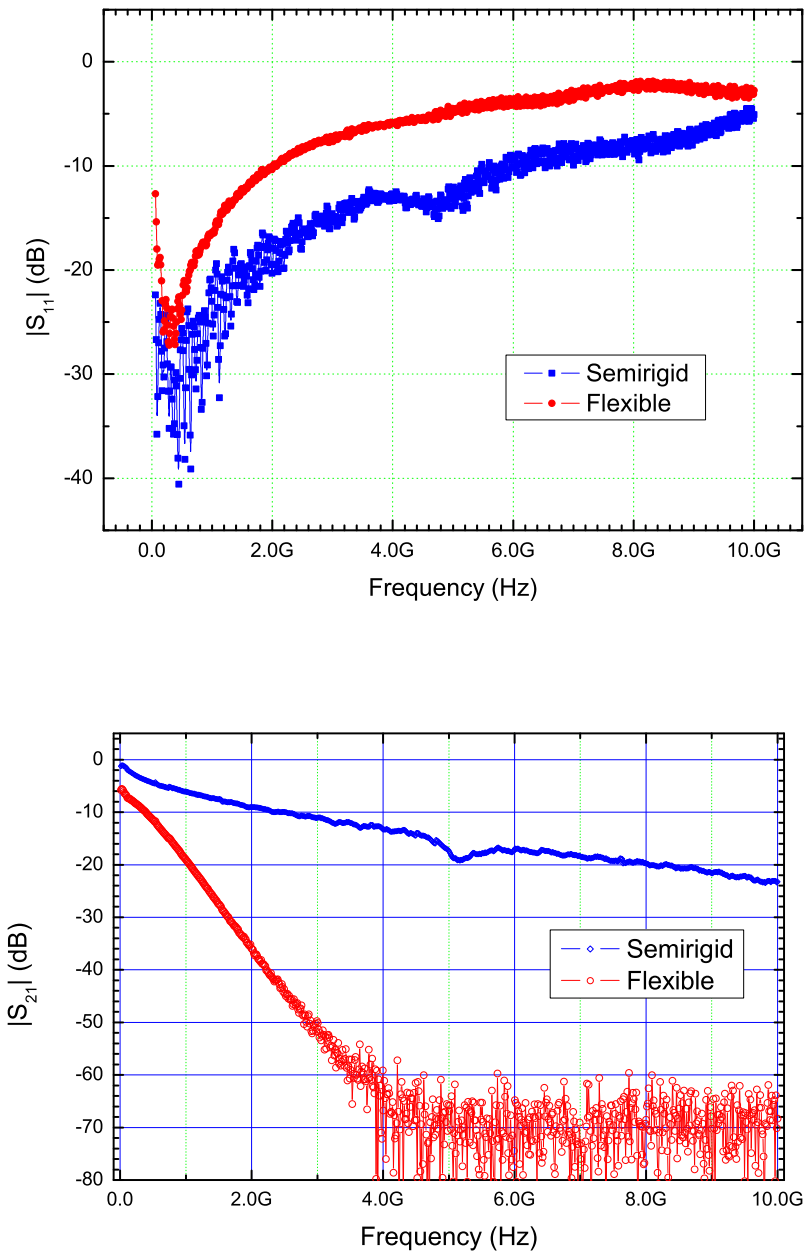

Figure 2.11: The cryogenic cable amplitude reflection and transmission functions measured by S-parameter S_{11} and S_{21} for two types made of different materials.

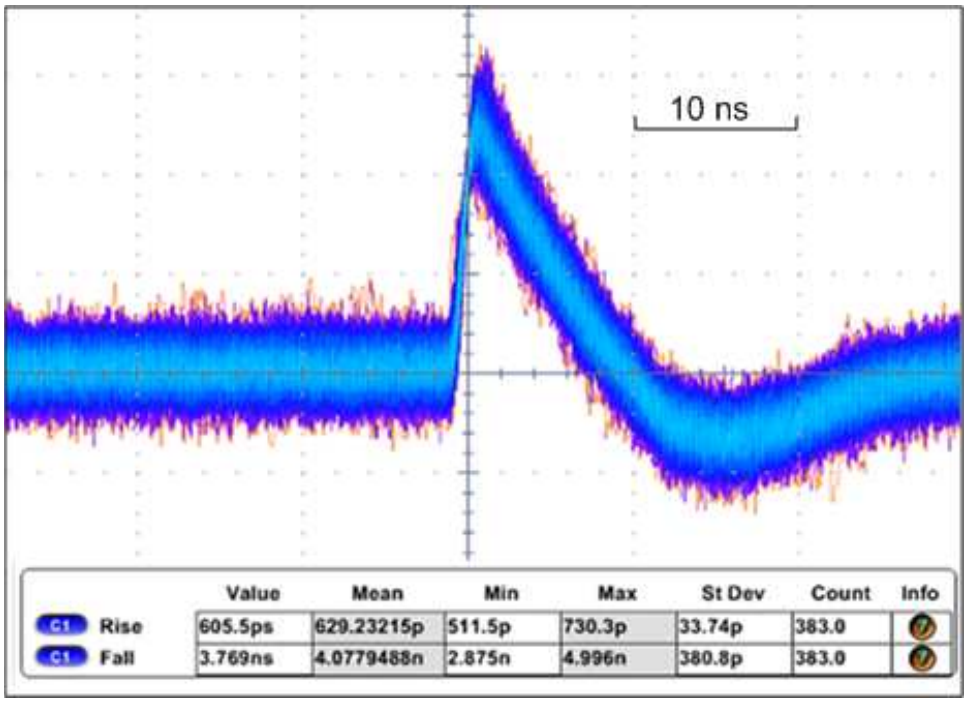

Figure 2.12: Screen shot of a typical photon/dark count voltage response for the flexible cryogenic cable.

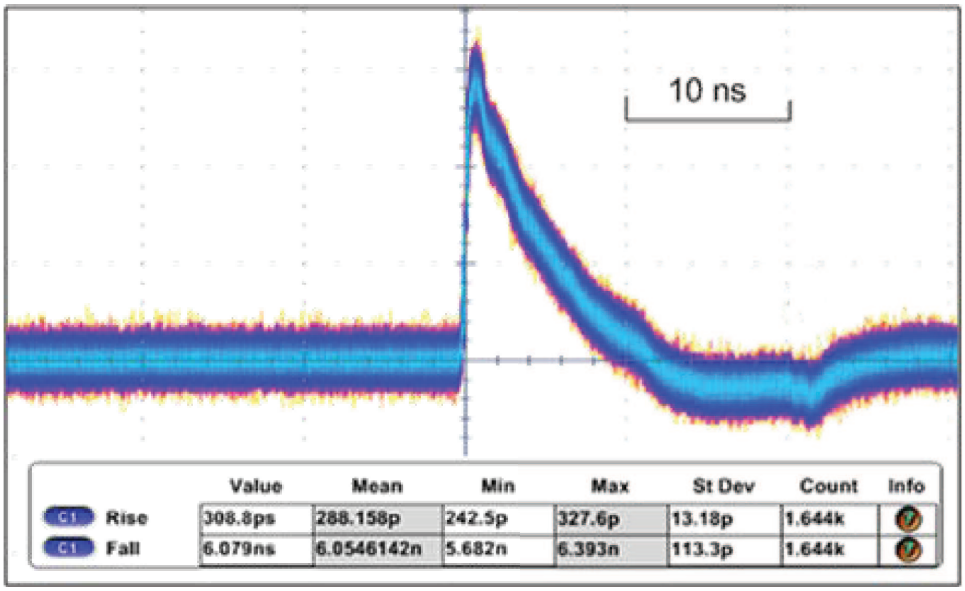

Figure 2.13: Screen shot of a typical photon/dark count voltage response for the semirigid cryogenic cable.

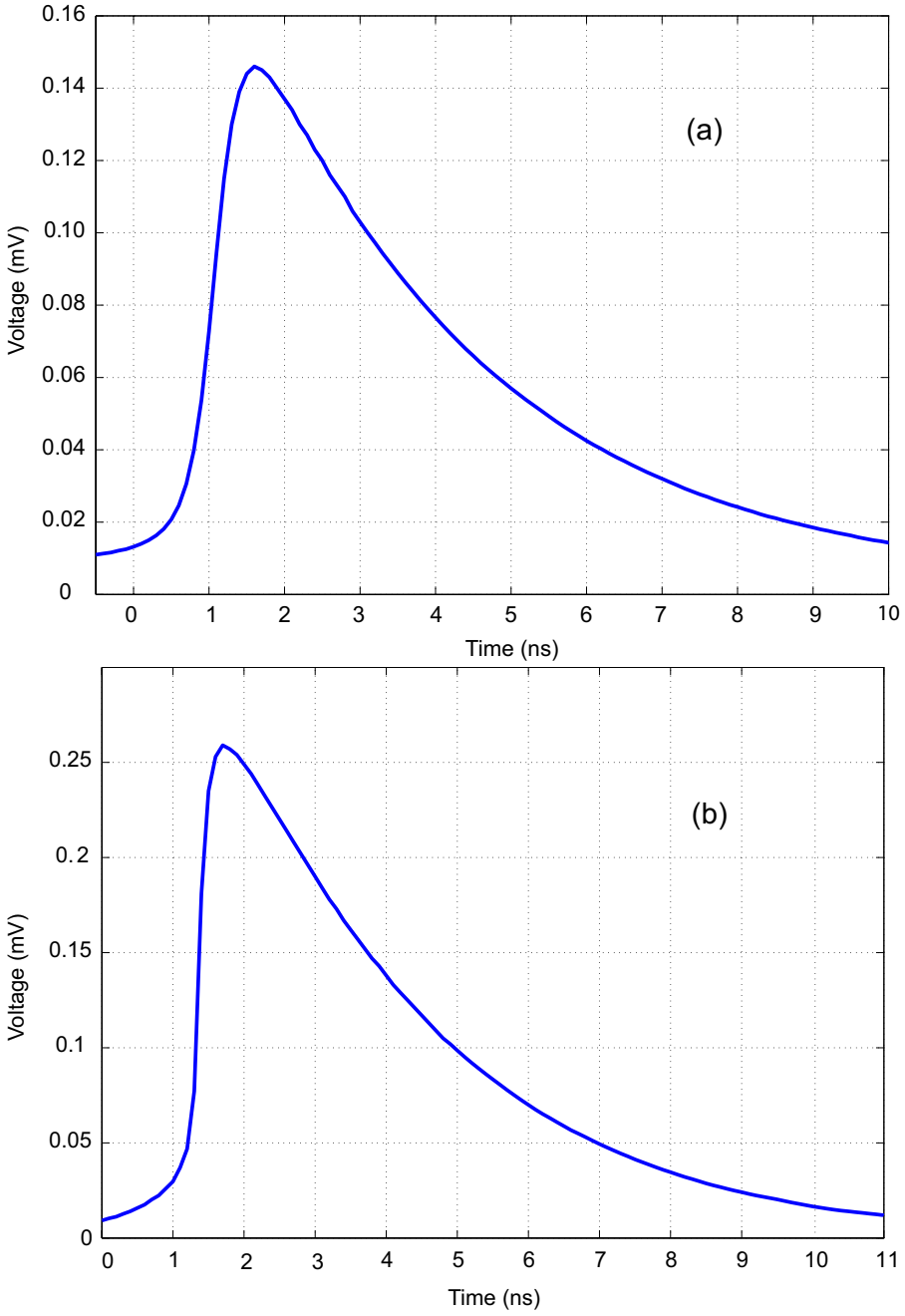

Figure 2.14: The photoresponse simulation by taking into account of the different cryogenic cable transmission function as a frequency synthesizer filter.

We use Fourier transformation to convert the simulation results obtained by numerically solving Eq. 2.1 from time domain into frequency domain

$$\tilde{V}_o(\omega) = \mathcal{F}\{V_o(t)\}$$

Here we have not treated $V_o(t)$ as repetitive signal, considering the dark count/photoresponse voltage randomly generated in the time domain. In the above transformation, only a single shot with discrete time space of 50 picosecond is used to perform the FFT in the matlab. Then we multiply it with S_{21} at each frequency point. The interpolation was employed to match the date points. At last, we perform a reverse Fourier transformation to obtain the new voltage response in the time domain $V_o'(t)$

$$V_o'(t) = \mathcal{F}^{-1}\left\{\tilde{V}_o(\omega) S_{21}(\omega)\right\}$$

In the above calculation, we have not taken into account the reflections for both cables, observing their S_{11} are relatively well matched, in particular at lower frequencies. Since the main power spectrum of the photoresponse single shot occupies the frequency band below one GHz.

Fig. 2.14 illustrate the simulation results by incorporating the transfer characteristics of two cables. The simulation algorithm treats each cable as a frequency synthesizer filter. The simulation demonstrates the amplitude reduction for the same intrinsic photoresponse (see Fig. 2.10). The simulated system level photoresponse with the flexible cable S_{21} has the rise time around 600 ps; and the rise time using the semirigid cable S_{21} reads around 300 ps. Both time estimation is using 10% and 90% amplitude rise time threshold. The simulation results agree well with the experimental results in both the rise time; as well as the relative amplitude. We believe that our measured rise time is mainly limited by the cryogenic cable bandwidth, but to further improve it, implementing higher bandwidth amplifiers are definitely required.

2.5 Summary

In this chapter, we have described our characterization setup for SNSPDs. The in-house packaging of the SNSPD has achieved a good optical coupling without any further on chip micro-mechanical processing. The electrical connection was proved to satisfy the requirements imposed by the wide band cryogenic operation. The cooling process by ST-500 has been delimited in detail. The high vacuum chamber of ST-500 has tremendous advantage for the long term stability for a given SNSPD, that ensures repeatability and reliability of the characterizing system.

The characterization measurements showed operation in single photon detection regime with 40 dB dynamic range at 80% bias ratio. The device quantum efficiency and dark count measurements have been done through basic optoelectronic characterization techniques and the experimental results agree with relevant literature.

We further examines the photoresponse by invoking an equivalent circuit, obtained in our small signal S-parameter measurement, which will be elaborated in the following chapter. We measured two different rise times associated with two types of cryogenic cables. The cables were treated as band synthesizer filter and their S_{21} was measured and employed as a transfer function in the frequency domain. We simulated the entire system level photoresponse, by considering the non-ideal bandwidth of a given cryogenic cable. The simulated rise time was compared to the experimental result. The good agreement between them implies that the cryogenic cable is the main critical path node when the rise time is around 300 ps, but to further reduce the rise time, higher bandwidth amplifier is also needed.

Chapter 3

DC, Small Signal RF/Microwave and Optical Characterization

In the preceding chapter, a setup for optoelectronic characterization of a SNSPD has been established, and is proved to be reliable for further investigating photon detection in the superconducting nanowire structure. The photon detection can be viewed as one strong nonlinear effect particularly exhibited in those nanowires. In principle, the strong nonlinearity stems from the strong depletion of Cooper pair density. Either bias current, or incident photon flux, or increased temperature can drive the nanowire into deep Cooper pair depletion regime.

One efficient way to probe the Cooper density is to measure the kinetic inductance of the nanowire structure. The inductance measurement requires an incident RF/microwave power and comparing the reflection power for both amplitude and phase. Since the nanowire makes a very sensitive detector, the incident RF/microwave probing power should be as low as possible. In this chapter, we will present a one-port S-parameter measurement that fulfills the above requirement; and apply the developed method to investigate the nonlinearity under combinations of temperature, bias current and optical power.

Microwave measurements have been exploited to examine the nonlinear properties of superconducting materials for many decades [79]-[80]. The merit of nonlin-

earity can be studied by measuring the parametric variation of the Quality factor (Q-factor), surface reactance and resistance of superconducting resonators. Such variation always behaves as a function of frequencies and power levels of the input signal [81], external magnetic field, or ambient temperature [82]-[83]. The nonlinearity can even be found by measuring higher orders of harmonic power spectra [84]. Abdo *et al.* discovered some potential applications by studying bifurcations induced by a nonlinear NbN resonator [85].

However, studies on dc current or voltage induced nonlinearity have not yet been performed in the above devices, mainly because they can be treated only distributively, due to their relatively larger geometrical sizes with respect to the operation wavelength. Recently, NbN nanowire meanderlines have extensively been used to make the SNSPD [31]. The total length of the meanderline is typically 500 μm, much shorter than the center wavelength of a photon-induced microwave signal. One can treat the SNSPD as a lumped circuit element, terminating at one end of a normal transmission line, typically a 50 Ω Coplanar Waveguide (CPW) made of Au/Ti. Therefore, new technique is required to explore the DC-bias induced nonlinearities, particularly in the kinetic inductance or natural damped resonance frequencies associated with the meanderline.

Since relatively large but nonlinear kinetic inductance is an intrinsic property of the SNSPD, the relationship between the kinetic inductance and bias current might reveal geometrical constrictions that limit the quantum efficiency (QE). R. Hadfield *et al.* showed that the correlation between QE and SNSPD kinetic inductance does exist [65]. A. Kerman *et al.* attributed a limiting factor for QE to the constrictions of nanowires [63]. The value of the kinetic inductance also determines the rise and fall times of the photo-induced signal in the SNSPDs. The fall time is associated with the device recovery time, a key timing for the operational speed of SNSPDs [86]. In addition, the nonlinearity of the kinetic inductance can be potentially useful to devise and integrate novel superconducting single photon detectors with parametric amplification transmission lines [87]. Therefore, kinetic inductance and

its relationship with electrical bias becomes important figure of merit for SNSPDs.

Since the NbN nanowire is essentially a one-port passive device, one can readily explore combinations of resistive and reactive components, when it is treated as the load of a transmission line by the S-parameter measurement. Recently, Miki *et al.* characterized their SNSPDs fabricated on MgO substrate via the one port S-parameter measurement in the RF band [59]. However, only the kinetic inductance has been reported in the current bias mode. In this work, we employ such measurements not only to explore the kinetic inductance, and other relevant reactive and resistive components, under either dc current or voltage bias, but also to find the resonant frequency and quality factor of the packaged NbN meanderline. Furthermore, the detail of a one-port S-parameter measurement including the calibration at low temperature is presented in this chapter.

In the following sections, we first construct the model of equivalent circuitry; derive mathematical relations to compute values of the circuit elements; apply our experimental results to obtain the kinetic inductance, the capacitance and the series resistance; and finally justify the results by the measurement of resonant frequencies and quality factors under various biasing conditions.

3.1 Equivalent Circuit Model for S-Parameter Measurement

3.1.1 The Construction of the Equivalent Circuit Model

We use the packaged SNSPD identical to what we have reported in the previous chapter to undertake all the measurements. However, in the context of current chapter, NbN nanowire meanderlines of the SNSPD are taken as the device under test (DUT). The nanowire meanderline has the same geometrical sizes as what the SNSPD has. For DUT critical temperature T_c, we use an alternative method to find its value. It is estimated to be close to 10.4 K, by the best fitting to the

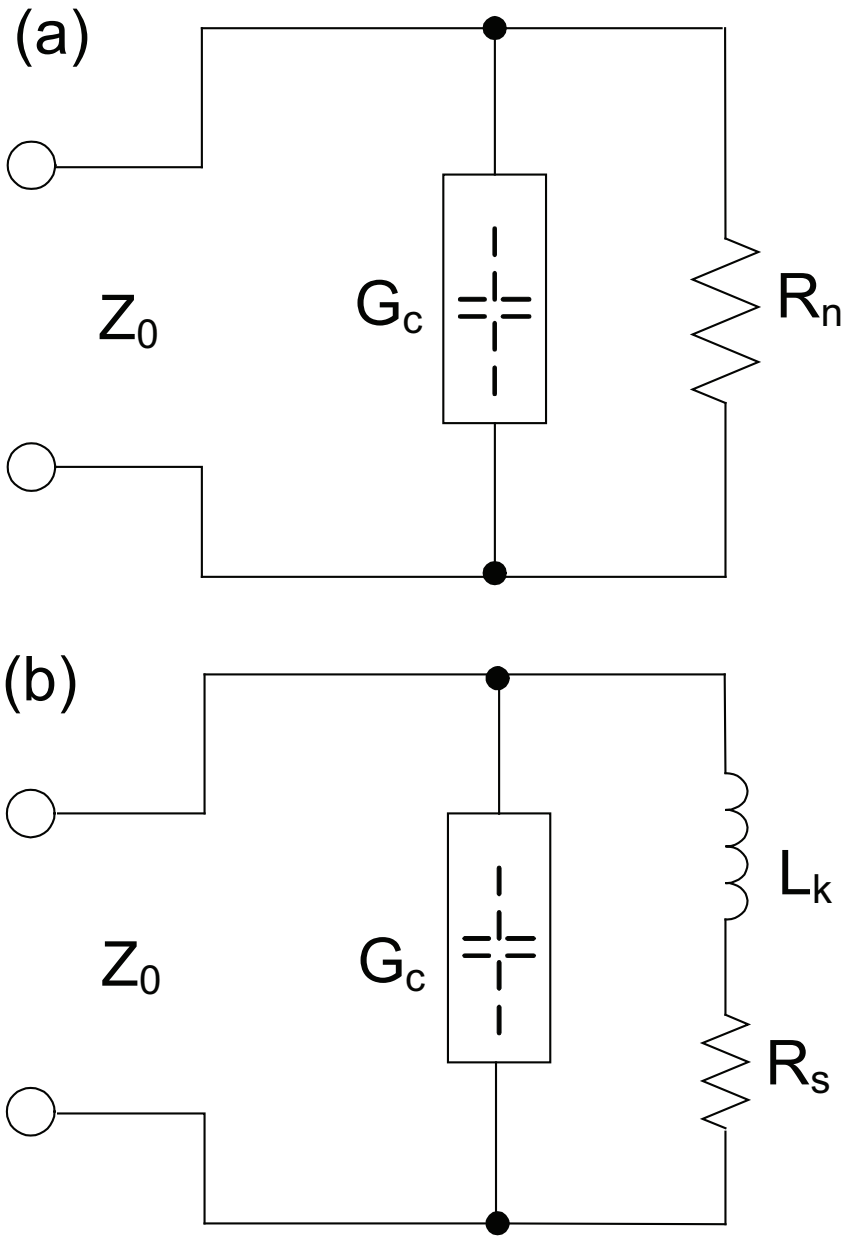

Figure 3.1: (a) Room temperature equivalent circuits; (b) Low temperature 4.2K equivalent circuit.

$1-(T/T_c)^4$ like relation based on kinetic inductance-temperature measurement. We will elaborate how to achieve the estimation in later sections. The exact critical current density varies with different DUTs, but all are in the range above $10^6 A/cm^2$.

Since the measurement has to be performed in a packaged device, while the active area of nanowire is relatively small, any distributed effect must be taken into account, including geometrically induced magnetic inductance and capacitance, which are in addition to the kinetic inductance L_k. The former most likely arises from interconnection wires; the latter has been reported either originating from the stray capacitance [78, 88], or from the dc bias circuitry [89]. In addition, when the device is dc biased, either with or without the presence of an RF signal, some resistance possibly due to either phase slips or Joule heating may present along the nanowire [90]. We model such lossy contributions by a resistance term of R_s in series with L_k. Therefore, the construction of an equivalent circuit model, which helps to exclude these unavoidable elements, becomes the key to accurately measure L_k, under conditions of both current and voltage bias schemes.

Fig. 3.1 shows the circuit model at both room and cryogenic temperatures. The procedures to determine values of C, L_k and R_s are deduced from the model, provided that we know the impedance Z_0 of transmission line, and room temperature resistance R_n (usually between 1.5 to 2 MΩ) of the NbN nanowire meanderline. The two-step procedure comprises room and cryogenic temperature S-parameter measurements. Firstly, we perform a room temperature one port S-parameter measurement to find the value of lumped reactance stemming from geometrical factors. The equivalent circuit is illustrated in Fig. 3.1 (a). Fig. 3.2 shows the results of the S-parameter measurement. From the plot, one can find a phase lag whose angle is proportional to the testing frequency. For mathematical simplicity, the phase angle is expressed in wrapped format at ±180°. The phase angle in fact constantly decreases with each increment of measuring frequencies. Such observation confirms that a capacitance does exist. The value of such capacitance can be well evaluated at frequencies of a few hundred MHz, typically at 100 MHz, to avoid errors arising

from magnetic inductances.

Note that two assumptions have been made here:

1. The magnetic inductance L_m has not been taken into account. Fig. 3.2 displays two resonance frequencies at room temperature measurement. Based on the plot, one can estimate the magnetic inductance L_m to be less than 1 nH, which is not subject to the presence of L_k. In comparison with the kinetic inductance L_k of the nanowire of interests, we estimated L_m is less than 1% of L_k. However, it can become significant when very high RF frequency is applied, typically above 5 GHz. In the frequency range below 300 MHz, where our measurements were made, neglecting L_m should not cause any error in the final results of our measurements.

2. One should be aware that the origin of R_s is not entirely clear yet, but it is definitely different from a stable hotspot resistance, especially when the resistance in the voltage bias scheme, after the critical current point. Quasi-particle excitation is most probably responsible for R_s in this range, where electrically spontaneous relaxations can be observed, and L_k exhibits less than three times L_{k0} (the zero bias L_k) change. Beyond this range, where a stable hotspot has formed, we observe an abrupt L_k variation, associated with a similar style of resistance change. We suspect that the long range coherence of the order parameter has been quenched; a hotspot will thus develop by the process of self Joule-heating.

Based on these assumptions, we conclude that the impedance of the capacitance is dominant (illustrated in Fig. 3.1 as G_c), while the impedance due to the magnetic inductance is negligible in comparison with the impedance of kinetic inductance L_k, at low frequencies typically below 300 MHz. Secondly, when we cool down the packaged NbN meanderline to the cryogenic temperature, the corresponding circuit model is depicted in Fig. 3.1 (b). Assuming that the capacitance (G_c) keeps constant, the kinetic inductance L_k in series with R_s can be determined by performing a similar one port S-parameter measurement.

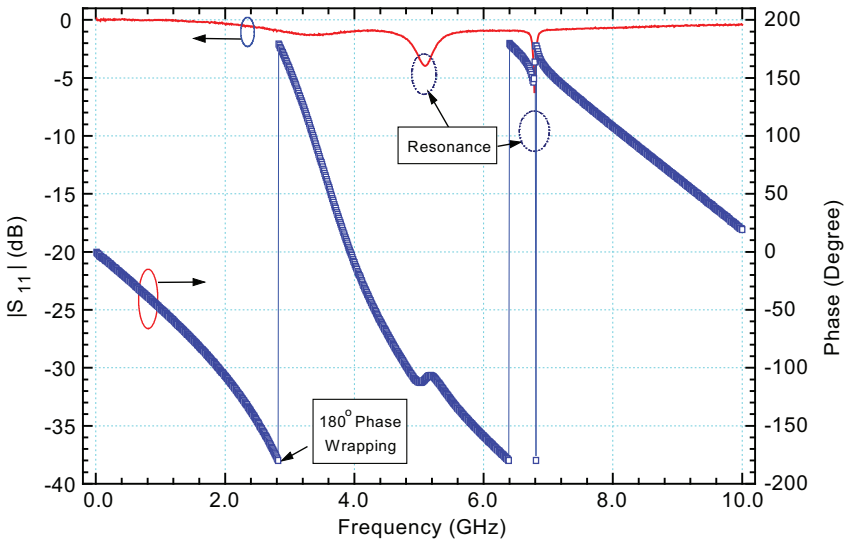

Figure 3.2: Room temperature S-parameter measurement, the phase trace (denoted as hollow blue squares) is wrapped at every $\pm 180°$ angle.

3.1.2 Scattering Parameter Analysis

Elements of the circuit model shown in Fig. 3.1 are determined based on S-Parameter (S_{11}) measurement, which can be done by a Vector Network Analyzer (VNA) in a certain frequency range. The inputs of the following mathematical relations are from S_{11} measured at both room and cryogenic temperatures.

The S_{11} can also be expressed as the reflection coefficient Γ. At each given frequency ω, the magnitude $\rho = |\Gamma|$ and phase angle θ can be written as $\Gamma = \rho e^{i\theta}$. We can define the complex conductance G_c as the termination of the transmission line whose characteristic impedance is 50 Ω

$$G_c = \frac{i\,(\Gamma - 1)}{\omega\,(\Gamma + 1)\,Z_0}. \tag{3.1}$$

where $Z_0 = 50\Omega$, and the complex $G_c = C - \frac{iG_n}{\omega} = C - \frac{i}{\omega R_n}$. The capacitance and the normal state resistance in parallel can be obtained by the knowledge of S_{11} measurement in the room temperature as

$$C = \frac{-2\rho \sin\theta}{\omega Z_0\,(1 + 2\rho\cos\theta + \rho^2)}, \tag{3.2a}$$

$$R_n = \frac{Z_0\,(1 + 2\rho\cos\theta + \rho^2)}{1 - \rho^2}. \tag{3.2b}$$

The room temperature S-parameter measurement indicates that there exists a capacitor that plays a role in the equivalent circuit model. The contribution of this capacitance leads to the resonance behavior. When the meanderline has been cooled down to its superconducting state, the normal state R_n becomes the combination of a kinetic inductance L_k and a series resistance R_s. The series resistance has very small values when the bias current is lower than the critical current I_c. We introduce a complex resistance Z_{Lk} to represent the circuit components when the NbN nanowire is in the superconducting state. It comprises the contribution from the kinetic inductance L_k and the series resistance R_s. The relation between the measured S-parameter S_{11} or Γ and the capacitance C to obtain Z_{Lk} is expressed as

$$Z_{Lk} = \frac{i\left(\Gamma + 1\right) Z_0}{\omega\left[\left(1 + iZ_0\omega C\right)\Gamma - \left(1 - iZ_0\omega C\right)\right]}. \tag{3.3}$$

After obtaining Z_{Lk}, the kinetic inductance $L_k = \mathrm{Re}\left(Z_{Lk}\right)$ and series resistance $R_s = -\omega \mathrm{Im}\left(Z_{Lk}\right)$ can be measured by separating the real and imaginary parts of the complex Z_{Lk}. With the increased value of R_s, the resonance frequency deviates from the undamped LC resonance frequency ω_o ($\omega_o = \frac{1}{\sqrt{L_k C}}$) as illustrated in the Fig. 3.1 (b). The deviation of ω_o degrades to the damped resonant frequency ω_d

$$\omega_d = \omega_o \sqrt{1 - Q^{-2}} \tag{3.4}$$

where the Quality factor Q can be calculated through the relationship $Q = \frac{1}{R_s}\sqrt{\frac{L_k}{C}}$.

3.2 Experimental Results of Kinetic Inductance Measurement

3.2.1 Experimental Setup and Measurement Principle Procedures

The RF/Microwave characterization system of the packaged NbN meanderline employs an Agilent E8364B PNA Network Analyzer (10 MHz to 50 GHz), a Pasternack

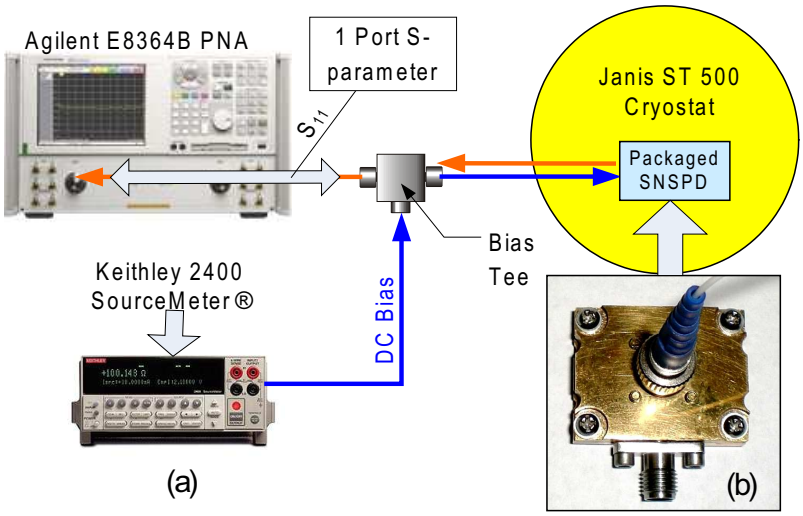

Figure 3.3: The experimental setup for the measurement of circuit model elements: (a) The configuration diagram, (b) The photograph of the packaged SNSPD.

bias Tee 10MHz-6GHz, a Keithley 2400 SourceMeter, and a Janis ST-500 cryostat. Their connection is illustrated in Fig. 3.3 (a). The DUT is packaged in an ETP copper housing equipped with a 40 GHz bandwidth k-connector to maintain the high frequency performance free from the cryogenic temperature stress. The k-connector dielectric layer is made of air/vacuum rather than Teflon in SMA connectors that suffers contraction. In addition, the dielectric constant of Teflon may vary such that it may lead to unwanted variation of the port impedance. The packaged housing is first plated with nickel followed by gold to improve the thermal conduction with the cryostat cold plate. The NbN meanderline is electrically connected by silver epoxy to glue one contact pad to the microwave center pin, and the remaining two pads to the wall of the housing. The final result of the device package is shown in Fig. 3.3 (b).

The measurement assumes that any extra time delay arising from interconnections within the device packaging is negligible, because of two considerations: (1) The S-parameter S_{11} can be technically measured at only the reference plane, located at input/output port of the packaged NbN meanderline. The reference plane is set by calibration with VNA; (2) The working wavelength (in meters) is much

longer than the total electrical wire length (in one hundredths of a meter) including the packaging and the coplanar waveguide on the substrate. Thus, the circuit model in conjunction with its mathematical description has been justified.

It is challenging to do S-parameter measurement under cryogenic temperature and high vacuum because of two limiting factors: (1) We have to limit the amplitude of the ac signal to avoid the device latching when the dc bias is very close to its critical point; (2) The interconnection loss along the transmission line, especially the connector loss, weakens the reflected power. As a result, the ratio of signal to noise becomes extremely low. Since the standard one-port calibration can be performed only in the range of room temperature (approximately 25-30 °C) and pressure (10^3 mbar), the forward tracking error terms in a standard one-port calibration algorithm can not be kept accurate enough, because the portion of the measuring coaxial cable has been cooled far below its calibrating temperature; and has been placed in an ambient of high vacuum condition ($< 10^{-5}$ mbar).

We have observed that the amplitude of Γ in the frequency range experiences about 0.1 dB variation on average. According to our calculation, R_s should be very sensitive to $|\Gamma|$ when the dc bias current is very close to zero, because R_s is expected to be very close to zero. The associated phase angle variation can be approximated in the complex plane by simple geometrical relations and the result indicates the phase angle variation is less than 0.6 degree. Thus, the inductance measurement can achieve a good accuracy, even though the capacitance reduces the phase angle as a function of frequency ω.

In the experiment, we treat the bias tee and cryogenic cable as one lossy transmission line. The calibration is done by setting the reference plane to the end of the cryogenic cable, i.e. the k-connector input of the packaging. Thus, losses from the cryogenic cable, the bias tee and interconnecting components, which are in the ambient temperature, have been compensated by the calibration. The calibration frequency ranges from 10 MHz to 300 MHz. The dc bias source is programmed in either current or voltage mode. The microwave probing power is set at -76 dBm,

corresponding to 1 μA peak-to-peak ac current at a 50 Ω coaxial cable. However, considering the cryogenic cable loss, the effective ac current amplitude at the device side falls to about 0.25 μA, which poses much less perturbation to the system during the measurement. Meanwhile, we have observed that when the frequency is higher than about 70 MHz, the S_{11} magnitude variation due to the incident microwave signal becomes negligible. Therefore, the measurement of circuit elements L_k, C and R_s starts with S_{11} frequency points higher than 70 MHz and averages them to the upper frequency limit (in this measurement it is 300 MHz).

Moreover, the choice of calibration power is -30 dBm, whereas the measurement power is set to -76 dBm. This calibration power level is chosen by considering that the minimum noise floor for this VNA preamplifier is -110 dBm. If the calibration power is too low, the forward tracking error term can not be well resolved after the calibration. We can use the data track smooth algorithm as well when we switch the power level down to -76 dBm. However, the smoothing data track can not lead to a higher signal to noise ratio. Instead, we can reduce the *IF bandwidth* to 10 Hz to increase the measurement accuracy. Based on our experiment, further decreasing *IF bandwidth* has no appreciable improvement. In addition, *stepped frequency scanning* is adopted in lieu of the default adaptive scan mode. Each stepped frequency has a 1 ms delay to make sure no residue power affects the adjacent frequencies.

3.2.2 Kinetic Inductance Measurement Results

Initially, we apply the current bias scheme in the measurements. Fig. 3.4 shows the measured kinetic inductance for two identical packaged devices, made of NbN nanowire meanderlines. Both measurements of L_k have been normalized to their zero bias kinetic inductance, respectively. The capacitance has been measured in the room temperature via one port S-parameter measurement. The measured capacitance after postprocessing indicates that its value is device dependant. In this work, the capacitance for higher quality film nanowire is 1.6 pF; whereas for the

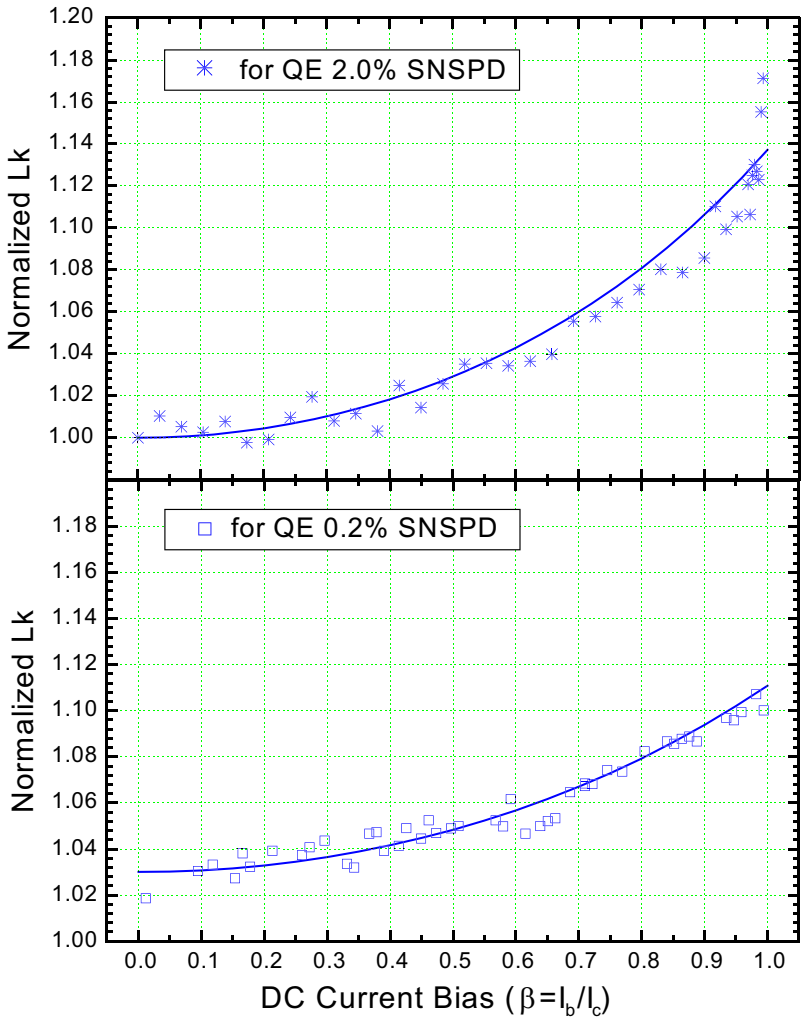

Figure 3.4: The measured kinetic inductance for two NbN nanowire meanderlines with different film quality; solid lines are results from theoretical simulations.

lower film quality [1] one, its capacitance is 1.4 pF. On the other hand, the former has zero bias kinetic inductance at about 210 nH; while the latter is 230 nH. In both cases, the nonlinear kinetic inductance displays a trend of higher L_k associated with a higher bias ratio. Detailed discussions on the theoretical background are presented in Appendix A. The relationship of L_k with respect to the bias current ratio is given by (3.5); and the simulation results are plotted as solid curves in Fig. 3.4.

However, neither in this work nor in the relevant literatures [59, 65] have shown any abrupt change of L_k when the dc bias current is very close to the so-called critical current I_c, even when we are able to drive the bias current ratio above 99%. Since the kinetic inductance L_k by definition should be inversely proportional to the Cooper pair density of the nanowire condensate, this seems to imply that the I_c may only be a local effect, possibly a resistive spot somewhere along the nanowire. Further increasing the bias current above I_c will cause device permanent latching .

Based on the preceding analysis, we switch our dc bias scheme into voltage bias. Now all of the measurement conditions are kept the same except the bias method. Fig. 3.5 demonstrates the linkage between the different I-V regimes and the kinetic inductance L_k of the NbN meanderline. The curve shows that even when the bias current decreases after I_c, the kinetic inductance increases constantly with the increasing bias voltage. This suggests that Cooper pairs are proportionally accelerated by applied voltages without apparent resistance barriers along the meanderline path, until the hotspot formation plateau occurs. At that transition point, the kinetic inductance changes very abruptly to 1500 nH at 4.2 K. In order to see the connection of the increasing kinetic inductance L_k with the series resistance R_s, Fig. 3.6 shows the measured L_k and R_s at each bias voltage point. The figure suggests that when the bias voltage surpasses the point where I_c occurs, both L_k and R_s follow the same trend of a constant increment, due to dissipations caused

[1] The higher SNSPD QE, the better film quality. So the better thin film quality one is equivalent to higher QE SNSPD.

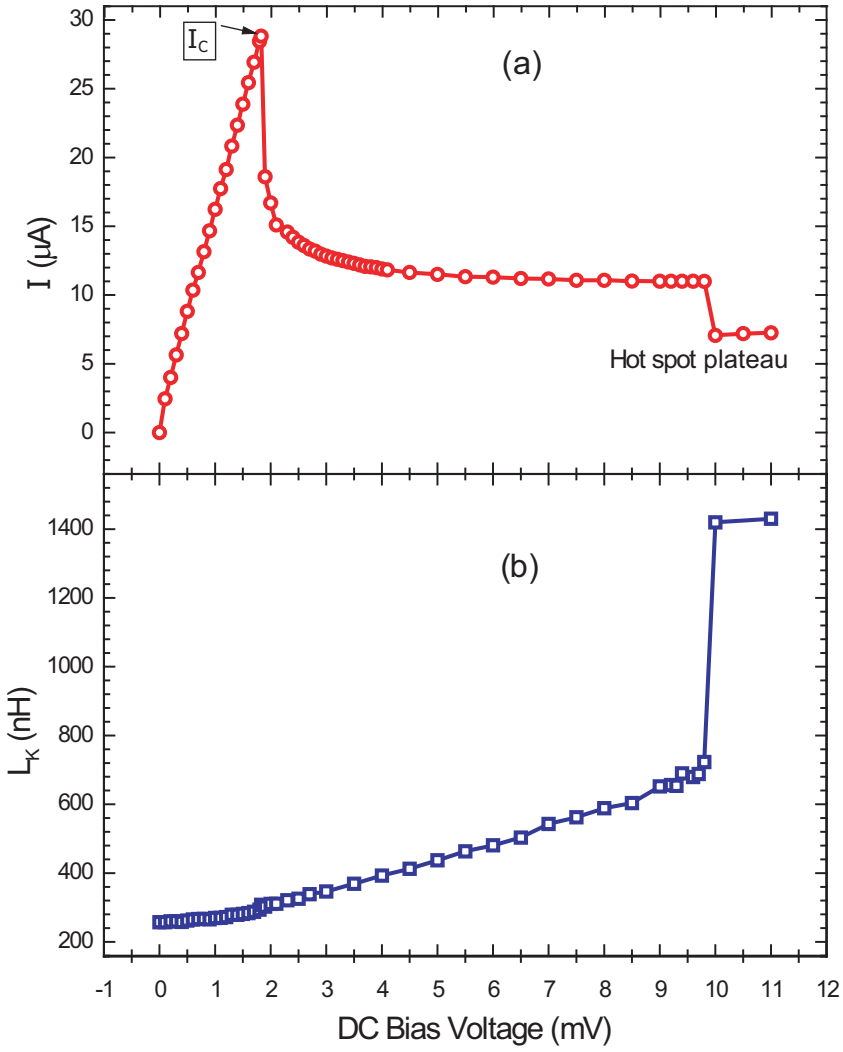

Figure 3.5: The linkage of the I-V scan and kinetic inductance variation, (a) the I-V curve under voltage bias scheme; (b) the measured kinetic inductance L_k.

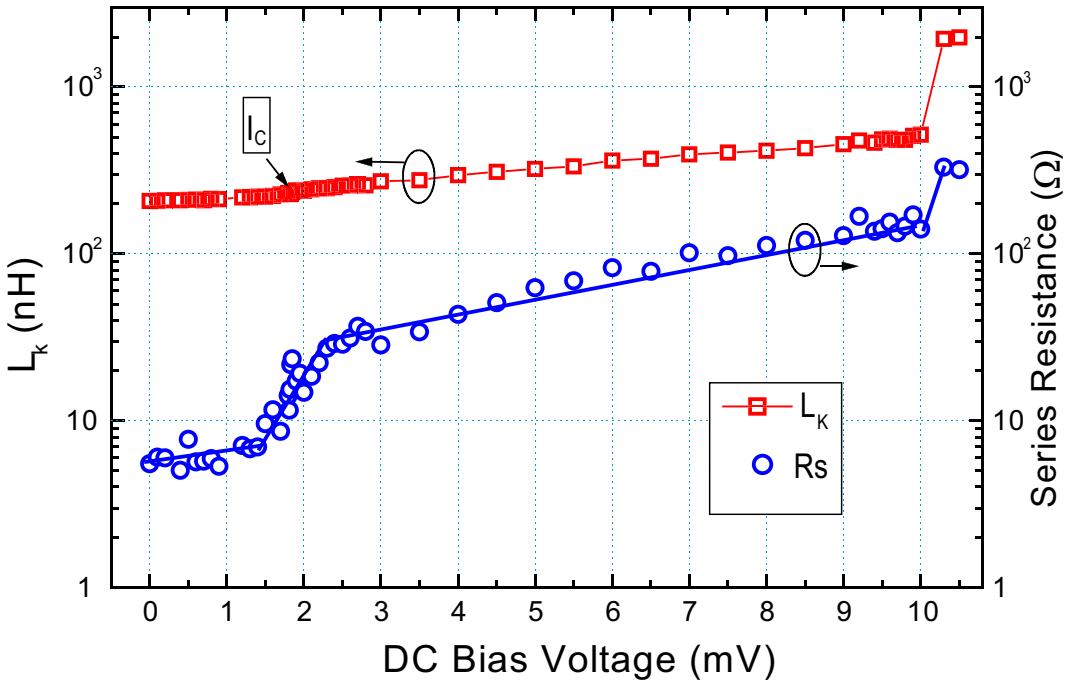

Figure 3.6: The measured kinetic inductance and series resistance under the voltage bias scheme for the SNSPD whose QE is 2%.

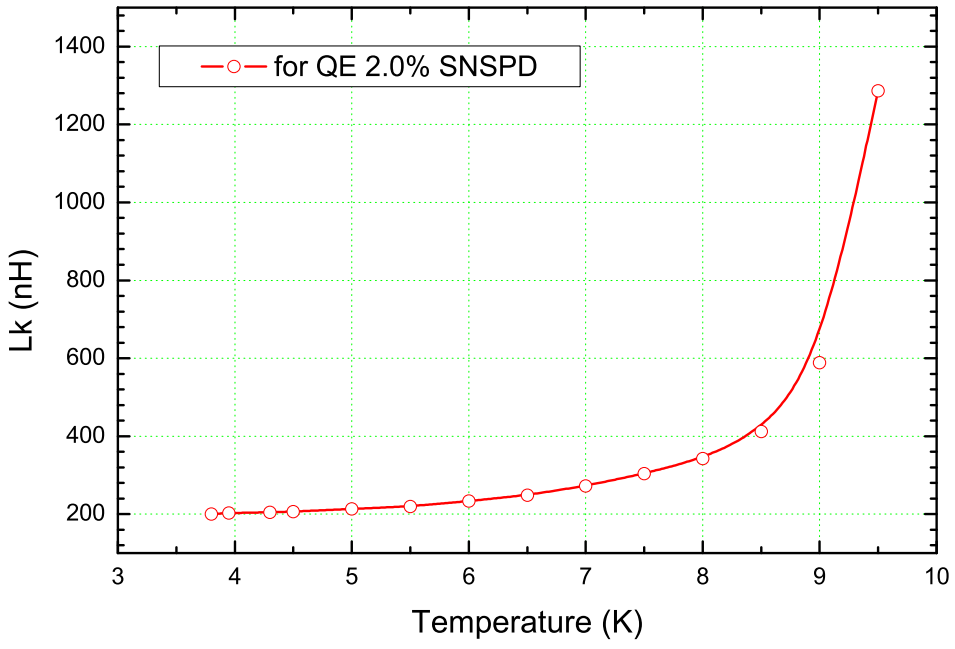

Figure 3.7: The measured kinetic inductance by varying the thermal bath temperature in the absence of optical irradiations.

by the quasiparticle excitation. At lower dc bias, such dissipation is weak, so R_s is negligible. R_s increases smoothly from zero to a quasi stable value close to 120 Ω prior to the formation of an initial hotspot, whose stable value is about 500 Ω. This process can *not* be found in the dc current bias scheme. Instead, when it is switched to the voltage bias, we observe a continuous transition for kinetic inductance L_k and series resistance R_s. They both display an abrupt change at the point where the dc bias current drops below the return current I_{ret}, as shown in Fig. 3.5(a). The abruptly changed value of R_s is in the range of the hotspot resistance R_h. Very large variations of L_k (more than four times $L_k(\beta = 0)$ have been observed, and show good agreement with the Ginsburg-Landau (G-L) theory prediction [78], when R_s becomes comparable with the R_h. Such experimental observation suggests that when the NbN nanowire meanderline is used as SNSPD, its photon-response due to the formation of hotspot strongly correlates to the abrupt change of kinetic inductance.

We performed the L_k measurement by changing the DUT temperature. The temperature is monitored and controlled by the Lakeshore 332 two channel temperature monitor/controller. This temperature controller is equipped with two independent channels of heater and thermal sensor interface. The helium flow of the cryostat is also adjusted in order to track the change of temperature and to keep the temperature of the ST-500 cold plate as stable as possible. The temperature has the fluctuation less than 0.1 K. We average our measurements over one particular temperature for multiple times to reduce the uncertainty.

The same one-port S-parameter measurement as what we have performed in the first section is undertaken. L_k is measured as a function of temperature T. The result is depicted in Fig. 3.7. The open circle in the plot is the experimental measurement; the solid line is the fitting curve using a asymptotic relation of $1 - (T/T_c)_0^{\alpha}$. We take $\alpha_0 = 4$, and $T_c = 10.4K$ for the best fit to the measurements.

3.2.3 The Resonating Circuit Analysis

To further confirm the validity of the R_s-L_k-C circuit model and the related model parameter measurement, one can resort to resonance frequency measurement, i.e. by looking at the frequency points where the phase angle of S_{11} is zero. In this case, the load at the end of the transmission line has no imaginary component. The undamped resonance happens when R_s is zero or negligibly small. What is important for this work is that the damped resonance frequency ω_d deviates from the undamped resonance frequency (ω_o) governed by Eq. (3.4), due to large values of R_s. Fig. 3.8 shows the experimental results of the phase with different frequencies of the RF/microwave excitation signals under different bias voltages. The values of L_k and R_s for each branch can be found in Fig. 3.6.

Fig. 3.9 displays the extracted quality factor as a function of bias voltage. The plot indicates that the quality factor for this photon detector is not high. Unlike the high-Q resonator detection mechanism, the highest Q of the SNSPD is less than 100 at 4.2K. We think that it is beneficial for the fast resistive state formation. The Q-value is expected to increase with lower temperatures than 4.2 K, but it makes the transition from superconducting to resistive state hard. Therefore, experimentally the QE of SNSPD has not been reported to be further improved when its operating temperature is below 1.8 K.

Table 3.1 tabulates the calculated undamped resonance frequency (ω_o) and the directly measured damped resonance frequency (ω_d). The corresponding Quality factor Q is obtained by both methods of damped resonance frequency, and the Q factor is defined as the function of L_k, R_s and C. The comparison of both approaches shows a good agreement when R_s is relatively large, e.g.$> 100\Omega$. The resonating R_s-L_k-C circuit does not display any absorption dips at the resonating frequencies, if we focus just on the amplitude of S_{11}, because of two factors: First, the equivalent circuit shown in Fig. 3.1(b) is neither a parallel nor a serial typical RLC resonating circuit as depicted in [91]. One can convert our equivalent circuitry into a typical parallel R_s-L_k-C resonator circuit by invoking circuit theories, but

Table 3.1: Measured resonance frequencies and kinetic inductance.

Voltage	L_k	Undamped $f_0 = \frac{1}{2\pi\sqrt{L_k C}}$	Damped Exp. resonance f_d	Q-factor[a]	Q-factor[c]
(mV)	(nH)	(MHz)	(MHz)	Q	Q
9.0	456.00	186.33	153.40	1.75	4.15
8.0	415.16	195.28	192.25	5.56	4.52
7.0	395.50	200.07	200.65	12.50 [b]	4.90
6.0	362.13	209.09	217.45	3.45 [b]	5.75
5.0	323.69	221.15	223.75	6.67 [b]	7.18
4.0	297.35	230.74	230.5	12.5	9.93
3.0	272.66	240.96	240.55	16.67	14.46
2.6	257.50	247.95	246.85	11.11	12.80

a. The quality factor Q is calculated by $Q = \left(\sqrt{1 - \left(\frac{f_d}{f_0}\right)^2}\right)^{-1}$.

b. Absolute value $\left|1 - \left(\frac{f_d}{f_0}\right)^2\right|$

c. The quality factor Q is directly obtained by the definition $Q = \frac{1}{R_s}\sqrt{\frac{L_k}{C}}$

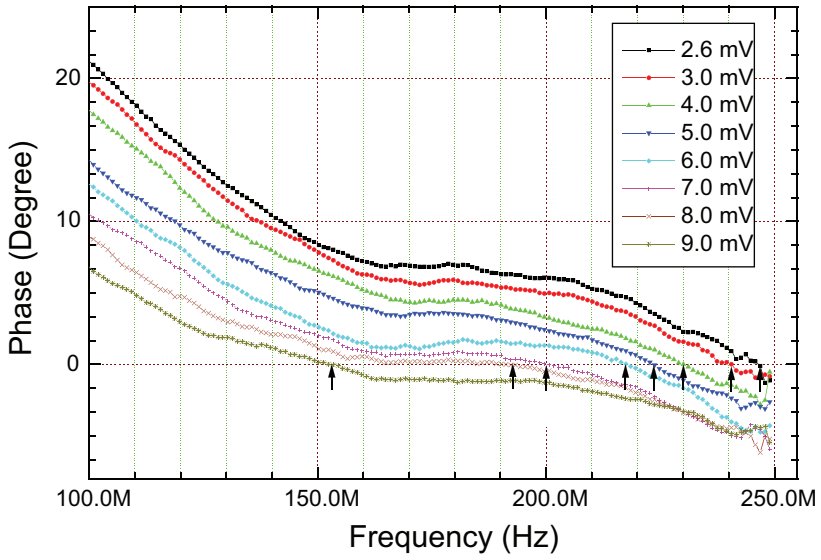

Figure 3.8: The measured kinetic inductance and series resistance under the voltage bias scheme for the SNSPD whose QE is 2%, the arrows indicate frequency points of each damped resonance.

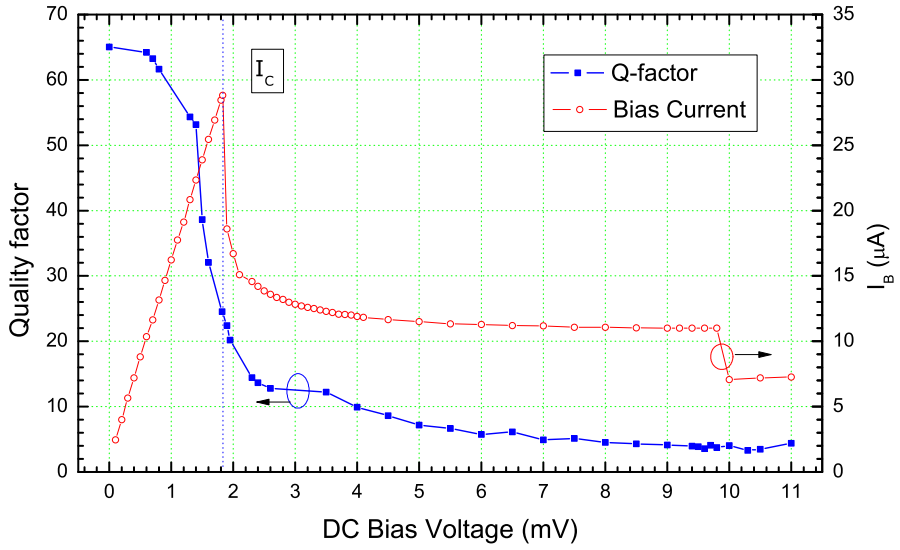

Figure 3.9: The quality factor -Q of the equivalent R_s-L_k-C circuit as the resonating circuitry

the converted parallel resistance becomes considerably larger than the 50Ω transmission line impedance, resulting in a pure parallel L_k-C circuitry approximately. Second, at the non-resonating frequencies, the total impedance of our equivalent circuit becomes primarily reactive, so the unitary reflection will be most probably measured.

3.3 Ginsburg-Landau Relation for Kinetic Inductance and Bias Current

In the past, many experimental measurements showed that (a). in dc I-V measurement, even at 4.2 K, there is a non-trivial dc current dissipation, i.e resistance, (b) the residual resistance close to 20 K has the highest value compared with that at room temperature, with resistivity of 200 $\mu\Omega$-cm. To seek more insights, we explored extensively in the relevant literatures; and two well-established evidences have been brought to our attention:

1 The fabrication process of NbN thin films involves sputtering pure niobium target in a mixed gas flow of nitrogen and argon [92]. The film properties have been studied microscopically in [93]-[94], in order to systematically show the weaklink properties of NbN thin films. The electrical properties of NbN thin films have been studied in [95]-[96]. Based on values of the normal state resistivity, which is in the range of some 200 $\mu\Omega$-cm, granular boundaries inherently existing in NbN thin films were attributed to tunneling weaklinks. Very interestingly, ref. [95] gives a good approximation to the critical current density based on quasiparticle tunneling by Ambegaokar *et al.* [97]-[98]. We have found out that the normal state resistivity of the nanowire is about 200 $\mu\Omega$-cm, which is the range of granular tunneling range at 20 K regime as discussed in [95]-[96].

2 Microwave nonlinear surface resistance Z_s: NbN has been long employed in

microwave applications, primarily useful for making transmission lines and resonators. The power handling capability of such devices has been a topic for many decades [99]-[101]. The nonlinear dependency of the surface resistance has been attributed to the granular nature of NbN thin films [80], [99]-[101], that has been prepared by the RF sputtering technique. The dependency has been modeled on the basis of tangential magnetic field that is parallel with the superconducting surface. The model involves magnetic field penetration depth. This does not seem applicable to our case directly, because the DUT acts only as a lumped load; but the dissipation of microwave power by granular boundary remains the same mechanism to account for the nonlinearity.

Additionally, we also calculated the phase-slip induced I-V relationship at the transition from the superconducting state to the normal state when the temperature increases across the transition temperature T_c. The exponential increase of resistance indicates the pronounced existence of phase-slip centers in the nanowire meander-line. We suspect that these phase slip centers stem from the granular boundaries during the formation of thin film. It is well known about the process of sputtering thin films. Some seeds of metallic grains expand and gradually merge into one continuous film. Thus, we conclude that the superconducting nanowire is patterned on such thin film and its weaklink effect has to be considered in almost every testing, such as dc I-V and RF/microwave measurements.

Thus, we heuristically conclude that the strong-weaklink network [80], or inhomogeneities of the order parameter in one dimension superconducting nanowire, is responsible for both nonlinear kinetic inductance and resistance. The amplitude of complex order parameter has been reduced on average, allowing the G-L equation to be valid in a wider temperature range, e.g. at $0.5T_c$.

We have developed a relation of current bias ratio with respect to kinetic inductance L_k for a clean, uniform bulk superconducting 1-D wire, with the absence

of magnetic field, in [78], and the analytical solution reads

$$L_k(\beta) = \frac{L_{k0}}{1 - 4\cos^2\left(\frac{\pi}{3} - \frac{1}{3}\arctan\left(\frac{\sqrt{1-\beta^2}}{\beta}\right)\right)} \tag{3.5}$$

where L_{k0} is the zero bias kinetic inductance. It is device dependent, and can be measured via the method in this paper when the setting dc bias to zero. $\beta = {I_b}/{I_c^{GL}}$ is the ratio of dc bias current I_b to that of bulk critical current I_c^{GL}. Since the order parameter has been reduced due to the strong weaklink network, the (3.5) is valid for temperature at 4.2 K. However, attention has to be paid to the fact that $I_c^{GL} \gg I_c$, where I_c is defined as the critical current in the context of SNSPD. In terms of thin film quality, or QE of a given SNSPD in the literature, we substitute β with $\beta_b = \gamma\beta$, in which γ is a figure of merit of the thin film quality, defined as $\gamma = \frac{I_c}{I_c^{GL}}$, and $\beta_b = \frac{I_b}{I_c}$.

Note that technically I_c^{GL} can not be measured directly, but can be deduced through the ratio of $\frac{L_k(\beta_b)}{L_{k0}}$ when $\beta_b \simeq 1$ based on the relationship of (3.5). Evidently, the highest γ can be close to 0.6 at temperatures of 4.2 K . It would become relatively higher when the temperature is decreased, but we anticipate that γ will saturate at some point due to the possibility that the weaklink will limit I_c from going close to I_c^{GL}. For two of our DUTs, the higher quality one has $\gamma = 0.5$; and $\gamma = 0.4$ for the lower one.

Finally, the effort to account for nonlinear resistance is more complicated, because it involves combinations of material, processing, electrical and thermal physics. The difficulty is added because of the quasiparticles are involved in the presence of RF field. The strong fluctuations of R_s result not only from the quasiparticle generation and recombination process, but also from their tunneling through the weaklinks. We think that detailed discussions are much beyond the scope of this thesis, and we will address this topic in the future works.

Table 3.2: Computed superconducting material parameters

Parameter	SNSPD # 1[1]	SNSPD # 2[2]
J_c (A/m^2)	6.2×10^{10}	3.7×10^{10}
L_k (nH) [3]	200	230
ρ $(\mu\Omega \cdot cm)$	195	214
λ_L (0) (nm)	383	411
λ_{GL} (0) (nm)	400.7	407.9
λ (0) (nm)	490.6	499
ξ_0 (nm)	6.18	5.91
l_{tr} (nm)	3.97	4.00
κ_{GL}	70.88	73.45

[1]Device QE is 2%

[2]Device QE is 0.2%

[3]Extracted at $T = 4.2$ K with $T_c = 10.4$ K for all calculations

3.4 NbN Superconducting Thin Film Properties

We treat superconducting nanowire devices as a nonlinear load of a 50 Ω transmission line. The incident RF/microwave power (ac current) is weakly applied. The reflected power is measured and analyzed as discussed in the preceding sections. Series of experimental results to measure kinetic inductance L_k to study the nonlinearities stemming from dc bias by one port S-parameter measurement. The weak ac current was used (less than 1 μA) as a probe for all measurements.

By knowing the kinetic inductance of the superconducting nanowire via the method described in the preceding section, we are able to obtain some insights to the material properties of the superconducting parameters that is prepared for making NbN SNSPD. After post processing the measured S-parameter, we are able to retrieve London penetration depth, coherence length, and very importantly the first and second critical magnetic field H_{c1} and H_{c2}. However, the second critical magnetic field intensity can not be simply computed for NbN thin film, especially for the ultra thin film (e.g. 4 nm).

The extraction of values of the penetration depth λ is based on the relations in Ref. [102]. The normal state electron specific heat $\gamma_0 = 2.1 \times 10^{-4}\ J \cdot cm^{-3} \cdot K^{-2}$ is from [76]. All of the input parameters, including the kinetic inductance L_k in conjunction with the critical current density J_c and the normal state resistivity ρ_n at 20 K are measured parameters. We have also evaluated BCS coherent length ξ_0 and electronic mean free path l_{tr}. Interestingly, we have found that they are comparable. Consequently, all values of different penetration depth are becoming comparable accordingly, which is significantly different from the bulk properties of NbN. This exceptionally long mean free path seems to arise from the two magnitude lower electron gas density at Fermi surface than that of bulk superconductors. Table 3.2 lists all of input parameters and output results for this evaluation. Oates *et al.* [103] reported the penetration depth $\lambda(0)$ obtained from their surface impedance measurement in the microwave range. The comparison shows that our penetration depth value is in good agreement with their results provided that thin film modifies

the values of BCS coherent length ξ_0 and mean free path l_{tr}. As a result, their London penetration depth $\lambda_L(0)$ becomes considerably lower than $\lambda(0)$ due to the high ratio of ξ_0 to l_{tr}.

3.5 DC I-V Measurement in the Absence of Optical Power

The dc I-V measurement of the NbN nanowire shows four distinct regimes. The first regime is the superconducting regime and the slope of I-V curve is primarily determined by the cryogenic cable resistance; The second is the switching state [104], in which spontaneous thermo-electrical relaxation oscillations is dominantly observed; The third regime is the formation and expansion of a stable hotspot, which is the starting point of a self-heating effect. The hotspot grows up with the increment of dc bias to occupy one entire segment of the nanowire. After this point, the fourth regime is entered when one segment of the nanowire becomes a hotwire and starts to heat up the adjacent segments of nanowires.

3.5.1 Superconducting and Switched States

For the first two regimes as demonstrated in Fig. 3.10, the figure depicts the forward I-V curve obtained via two scan speeds: fast computerized scan and slow manual scan, in which the inset panel displays a typical computerized scan in both forward and backward directions. The manual mode is persistently useful for the small signal S-parameter measurements. In both manual and computerized scan modes, the return current, which manifests the plateau of a hotspot formation, shows the same value. However, the occurrence of this point in the manual scan mode is different from the computerized fast scan mode. For the former mode, it occurs at higher voltage than does the latter, but the latching current (approximately 7 μA) is almost identical. We attribute this to three possible mechanisms: scanning

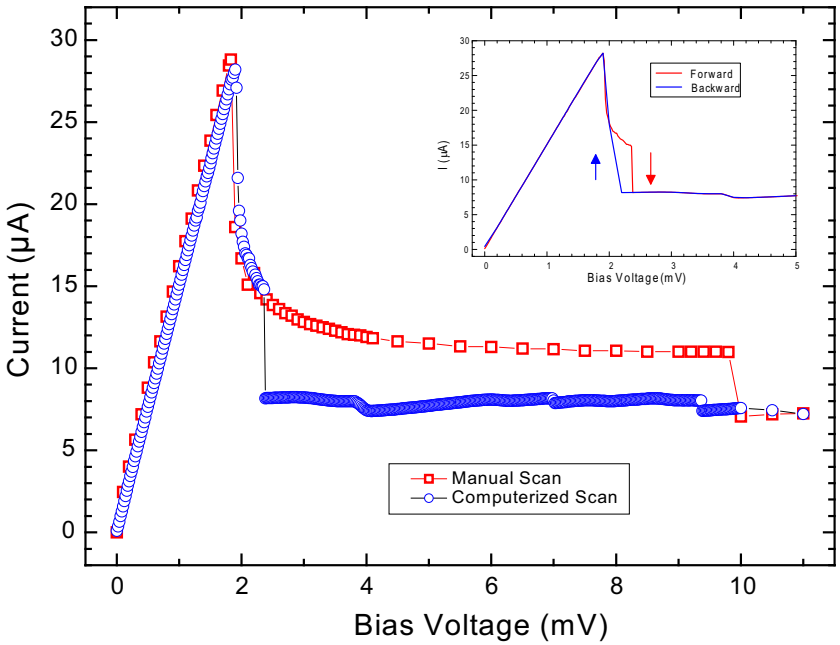

Figure 3.10: Experimental voltage and current relationship measured via both manual and computerized scan modes under forward voltage bias scheme; inset panel is a computerized scan curve in both directions.

speed, scanning direction and electrical grounding. The manual mode always has slower variation of bias voltage. The voltage relaxation induced by quasiparticle excitations results in a metastable states, which is very susceptible to external perturbations, such as a sudden bias voltage variation, and then stabilizes itself at the latching current.

In addition, the scanning direction depends on whether it starts from a higher bias voltage down to zero (backward), or vice versa (forward). Within the switched states as defined in [104], the nanowire will exhibit a hysteresis I-V curve due to the thermal healing of the hotspot, i.e. the voltage scans of the forward and backward mode show the hysteresis behavior; and the measured current remains at the level of latching current until the bias voltage decreases below the forward latching voltage point. The detail theory has been discussed by Tinkham *et al.* [90]. However, the theory can not account for the different hysteresis loops in two scan modes. We suspect that the electrically shared ground of the analog and digital

parts in the source meter is responsible for the difference. In the computerized scan mode, communication between the source meter and computer can induce extra ground voltage fluctuations. Consequently, a smaller hysteresis I-V curve results as demonstrated in the inset panel of Fig. 3.10.

The dc I-V curve measurement also indicates that when I_b is greater than $\sqrt{2}I_{ret}$, it is no longer a single value function of bias voltage. On the other hand, for any given bias voltage, there exists a single-value current. Lindgren *et al.* used to bias an HTS bridge in the switched state to measure photoresponses [104]. The values of R_s by small signal RF/microwave measurement results in less than 20 Ω, even when I_b is 0.5 μA less than I_c (28.5 μA in this case), which is much lower than the stable resistance of a hotspot by Joule heating.

3.5.2 Temperature Dependent I_c

The critical current I_c can be experimentally determined for a given SNSPD by inspecting the maximum current in Fig. 3.10. [2] The temperature dependence of I_c can be experimentally found by inspecting the maximum current in the dc I-V measurement at all temperatures. Fig. 3.11 illustrates the measured zero maximum current for the DUT with higher QE. In the figure, the dot line is a linear fitting curve, whose slope is -5.88 $\mu A/K$; the zero temperature I_c is projected to be 50.74 μA. The red square in the plot is the DUT provider measured I_c at 2 K, which is below the linear fitting trend line. When the temperature ranges from 7.5 K to 9.5 K, approximately a second slope can be observed. Higher 9.5 K, we can only measure submicron ampere current, which is hard to identify it as a maximum current. The linear relation of I_c with the decreased temperature is not consistent with what Ginsburg-Landau theory predicts in the bulk superconductors, from which we expect a relation like $I_c \propto T^{-3/2}$ curve. We attribute the linear

[2] when the bias current I_b is close to I_c, the superconducting nanowire will exhibit a considerable dc resistance primarily due to voltage spikes arising from dark count. Consequently, this will affect the accuracy of the I_c measurement, as well as latching problem in the experiment.

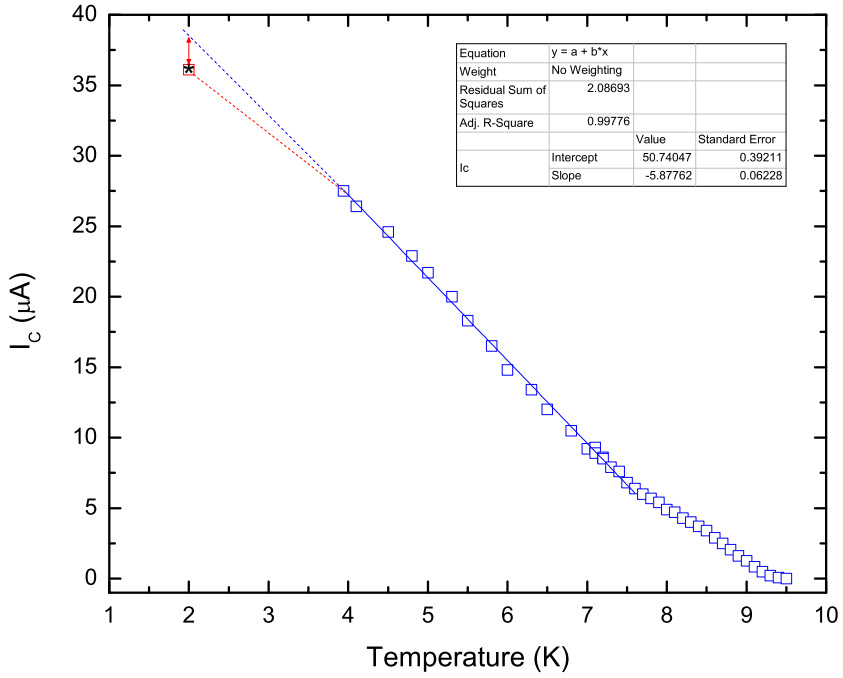

Figure 3.11: The zero voltage maximum current, or critical current I_c vs temperature dependence for the SNSPD of higher QE.

relationship of $I_c(T)$ particulary exhibited in the SNSPDs to the NbN thin film, in which the superconducting weaklinks formed during its fabrication process.

The NbN thin film is sputtered on sapphire substrates; and is studied in [95]-[96]. The weaklink inherently presents during the ultra thin film sputtering, due to the formation of granular grain boundaries. Kampwirth *et al.* [95] approximated the critical current based on the quasiparticle tunneling, which is studied by Ambegaokar [97]-[98]. We can relate I_c to the granular size of the NbN thin film a_0

$$a_0 = \frac{\pi A \Delta(T)}{2 I_c q_e \rho_{20K}} \tanh\left[\frac{\Delta\,(T)}{2 k_B T}\right] \tag{3.6}$$

where k_B is the Boltzmann constant; q_e is the electron charge; $\Delta(T)$ is the temperature dependent BCS energy gap; A is the cross section area of the nanowire, and ρ_{20K} is the resistivity and will be addressed later in this section. The value of a_0 provides a quantitatively commencement point in the self-heating model for the SNSPD nanowire that will discussed next.

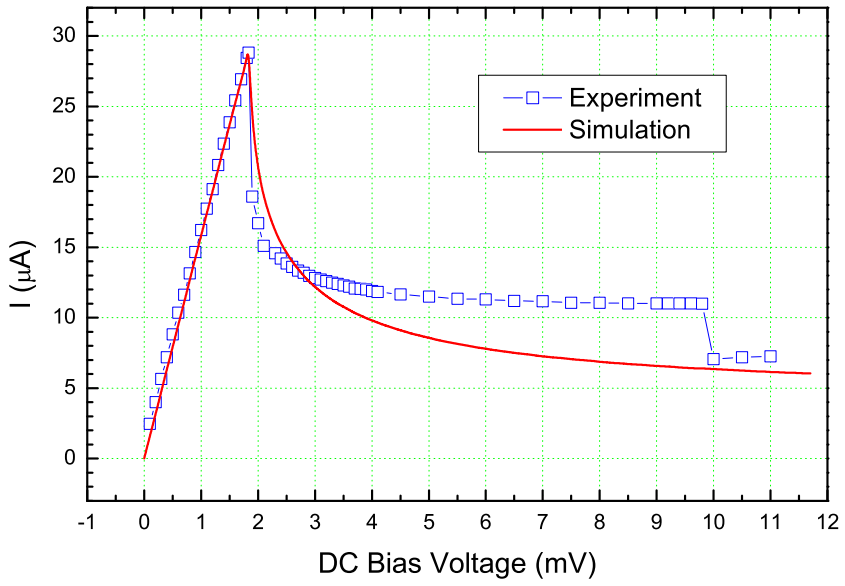

Figure 3.12: The simulated dc I-V scan by voltage bias in superconducting and switched states

3.5.3 Modeling of Superconducting and Switched State

The I-V curve shown in Fig. 3.5 (a) prior and after the critical current I_c point, is the superconducting and switched state [104], respectively. For the latter, it is characterized by a spontaneous relaxation oscillation at about 800 KHz counting rate, when we use the method to perform photon/dark count characterization in the preceding chapter.

Hadfield *et al.* [105] suspected about 5000 Josephson Junction-like behavior exhibited in their SNSPD, which has the identical geometrical size as that of our DUT. It is actually in consistency with what we calculated based on what Kampwirth [95] estimated about the single granular size of 100 nm. We further developed a lump 5000-stacked Josephson Junction circuit model to simulate to the total current driven by a voltage source. The voltage source spans from 0 to 10 mV. The simulation results is plotted in a solid curve in Fig. 3.12. The comparison to the experimental result in the figure indicates that the simulation does not display a relatively flat current in the switched state. This is primarily due to the fact that the spontaneous voltage oscillation at about 800 KHz has not been considered in

the simulation. The strong voltage pulses can act as another resistance, which is beyond our stacked Josephson Junction model.

3.5.4 Modeling 1-D Self-Heating

We are not able to observe any relaxation oscillations when the device is latching. We believe that when the bias voltage is higher than the latching voltage point, the nanowire formulates a non-reversible hotspot that can not be thermally healed by the heat bath. Then the nanowire is believed to enter the third regime dominated by self-heating effect.

Carefully examining the I-V curve in Fig. 3.13 (a) and (b), we notice that there exist a series of zigzag current fluctuations with the increment of bias voltage. We anticipate that the self-heating hotspot expansion along one segment of the nanowire is quantized as resistance staircases. We suspect that those resistive steps are associated with granular nature of the ultra thin NbN thin films.

With the increment of dc voltage bias, a stable hotspot will develop at a certain section of the nanowire. The voltage width of the switched state depends also on the scanning direction and mode. Usually manually increasing the voltage will result in an accurate voltage point of the hotspot formation. Upon its formation, thermo-electrically Joule heating will apply. The first segment of the nanowires gradually exhibits normal state I-V properties as the dc bias voltage increases. The self-heating model by Skocpol *et al.* [75] is the best to account for this physical process. The current and voltage as the functions of the hotspot size χ_0 are

$$I_b(\chi_0) = I_r \sqrt{1 + \coth\left(\frac{\chi_0}{\eta_S}\right) \coth\left(\frac{\chi_0}{\eta_S} - \frac{L}{2\eta_n}\right)} \tag{3.7}$$

$$V_b(\chi_0) = I(\chi_0)\, \chi_0 \rho_{20K}/Wd \tag{3.8}$$

in which we treat the thermal healing length η_S to be the same as η_n. The simulation results are displayed in Fig. 3.13 (a) and (b). The comparison to the experimental results shows a very good agreement between the theory and experiment. The parameters used in simulation are listed in Table 3.3.

Table 3.3: The self-heating hot spot model parameters

Name Description	Return Current I_r (μA)	Ambient Temperature $T_b(K)$	Heat Transfer Coefficient $\alpha(W/m^2 \cdot K)$	Resistivity at 20K $\rho_{20K}(\Omega \cdot m)$
DUT ♯1	5.66	4.2	2×10^4	2.05×10^{-6}
DUT ♯2	3.96	4.5	2×10^4	2.14×10^{-6}

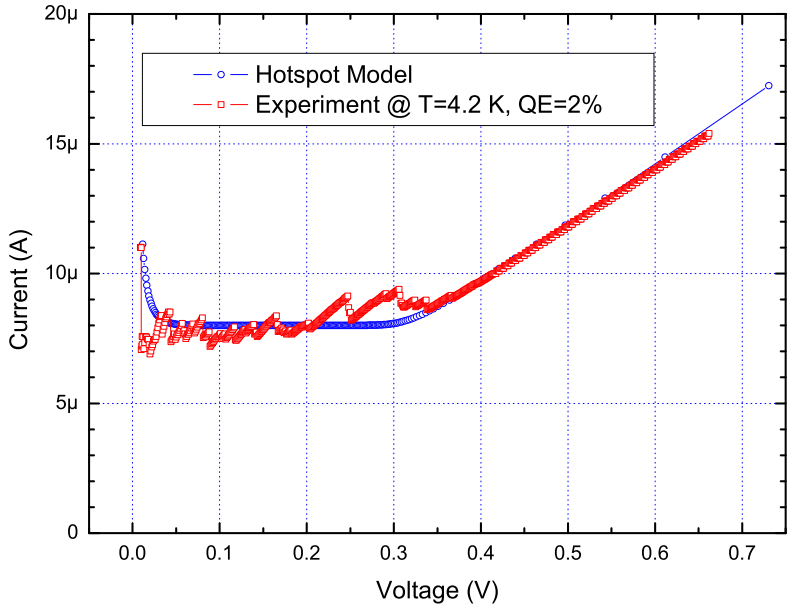

(a) Hotspot formation under voltage bias, for DUT I

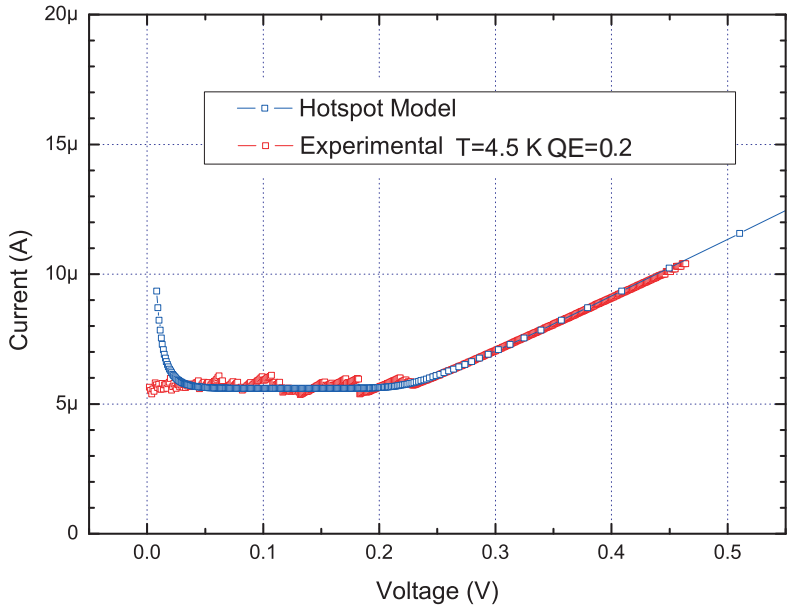

(b) Hotspot formation under voltage bias, for DUT II

Figure 3.13: Experimental and simulation results of the dc voltage and current characterization.

In this model, one of the free parameters is ρ_{20K}, which can be extracted via the dc resistance measured during the sample cooling down. The notation of 20K can be understood as the maximum resistivity before the transition temperature

T_c, which usually has the maximum value close to 20 K. The other free parameter, i.e. the return current I_r is determined from the I-V curve scan during the dc characterization measurement. It is the minimum current platform, almost constant current during the bias current. It may reveal the regularity along the segment of nanowire, because essentially this is based on one-dimensional ideal wire whose width is a constant of 120 nm, which can not be maintained to be true during the fabrication, i.e. the lithography. Our estimation based on this model shows that the thermal resistance is 0.048 Kcm^2/W at 4.2 K, which is a very good estimation based on self-heating model hot spots in [75]. Note the range of χ_0 in Eqs. (3.7) and (3.8) is $a_0 < \chi_0 < l \sim 10\mu m$, in which a_0 is determined by Eq. 3.6 and assumed to be completely normal in this regime.

3.6 DC and Small Signal RF/Microwave Measurement Under CW Power

In order to gain insights into the optical interaction with superconducting nanowires, we start with the continuous wave (CW) optical irradiation to study how the optical powers mediate superconducting Cooper pair density. In this section, we are going to show the results of DC and small signal S-parameter measurement in the presence of CW laser irradiation; and attempt to model the change of Cooper pair density by μ^* model [106].

3.6.1 DC Measurement

Under CW optical irradiation, we undertake the measurements of (a) the transition resistance during superconducting to normal state transition; (b) DC I-V measurement in the superconducting state to the switched state.

The transition resistance variation is measured while lowering the thermal bath temperatures. Fig. 3.14 records this transition with and without the presence

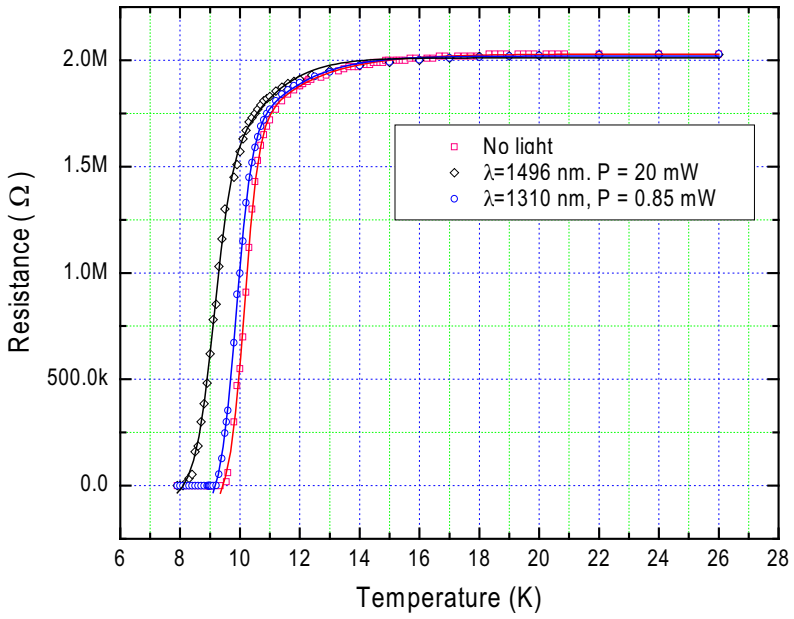

Figure 3.14: Normal to superconductivity transition presented by a resistance and temperature relation when the nanowire is shined with 1310 nm of power 0.85 mW, and 1496 nm of power 20 mW as well as in the absence of optical power (Dark).

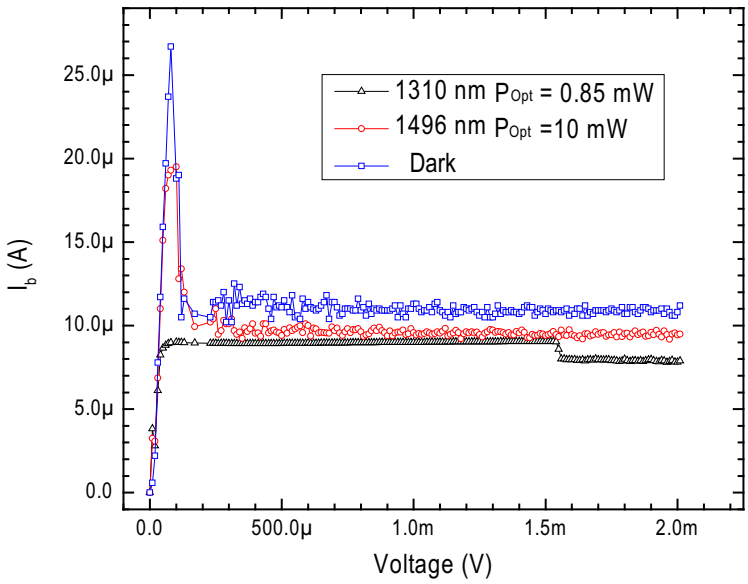

Figure 3.15: DC current and voltage scan at 4.2 K temperature when the nanowire is shined with 1310 nm of power 0.85 mW, and 1496 nm of power 10 mW as well as in the absence of optical power (Dark).

of CW optical irradiation. Three slopes and transition temperature have been identified in the above figure. It can be concluded that both optical wavelengths and power levels can play roles in the determining the transition properties of NbN superconducting nanowires. From numerical electromagnetic simulation, such as high frequency structure simulator (HFSS), the power absorption ratio at 1310nm and 1496nm wavelengths, one can see that not only the optical absorption, but also the optical coupling to the active area of DUT are responsible for the T_C difference displayed in Fig. 3.14. The CW of 1310 nm, 0.85 mW causes 0.2 K; and CW of 1496 nm, 20 mW causes 1.4 K reduction of T_C, respectively.

Fig. 3.15 depicts the current-voltage (dc I-V) scan when the DUT is in the voltage bias mode. All of the scans are obtained via National Instrument (NI) LabView. The maximum current in a computerized scan mode is less likely to accurately measure I_c. Nonetheless, from our statistics, the maximum error can be less than 1 μA, which is enough to demonstrate the Cooper pair density varied by optical irradiations. The maximum current peak is diminished under 1310 nm, 0.85 mW CW irradiation; while with 10 mW, 1496 nm CW power, a reduced I_c peak is observed. The diminishing I_c suggests that the size of optical induced resistive barrier (refer to Eq. 3.6) is large enough to cause spontaneous oscillations once $I_b > I_{ret}$ is satisfied; but smaller than the self-healing length [75] to cause device latching.

3.6.2 Small Signal RF/Microwave Measurement and μ^* Model

The optoelectronic measurement is performed in conjunction with S-parameter measurement. The coherent light source, i.e. a laser diode whose wavelength is 1310 nm is utilized (refer to Fig. 5.3). The optical interactions with the superconducting nanowires results in the depletion of Cooper pairs. The changing of the chemical potential μ by the optical irradiations dominates at lower temperature, e.g. at temperatures close to zero K, where we consider non-bolometric quantum behavior. The pertinent physics has been discussed by Liu *et al.* [107]. We ex-

perimentally confirmed the similar physics in NbN nanowires. On the other hand, when the temperature is very close to the critical temperature T_c, the bolometric behavior becomes pronounced. We can attribute and calculate the temperature variation by considering the optical power only transfers to lattice. Evidentally, T_c reduction agrees with the bolometric predictions in [108].

To study the optical interaction with the superconducting material, Owen *et al.* [109] first proposed a theoretical framework that incorporated the relation between the excessive quasiparticles to the variation of chemical potential μ. Later, as it is discussed in [106], the parameters pertaining to optical and thin films find a quantitative association with μ

$$\begin{aligned}
\mu &= \Delta_0(T) + \frac{k_B T}{2} \ln\left[\frac{2\Delta_0(T)}{\pi k_B T}\left(x_0^2 + \frac{h\nu\Gamma_\mu}{2\Delta_0(T)}\right)\right] \\
x_0 &= \sqrt{\frac{\pi k_B T}{2\Delta_0(T)}} \exp\left[-\frac{\Delta_0(T)}{k_B T}\right] \\
\Gamma_\mu &= \frac{2e^2}{(h\nu)^2} P_a \tau_\Delta \frac{\lambda_o}{d} Z_d D
\end{aligned} \tag{3.9}$$

in which P_a is the absorbed optical power; Δ_0 is the BCS energy gap at zero temperature in the absence of optical power; λ_o is the optical penetration depth; and Z_d is the intrinsic impedance of the free space. For definitions of the rest parameters, readers can refer to [106]. Based on this result, we introduce a nonequilibrium gap parameter ratio $\zeta(T)$ to be a function of T

$$\zeta(T) = 1 + \sqrt{\frac{2\pi k_B T}{\Delta_0(T)}} \exp\left[-\frac{\Delta_0(T)}{k_B T}\right]\left\{1 - \exp\left[\frac{\mu}{k_B T}\right]\right\} \tag{3.10}$$

where $\zeta(T) = \frac{\Delta_\mu(T)}{\Delta_0(T)}$. The relation allows us to relate the nonequilibrium Cooper pair density at a given temperature $n_\mu(T)$

$$\frac{n_\mu(T)}{n_{s0}} = \zeta(T)\frac{\Delta_0(T)}{\Delta_0(0)} \tanh\left(\frac{\zeta(T)\Delta_0(T)}{2k_B T}\right) \tag{3.11}$$

The chemical potential approach demonstrated a very good agreement with the work done in [109] when the sample temperature is relatively low. Fig. 3.16 depicts

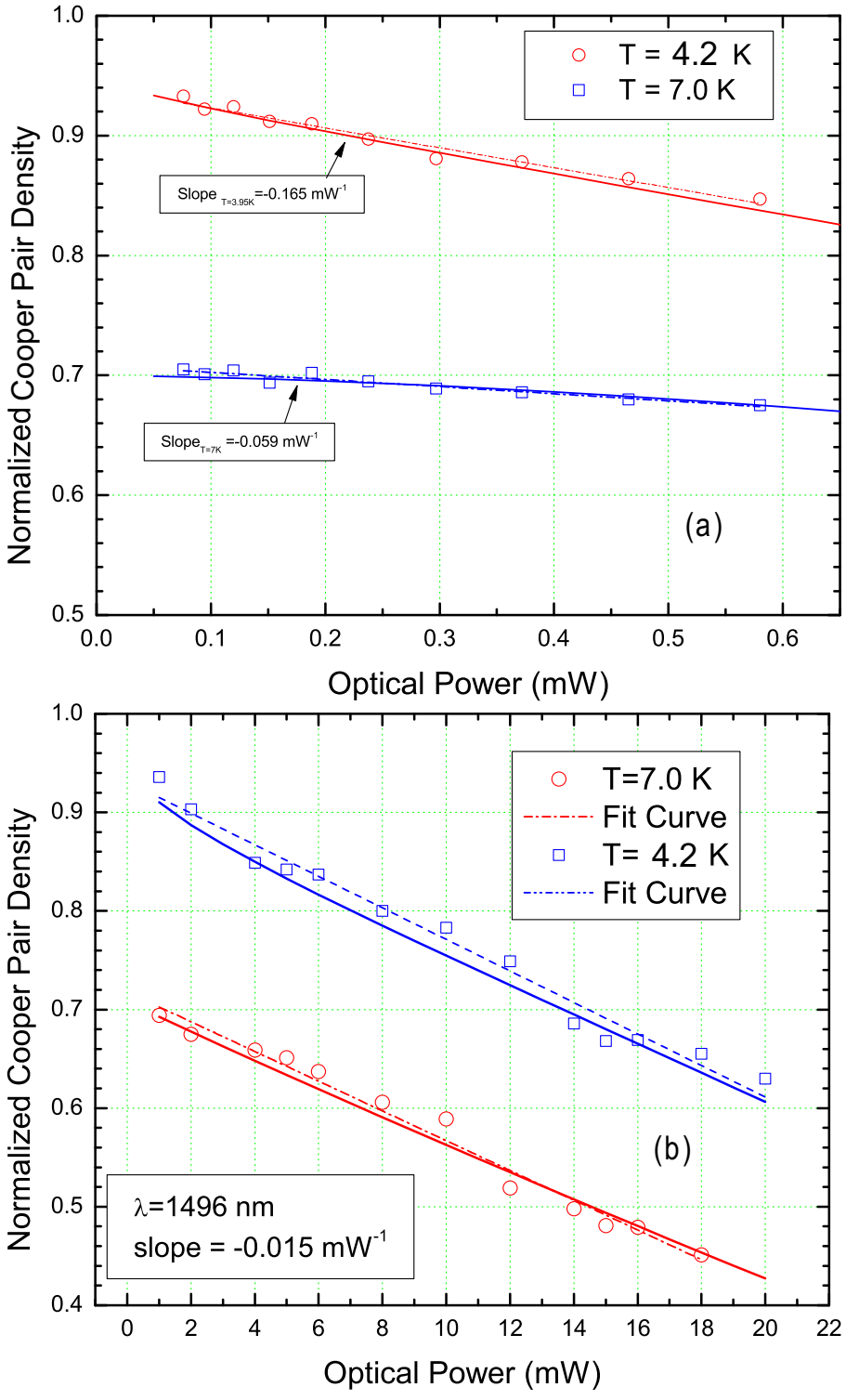

Figure 3.16: μ^* Model simulation and experimental result comparison under optical power scanning; solid lines are simulations; dash-dot lines are fitting curves; the plot (a) is for 1310 nm; and the plot, (b) is for 1496 nw cw, in both plots, blue open squares, red open circles are measurement results for 4.2 K and 7 K, respectively.

normalized Cooper pair density denoted as N_s under two optical wavelengths and power levels. In Fig. 3.16 (a) at two temperatures, we can identify two decreasing slopes of N_s. At T=4.2 K, N_s is more sensitive to the optical power variation than that at T=7 K. This implies that we expect more significantly pronounced optoelectronic effect at lower temperatures. The simulation is performed using Eqs. 3.9 to 3.11, and plotted in solid lines in the figure. The parameter of T at 7 K has to be corrected with a reduced effective T to be 6.5 K; and λ_o is used as the main fitting parameter in this simulation. At 4.2 K, λ_o varies from 1000 nm to 2300 nm, when optical power is from 0.05 mW to 0.85 mW; while at 7 K, λ_o varies from 350 nm to 1200 nm, for the same range of optical power as that of 4.2 K.

In contrast, for 1496 nm wavelength, the curves in Fig. 3.16 (b) for both temperatures exhibit almost identical slopes, implying that it is less likely to observe stronger optoelectronic effect with this wavelength. The simulation is performed with the same equations. When $T = 7$ K, we have to use the reduced effective T to be 6.55 K; and λ_o is again used as the main fitting parameter in the simulation. At 4.2 K, λ_o varies from 200 nm to 480 nm, when optical power is from 1 mW to 20 mW; while at 7 K, λ_o varies from 350 nm to 630 nm, for the same range of optical power as that of 4.2 K. However, in both wavelengths, Fig. 3.16 indicates that N_s is always higher when the temperature is lower.

At temperatures very close to T_c, the reduction of T_c calculated solely by μ overestimates what we have observed in the experiments. We believe that when the temperature is close to T_c, the optical field exchanges the energies it carries to the lattice of superconducting materials, rather than interacting with Cooper pairs, most probably due to the fact that BCS energy gap is strongly quenched and the availability of paired electrons is reduced considerably. Thus at temperatures close to T_c, the optical field interacting with lattice lends itself to heating up the superconducting surface up to its optical penetration depth, instead of destroying the electron pairing mechanisms. The optically induced thermal process has been

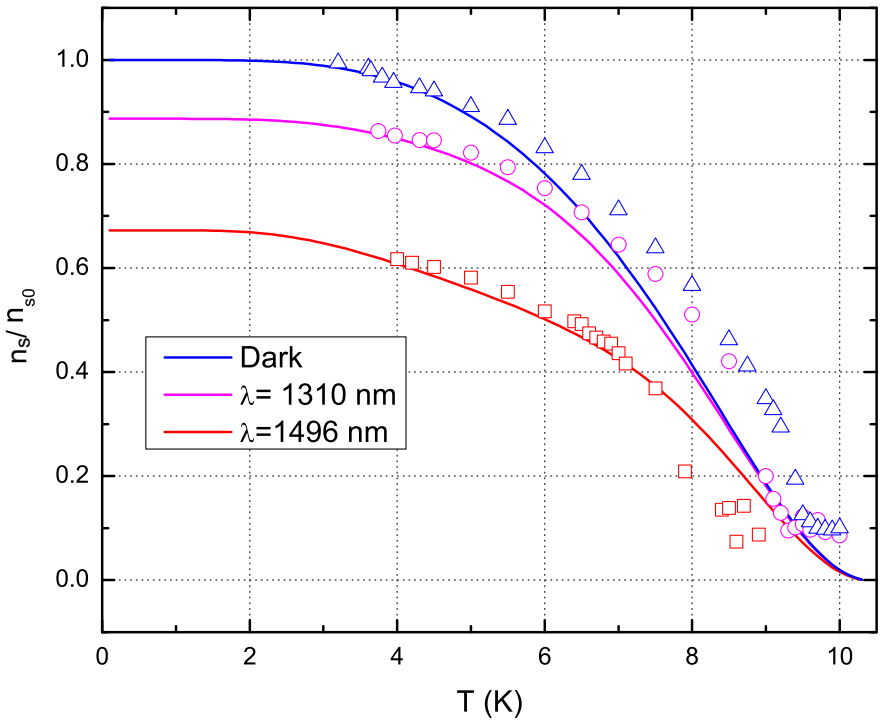

Figure 3.17: μ^* Model simulation and experimental result comparison in the absence of the effective transition temperature corrections; solid lines are simulations; blue open triangles, pink open circles and red open squares are measurement results for dark, 0.85 mw 1310nm cw, and 20 mW 1496 nw cw, respectively.

well studied in [108]. We model the reduced critical temperature T_c'

$$T_c' = T_c - \delta T = T_c - \frac{P_a \tau_{es}}{C_{ph} V} \tag{3.12}$$

where P_a is the absorbed optical power; τ_{es} is the phonon escape time, C_{ph} is the phonon specific heat; and $V = wdl$ is the volume of the nanowire. By separating two distinctively physical processes, we are able to model the Cooper pair density in the presence of external perturbation, such as continuous laser irradiation. The reduced Cooper pair density in the nonequilibrium state is expressed as:

$$n_s'(T) = n_{s0}' \left[1 - \left(\frac{T}{T_c'} \right)^4 \right] \tag{3.13}$$

where the dimensionless nonequilibrium Cooper pair density $n_{s0}' = \frac{n_\mu(0)}{n_{s0}} = \frac{n_\mu(T)}{n_{s0}}\Big|_{T \to \varepsilon \ll T_c}$.

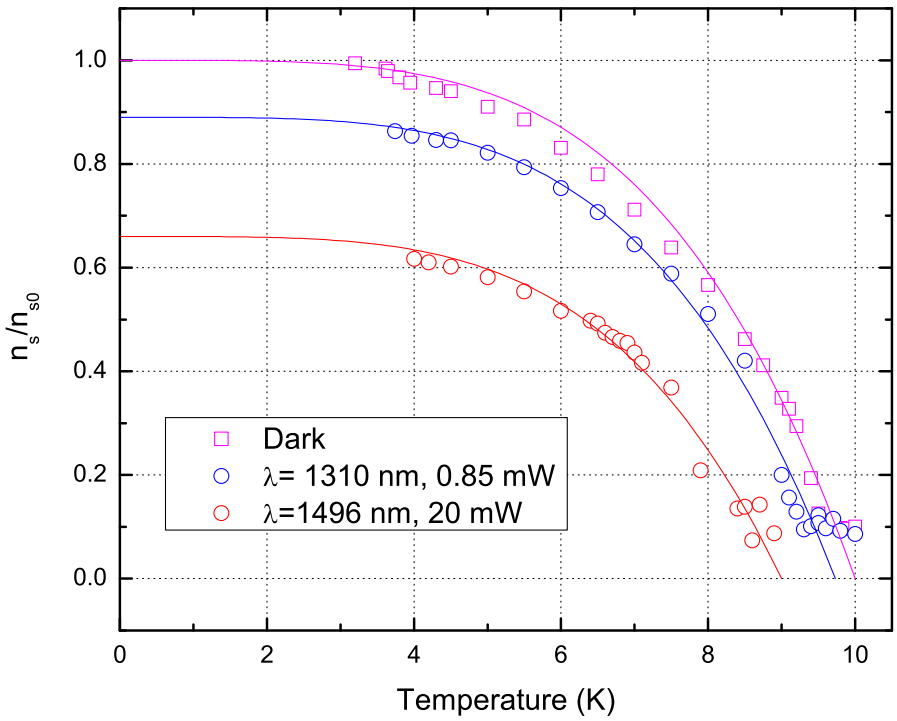

Figure 3.18: The Cooper pair density as function of temperature in the presence and absence of optical irradiation whose wavelength is 1310 nm, and power is 0.85 mW, and 1494 nm with power of 20 mW; solid lines are simulation results (blue color are the measured and simulated results in dark).

Fig.3.17 shows the simulation results without the attempt to correct the transition temperature reduction at the higher temperatures close to original T_c. The comparison with the experimental results indicates that $\mu*$ seems only valid when the thermal bath temperature is below $0.5T_c$. The simulation result is plotted in Fig. 3.18 as solid lines to compare with the experimental measurement. The comparison demonstrates a good match between the results. The relation in Eq. (3.13) is useful to model the interactions between a modulated optical irradiation and the superconducting nanowire, by which one can qualitatively calculate the ac optoelectronic responses for the microwave-photo mixing.

3.7 Summary

In this chapter, we first present the methods and results achieved from small signal RF/microwave measurement on the NbN nanowires. The equivalent circuit model is obtained via the two-step S-parameter measurement. The values of the circuit elements are determined in two consecutive steps. The first step aims to acquire the value of the lumped reactive element due to geometrical factors; the second step is to obtain the parametric relationship between the kinetic inductance L_k and dc bias current/voltage.

We have justified the existence of R_s by checking the damped resonance frequency points under different dc voltage bias values (R_s increases when dc bias voltages increases). The theoretical calculation compares well to the experimental measurements when the R_s is large in the circuit model (see Fig. 3.1 (b)).

The Ginsburg-Landau theory is employed to account for the L_k variation as the function of dc bias current ratio β. The analytical relation of L_k to β is obtained from G-L theorem (refer to Appendix A). The weaklink effect is revealed to explain limitation of I_c from reaching the bulk I_c^{GL}. We also anticipate the device quality can be determined by the parametrical variation of the kinetic inductance, which we think it becomes a figure of merit for a given SNSPD in terms of its quantum

efficiency.

Then we apply the small signal RF/microwave measurement method to investigate the thin film property. The measured results agrees with the expected value reported in the literature. This further confirms our method is a very effective tool to explore the change of Cooper pair density in the nanowires.

The I-V measurements showed four distinctive regime of a nanowire: i.e. superconducting, switched-relaxation, hotspot growth and hot wire regime, although the last regime is still under investigation, because not sufficient simulation has been carried on.

Lastly we showed the optical interaction with superconducting nanowire, their transition temperature T_c to identify two major mechanisms that can change the density of Cooper pairs, i.e. quantum regime, in which the chemical potential can be modeled as a function of absorbed optical power; and bolometric regime, where pure optical power heating up of a superconducting sample that results in the reduction of cortical temperature. We will show a good theoretical agreement with the experimental results in this perspective.

Chapter 4

Large Signal RF/Microwave Measurements

In the previous chapter, we have characterized the NbN SNSPD when it is excited either by DC and small signal RF signal or optical radiation. In this chapter, we will study the experimental results, when a large signal RF/microwave power is supplied to the SNSPD in the absence of optical irradiations. The goal is to gain the insight of the nonlinearity stemming from the superconducting nanowires by full power span of electrically sinusoidal ac signal. The ac signal is comprised of one or two single frequency components, namely one tone or tone signals. The Cooper pair density in the nanowire is very sensitive to such electrical perturbation. As a result, the kinetic inductance will be varying accordingly to react to such external excitations. The electrical signal based on the kinetic inductance, such as the RF power reflection coefficient, will be changed. This strong nonlinear effect is deemed as a parametric process.

The parametric processes have been widely employed to make exceptionally low noise microwave amplifiers [110]-[112], and filters [113]. The main physical component in such devices is a nonlinear reactive component. For example, the junction capacitance of a semiconductor varactor diode can be parametrically changed by varying the reverse junction voltage. The SNSPD exhibits strong nonlinearity.

Their Cooper pair density can be readily modulated by dc bias current [63, 65, 59] or optical radiation [108] or even ambient temperature. We have already quantitatively studied such properties in the preceding chapter. So we can take advantage of these properties to detect a great variety of weak signals, such as heat and optical signals [87], [114]-[115].

To exploit nonlinear properties of superconducting materials, one can form a resonator, and measure Q-factor variations under different levels of input microwave power [81]. However, their freedom in frequency domain has been limited by the center frequency of the resonator. We use NbN nanowires, primarily used for single photon detection, as a nonlinear reactive element. The NbN nanowire is placed at the one end of transmission line (TL), acting as its load. The equivalent circuit model has been constructed and the values of its components are experimentally determined.

Due to the nonlinearity of kinetic inductance, the time domain reflection coefficient can be used [116]-[117] to analyze harmonics of input frequency. The ac current can bias SNSPD higher than dc critical current. Therefore, we are able to manifest more exotic properties that can not be explored in the dc bias scheme.

In this chapter, we will explore two samples of biased-SNSPD at two different temperatures. The methods of time domain and frequency domain analysis are both employed. The former is based on the simplified equivalent circuit which is comprised of a nonlinear kinetic inductance as the load of TL. To find the general solution, the linear subnetwork has to be included in the calculation. This can be relatively easy to be achieved by the harmonic balance method. Nonetheless, the primary task of this chapter is to investigate the parametric relation of the nonlinear L_k under the different levels of dc and RF excitations. The methods widely used in the microwave circuit analysis are mainly for studying the device physics. The numerical simulation results may further provide us insights into the quasiparticle generation and recombination process, when the electrical power is supplied across the superconducting nanowire.

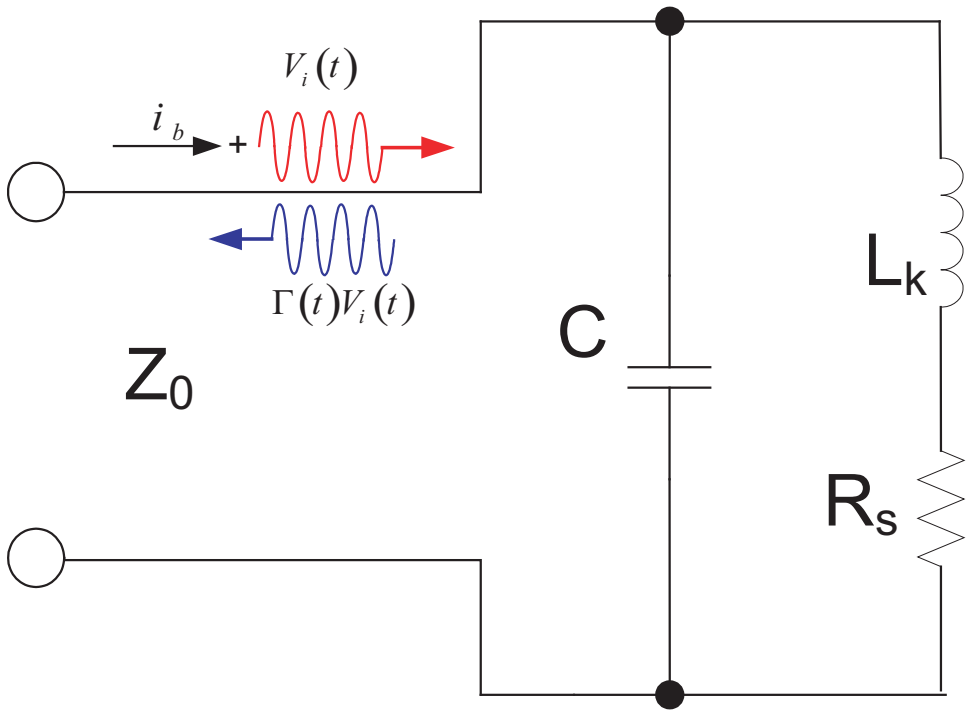

Figure 4.1: Equivalent circuit model as the complex load of transmission line.

4.1 Circuit Model As The Load of Transmission Line

The packaged SNSPD, as we have reported in chapter two, is connected at one end to a 50 Ω TL as its load. Based on the discussion in Appendix C, the transmission line effect can be ignored if we mainly focus on the amplitude information of discretely monochromatic harmonics.

The nonlinear load can be described by a circuit comprised of a nonlinear kinetic inductor. Fig. 4.1 shows the equivalent circuit model. The input RF signal (denoted as $g_1(t)$ in the Appendix C, but not shown in the figure) fed at the other end of the TL, propagating along the TL to the load. We treat the ac signal at the point of the nonlinear load to be $V_i(t)$. The nonlinear load is excited by combinations

of dc and ac signals, resulting in the reflected voltage $V_i(t)\Gamma(t)$ coupling backward into the same TL. Using the standard transmission line theory and KCL & KVL, the load voltage and current are expressed like

$$\begin{aligned} V(t) &= \frac{d}{dt}\left[\left(i(t) - C\frac{dV(t)}{dt} + i_b\right)L_k\right] + \left[i(t) - C\frac{dV(t)}{dt}\right]R_s \\ V(t) &= V_i(t)\left[1 + \Gamma(t)\right] \\ i(t) &= \frac{V_i(t)}{Z_0}\left(1 - \Gamma(t)\right) \end{aligned} \tag{4.1}$$

where as shown in Fig. 4.1, C is the parallel capacitance, R_s is the series resistance, which might be induced by Joule heating, when the bias current is very close to its critical value; $Z_0 = 50\Omega$ is characteristic impedance of TL and is dc bias current. Then combine the voltage and current relations, we will obtain a nonlinear second order differential equation that contains a time varying reflection coefficient $\Gamma(t)$. The relation between reflection coefficient $\Gamma(t)$ and the input microwave signal can be expressed via the following differential equation in time domain

$$\begin{aligned} & L_k(t)\,C\frac{d^2}{dt^2}\left[\left(1+\Gamma(t)\right)V_i(t)\right] + \left[1+\Gamma(t)\right]V_i(t) \\ & -L_k(t)\,\frac{d}{dt}\left[\frac{V_i(t)}{Z_0}\left(1-\Gamma(t)\right)\right] \\ & -\left\{i_b + \frac{V_i(t)}{Z_0}\left(1-\Gamma(t)\right) - C\frac{d}{dt}\left[\left(1+\Gamma(t)\right)V_i(t)\right]\right\}\frac{d}{dt}L_k(t) \\ & -\left\{\frac{V_i(t)}{Z_0}\left(1-\Gamma(t)\right) - C\frac{d}{dt}\left[\left(1+\Gamma(t)\right)V_i(t)\right]\right\}R_s = 0 \end{aligned} \tag{4.2}$$

Note that the kinetic inductance $L_k(t)$ now becomes a function of time through the current bias ratio $\beta(t)$ as

$$\beta(t) = \frac{i_b}{I_c^{GL}} + \frac{V_i(t)}{Z_0 I_c^{GL}}\left(1-\Gamma(t)\right) - \frac{C}{I_c^{GL}}\frac{d}{dt}\left[\left(1+\Gamma(t)\right)V_i(t)\right] \tag{4.3}$$

where I_c^{GL} is the Ginsburg-Landau critical current, whose value can be readily extrapolated by the zero voltage maximum current of a given SNSPD I_c , which is constriction limited by about 50% to 60% to that of I_c^{GL}. The Ginsburg-Landau relation of L_k has been developed in the preceding chapter and its analytical solution taken from Eq. 3.5

$$L_k(\beta) = \frac{L_{k0}}{1 - 4\cos^2\left(\frac{\pi}{3} - \frac{1}{3}\arctan\left(\frac{\sqrt{1-\beta^2}}{\beta}\right)\right)} \tag{4.4}$$

Table 4.1: Nonlinear Kinetic Inductance Expansion Coefficients

Conditions	L'_{k2}	L'_{k4}	L'_{k6}	L'_{k8}
DC	0.444	0.329	0.273	0.238

in which L_{k0} is the zero bias kinetic inductance. We can expand it into power series as

$$L_k^{'}(\beta) = 1 + \sum_{n=1}^{\infty} L_{k2n}^{'} \beta^{2n} = 1 + L_{k2}^{'}\beta^2 + L_{k4}^{'}\beta^4 + L_{k6}^{'}\beta^6 + L_{k8}^{'}\beta^8 + ... \tag{4.5}$$

where normalized $L_k^{'} = L_k/L_{k0}$; and up to the 4^{th} order of coefficients $L_{k2n}^{'}$s have been listed in the Table 4.1.

Setting the dc bias ratio to zero makes the power of even harmonic components to be absent. No explicit relation can be found to relate $L_{k2n}^{'}$s to each harmonic component of the reflected signals. Thus, we propose an approximation method to relate the reflected harmonics $V_o^{L_k}(t)$ to the nonlinear L_k, by assuming that the contribution to each harmonic component only arises from the lowest order nonlinear term. The relation up to the forth order read

$$V_o^{L_k}(t) \cong \sum_{n=0}^{4} V_a \beta_a^{2n+1} L_{k2n}^{'} \cos(2n+1)\omega t \tag{4.6}$$

where $V_a = \omega L_{k0} I_c^{GL}$; and β_a is the scaled bias ratio of incident current to the bulk critical current I_c^{GL} of SNSPDs. It can be approximated as $|V_{in}|/2Z_0 I_C$. The harmonic power components are proportional to the square of each term coefficient.

In practice, voltages derived from the reflected power can not be identical to $V_o^{L_k}(t)$ in Eq. (4.6), because $\Gamma(t)$ is not only the function of amplitude, its frequency of incident signals, but also susceptible to two types of perturbations: (a) the capacitive load in parallel when the excitation frequency is high enough; (b) the resistive contribution in series with the kinetic inductance, when the power from ac signal will unavoidably introduce heat to those nanowires in SNSPDs, leading to either phase slip resistance or hotspot resistance [90]. Both factors can lead to solving Eq. 4.2 rather complicated.

Given the complexity above, it seems to achieve an analytical solution to Eq. 4.2 becomes unlikely. However, we consider some physical factors that guide us to simplify the situation: (1) the measurement frequencies are in the range of 10^8 Hz, so $1/\omega C$ is much larger than ωL_k. (2) The dc bias is only by 1 μA and is less than the return current of the nanowire. More importantly, the thermal bath temperature is at 4.2 K, far below T_c. it is unlikely to induce resistance R_s. Thus, to neglect terms containing either C or R_s in Eq. (4.2) does not seem to lose too much accuracy to its numerical solution. The simplified equation is

$$L_k \frac{d}{dt}\left[\frac{V_i}{Z_0}(1-\Gamma)\right] + \left[i_b - \frac{V_i}{Z_0}(1-\Gamma)\right]\frac{d}{dt}L_k - (1+\Gamma)V_i = 0 \tag{4.7}$$

and $\beta(t)$ becomes

$$\beta(t) = \beta_d + \frac{V_i}{Z_0 I_c}(1-\Gamma)$$

where β_d is the ratio of the transient dc bias to that of the bulk critical current, i.e. $\beta_d = i_b / I_c^{GL}$.

The agreement obtained via comparing results of simulations to experimental measurements justifies this assumption (see the comparisons demonstrated in Fig. 4.4, and Fig. 4.5).

4.2 One Tone Measurement

4.2.1 Experimental setup

Two types of setup has been used to test the one tone and two tone responses by exciting the nanowire. The first attempt was in a customized Janis side-loading cryostat equipped with four microwave probe arms. Each arm has the frequency range up to 40 GHz Pico-Probe coplanar probe tip with a K-connector. The base temperature can be as low as 1.8 K, achieved by constantly pumping liquid helium in the 1 K pot. The flow of pumping rate is controlled by a needle valve. Since pure electrical signals are involved, no optical coupling is required in such type of test. So we do not have to rely on the complicated optical coupling.

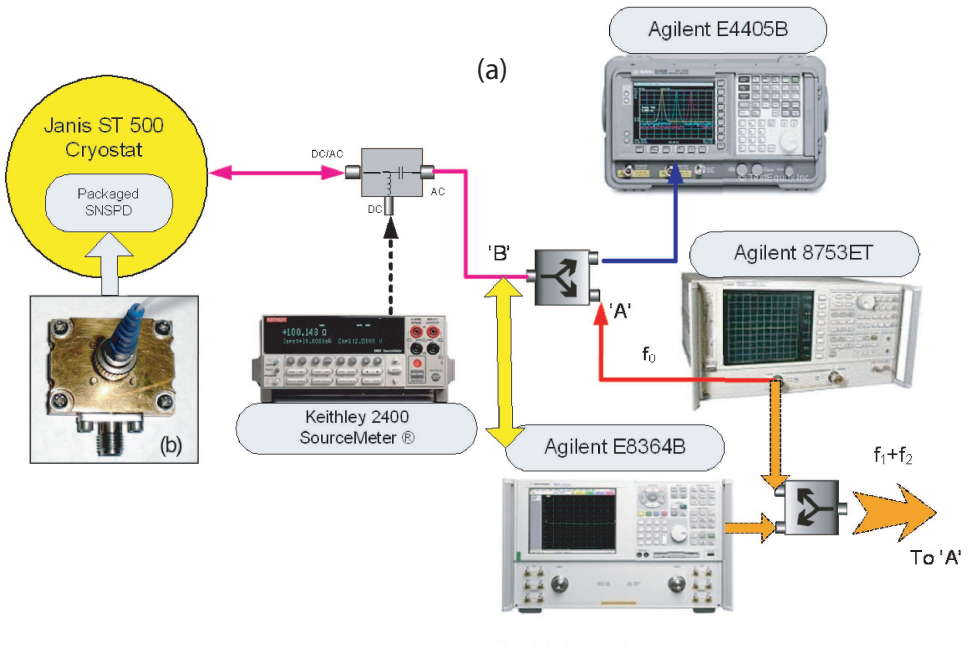

Figure 4.2: (a) The experimental setup and connections for the nonlinearity measurement; (b) the picture of the SNSPD microwave package.

Some preliminary experiments have been undertaken with the preceding setup, but its operational complexity has restricted us from sticking with it. Subsequently, we have developed the second setup, which is illustrated in Fig. 4.2. For the latter setup, the packaged SNSPD has been loaded into a much portable Janis ST-500 cryostat. We use Keithley 2400 SourceMeter as the dc bias source because it can be operated either in voltage or current source mode. Agilent 8753ET in our setup acts as a microwave power source, whose frequency ranges from 3 KHz to 3 GHz, and its output power ranges from -20 dBm to 5 dBm. Even lower excitation power can be achieved by cascading attenuators (IL =-15 dB from 10 MHz to 5 GHz from our characterization). The microwave power divider has more than 20 dB isolation below 2 GHz, which is the key to make it equivalent to a microwave circulator in the frequency range of our measurements.

Three types of measurements, including one port S-parameter, one tone and two tone measurements are needed in order to reveal the parametric properties of SNSPD nanowires. The setup shown in figure 4.2 is primarily for two tone

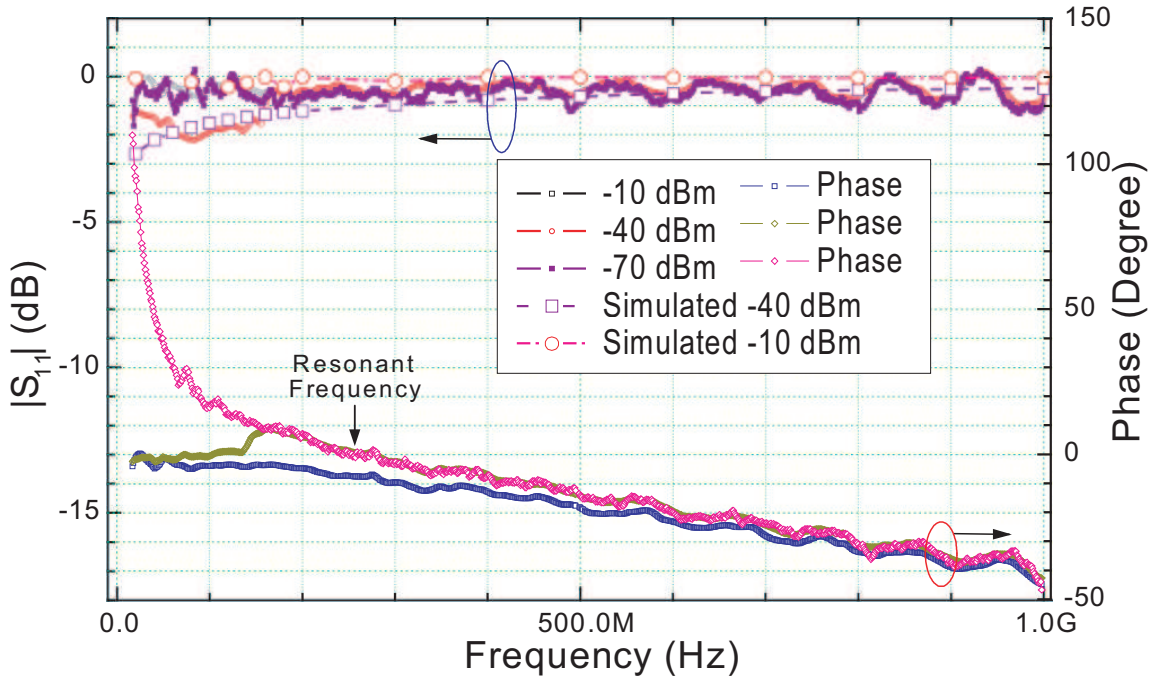

Figure 4.3: One port S-parameter measurement under different microwave power levels, the dc bias was set to be zero in all cases. The simulated results for reflection are marked in dashed lines for power levels of -10 dBm (open circle) and -40 dBm (open square).

measurement. We employ Agilent E8364B PNA, whose frequency ranges from 10 MHz to 50 GHz, to perform S-parameter measurement. The relevant connection is done by connecting the bias tee ac port to the PNA input port one. We choose the reference plane at the packaging input port when performing PNA calibration. As for two tone measurement, we just add one more power divider/combiner of the same model to the input arm of the power divider/combiner shown in Fig. 4.2. It combines two sinusoidal signals with frequency difference $\Delta f = 30$ MHz in all of the tests. In the later experiment, E8364 PNA has been programmed in Continuous Wave mode (CW) to act as the second microwave signal source.

4.2.2 Measurement Results

The S-parameter experiment has to be made at room temperature and cryogenic temperature. The former test aims at evaluating other forms of reactive element on top of the kinetic inductance. Such reactive elements are primarily due to the geometrical structures, e.g. interconnections of the microwave packaging; or parasitic capacitances arising from adjacent nanowires. The measurement shows a capacitive load close to 1.4 pF in parallel and a series inductance less than 1 nH. The equivalent circuitry thus has been constructed and shown in Fig. 4.1.

The results of cryogenic temperature measurement are illustrated in Fig. 4.3. The one port S-parameters have been measured under three levels of microwave power. The ac current amplitude is primarily determined by the microwave power. Three regimes have been identified, i.e. inductive, mixed and capacitive loads.

- First, when the excitation power is very high, e.g. -10 dBm, the input peak current is about $143I_C$, the superconductivity of SNSPD nanowires has been destroyed. Very large hotspot may be present due to the Joule heating by the excitation power. Consequently, only the capacitive component is dominant.

- Second, when the excitation power is not too high, i.e. the corresponding current amplitude is comparable with the critical current, e.g. -40 dBm, which is about $4.5I_C$, relatively stronger absorption to the excitation power is appreciable when the frequency is lower than about 180 MHz.

- Third, when the current is about 14% of I_C, i.e. at -70 dBm power level, we can see that the inductive load becomes dominant. Notably, both intermediate and low powers have one resonant frequency at about 278 MHz, as indicated by the arrow in Fig. 4.3. After the resonant frequency point, S-parameter (S_{11}), including its phase and amplitude, gradually merges into the same values. This also implies that Eq. (4.6) is only valid when excitation power is close to -70 dBm. Higher the power applied, higher degree of approximations has to be taken into account, in order to exploit Eq. (4.6).

In spite of this fact, experimental results always show that the nonlinear effect can be measurable only if the ac current amplitude is very close to the critical current I_C. As shown in Fig. 4.3, our numerical simulation reveals that strong reflection of input power always occurs, leading to poor absorption of ac input current.

More interestingly, as the frequency of ac signal approaches 1 GHz, almost complete reflection happens regardless of how high the RF power level is (e.g. -40 dBm or -10 dBm), even without the presence of series resistance and parallel capacitance. This is primarily due to the mismatch between the nonlinear load to the 50 Ω transmission line.

Typical results of one tone measurement are shown in Fig. 4.4 and 4.5 for 20 MHz and 100 MHz fundamental frequencies, respectively. Fig. 4.4 is under zero dc bias current; and Fig. 4.5 is obtained when I_b=1 μA (14 % dc bias ratio). Meanwhile, we have conducted numerical simulation on one tone measurement with $I_b = 0$ or 1 μA, based on the theoretical methods reported in Section 4.1.

The simulation results have been plotted in both sets of figures as comparison to that of experimental measurements. Table 4.1 tabulates the nonlinear terms illustrated in Eq. (4.5). DC nonlinear coefficients are obtained by Taylor expansion of Eq. (4.4). The ac terms are evaluated via Eq. (4.6), where kinetic inductance at zero bias (L_{k0}) is 230 nH (one port S-parameter measurement); and critical current I_c is measured to be 14 μA. Note that the power levels in each harmonic have to take into account of path losses. So we calculate the coefficients after compensating the insertion losses of cryogenic cable, power divider and bias tee. Each of them has been characterized separately and cascaded via transfer matrix method. The careful calculation shows that this insertion loss ranges from 5 dB to 10 dB, when the testing frequency varies by 1 GHz above 10 MHz; and such insertion loss is frequency dependent. The extracted nonlinear coefficients in the table suggest that with the higher frequency, nonlinear effects of SNSPD nanowires become weaker. So we are unable to extract when f_0 =100 MHz due to extremely low power strength of the eighth harmonic. Another aspect of Eq. (4.6) predicts that if the dc bias

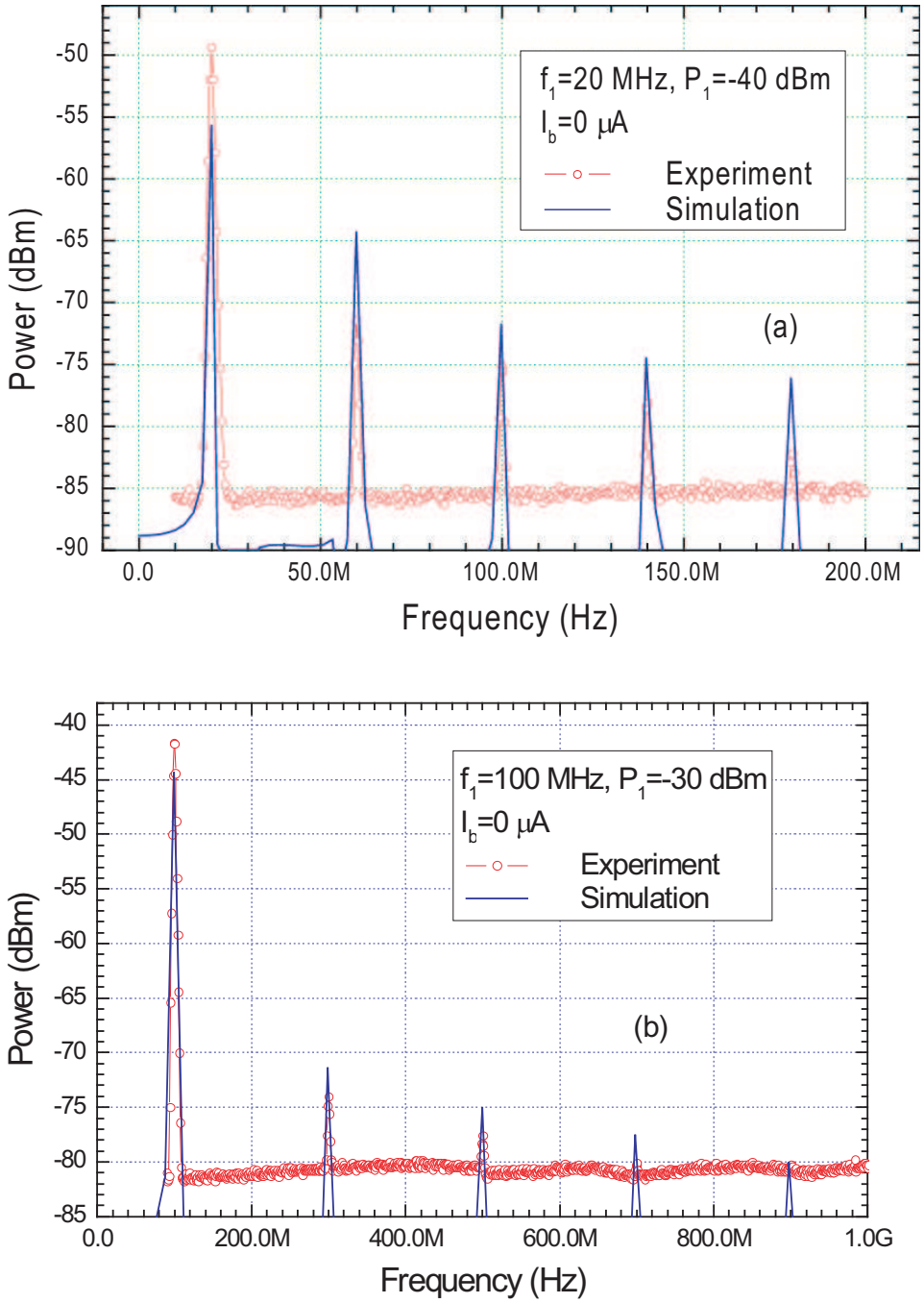

Figure 4.4: One tone simulation and measurement under different levels of microwave power with zero dc bias current, (a) the fundamental frequency is 20 MHz, power is -40 dBm; (b) the fundamental frequency is 100 MHz, power is -30 dBm.

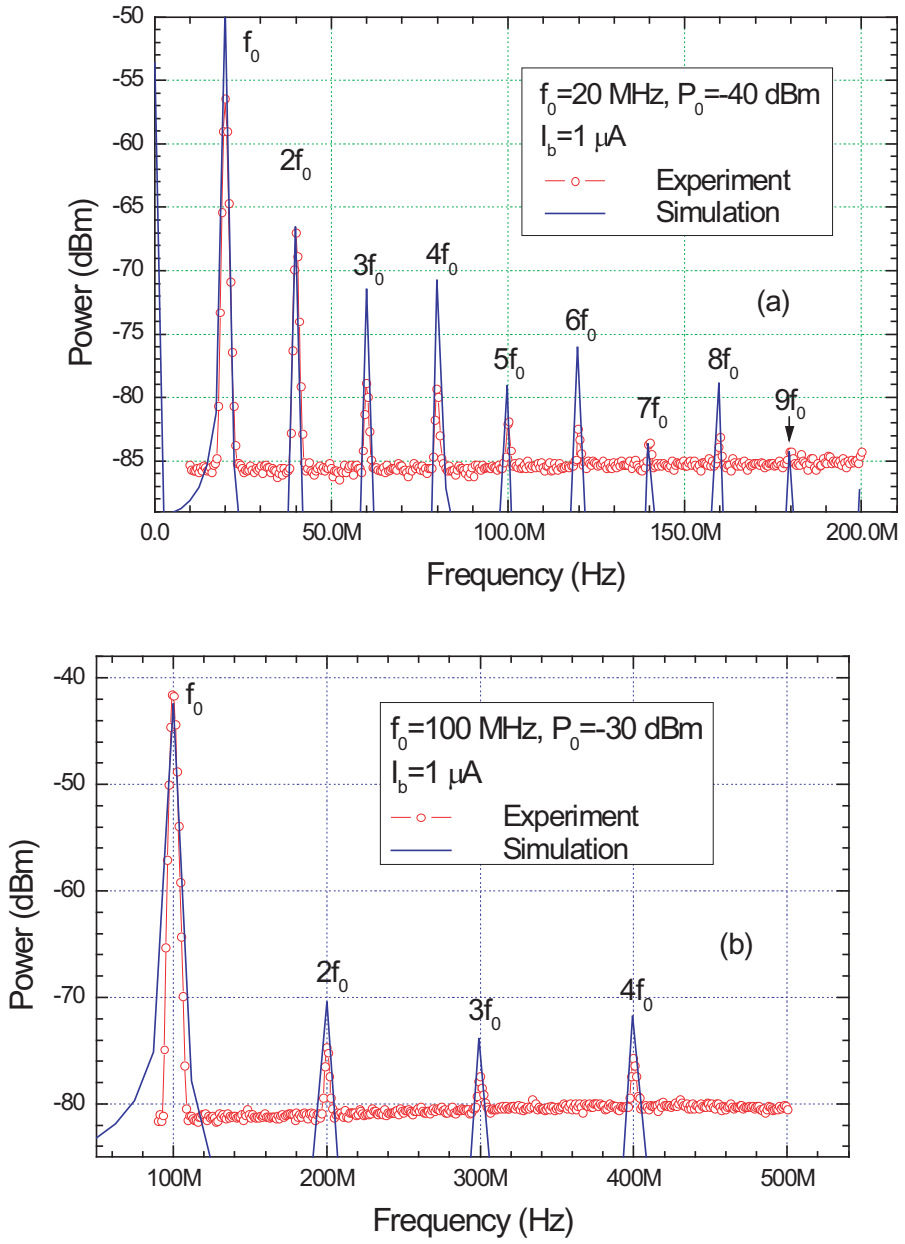

Figure 4.5: One tone simulation and measurement under different levels of microwave power with 1 μA dc bias current, (a) the fundamental frequency is 20 MHz, power is -40 dBm; (b) the fundamental frequency is 100 MHz, power is -30 dBm.

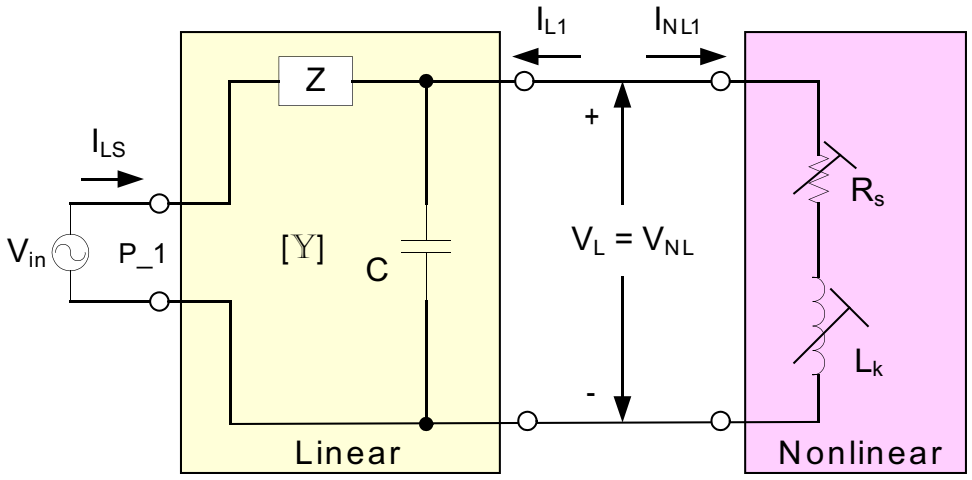

Figure 4.6: The circuit partition scheme of harmonic balance method into linear and nonlinear block diagram and their interconnection node voltage and current.

current is nonzero, power components of even number harmonics should be present in the reflected spectrum. More importantly the even number harmonic power should be higher than that of next odd number harmonics.

4.3 Harmonic Balance Analysis

The previous section is tackling the nonlinear circuit as the TL load in the time domain. The simplified nonlinear equation is solved. However, the equivalent capacitance C and the series resistance R_s have not been taken into account. Given the fact that the driving frequency is periodic, it is possible to analyze the entire circuit by a hybrid method, where both frequency-domain and time-domain analysis are involved [118]-[123]. This approach is so called Harmonic Balance (HB) method. The HB method is useful to analyze nonlinear microwave circuits. It can quantitatively simulate higher order harmonics, intermodulation distortions (IMD), and steady-state responses. Due to these desirable features, many computer-aided design softwares of microwave circuits are equipped with this method, such as HP-ADS.

4.3.1 The Harmonic Balance Analysis Scheme

The HB analysis assumes that there exists a well defined large signal nonlinear relationship for each nonlinear component; the new frequencies stemming from the nonlinearity must be included in simulation result; the dc bias condition must be taken into account. Nevertheless, the existence of stably unique HB solution is not guaranteed. The nonlinear inductance is very rarely used in the microwave circuits. So we have to specifically develop our own formulas and procedures to implement the HB method.

The first step is to partition the entire circuit into linear and nonlinear parts. Fig. 4.6 illustrate the circuit partitioning for the equivalent circuit as the load of TL (see Fig. 4.1). The linear part is represented by a N-port linear network; the nonlinear part will be represented by a predefined time domain relationship of their I-V model. The latter is usually obtained by nonlinear characterization. In our case, only one nonlinear port is involved, but it is comprised of two strongly nonlinear components coupled by the total bias current, we model them by the relation

$$V_{NL}(t) = \frac{d}{dt}\left[L_k(t)\, i_{NL}(t)\right] + i_{NL}(t)\, R_S \tag{4.8}$$

L_k (refer to Eq. (4.5)) is the function of time-varying bias ratio i_{NL}/I_c^{GL}. From the preceding discussion, $I_c^{GL} > I_c$ and the ratio between them at 4.2 K ranges from 40% to 60% depending on the NbN film quality. Next, the linear part of the equivalent circuitry is a two port network and is described by Y-matrix

$$[\mathbf{Y}] = \begin{bmatrix} Y_{SS} & Y_{SL} \\ Y_{LS} & Y_{LL} \end{bmatrix} = \begin{bmatrix} \frac{1}{Z_0} & -\frac{1}{Z_0} \\ -\frac{1}{Z_0} & \frac{Z_0+Z_C}{Z_0 Z_C} \end{bmatrix} \tag{4.9}$$

where $Z_C(\omega) = \frac{1}{j\omega C}$ is a function of harmonic frequency, $Z_0 = 50\Omega$ is TL characteristic impedance. Port 1 is connected to the source excitation as well as acting as the load for the reflected power at higher harmonics. Port 2 is connecting to the nonlinear port. The current balance relation is

$$\mathbf{I}_L + \mathbf{I}_{NL} = \mathbf{I}_S + \mathbf{I}_{L1} + \mathbf{I}_{NL} = \mathbf{Y}_{LS}\mathbf{V}_S + \mathbf{Y}_{LL}\mathbf{V}_L + \mathbf{I}_{NL} = \mathbf{0} \tag{4.10}$$

in which all the current vectors are the harmonic components. Both $\mathbf{Y}_{LS}$ and $\mathbf{Y}_{LL}$ are diagonal sparse matrix. For the one tone excitation whose frequency is ω_1 and amplitude is V_{si}. Suppose up to kth order harmonic is our interest, then we have

$$\mathbf{Y}_{LS}\mathbf{V}_S = \begin{bmatrix} i_{b0} & 0 & 0 & ... & 0 \\ 0 & -1/Z_0 & 0 & ... & 0 \\ 0 & 0 & -1/Z_0 & ... & 0 \\ ... & ... & ... & ... & 0 \\ 0 & ... & ... & 0 & -1/Z_0 \end{bmatrix} \begin{bmatrix} 1 \\ V_{si} \\ 0 \\ ... \\ 0 \end{bmatrix}$$

$$\mathbf{Y}_{LL}\mathbf{V}_L = \begin{bmatrix} 0 & 0 & ... & ... \\ 0 & j\omega C + 1/Z_0 & 0 & ... \\ ... & ... & ... & ... \\ 0 & ... & ... & jk\omega C + 1/Z_0 \end{bmatrix} \begin{bmatrix} 0 \\ V_{L1} \\ ... \\ V_{Lk} \end{bmatrix}$$

$$\mathbf{I}_{NL} = \begin{bmatrix} -i_{b0} \\ \tilde{I}^1_{NL} \\ \tilde{I}^2_{NL} \\ ... \\ \tilde{I}^k_{NL} \end{bmatrix}$$

The dc bias appears in the first component of column vector $\mathbf{I}_{NL}$ is $-i_{b0}$ since we assume the dc bias always balance with the source vector $\mathbf{Y}_{LS}\mathbf{V}_S$. Note this assumption may be not hold when a two tone HB simulation is carried out. The rest components in $\mathbf{I}_{NL}$ is the Fourier transform at the N-th harmonic

$$\tilde{I}^N_{NL} = \frac{1}{T}\int_0^T i_{NL}(t)\exp(jN\omega_1 t)\,dt \tag{4.11}$$

in which $1 \le N \le k$, and $\omega_1 = 2\pi/T$ is the fundamental angular frequency whose period is T (in the following chapter, it represents the electrical pumping frequency). The simulation algorithm is based on relaxation method. This method has an iterative loop in which the current is the independent variable. Its value is repeatedly updated at each cycle by the relation

$$\mathbf{I}_{NL} = (1-p)\mathbf{I}_{NL} - p\mathbf{I}_L \tag{4.12}$$

where p is the convergence parameter. In most cases, we choose its value to be at 0.0001 to 0.001. The determination of p value is basically from experience. Usually it takes less than three times of iteration to achieve the best solution; however, the most important step is indeed the initial guess of $\mathbf{I}_{NL}$, and the value of R_s. The strong nonlinear relation given by Eq. 4.4 leads to very difficult convergence of the solution for high number of iterations. R_s is induced by quasi-particles in the superconducting condensate. To decide the value of R_s is not easy. From the measured R_s in previous chapter, we approximate it

$$R_s = R_{s0}\left[\beta_d + \sqrt{\sum_{i=1}^{k}\beta_i^2}\right] \tag{4.13}$$

where R_{s0} is the maximum resistance under a given temperature and a given input power range; β_d is dc bias ratio; β_i is the relative current amplitude of the $i-th$ harmonic to that of bulk critical current.

4.3.2 The Results of HB Analysis

The detailed depiction of our HB analysis platform is uniquely dealing with a strong nonlinear inductance in conjunction with the quasi-particle induced resistance. We have performed a series of simulations and compared the results to the relevant experimental measurements. Fig. 4.7 shows two simulation results at the sample temperature of 7.5 K. The input RF power level is scanned from -73 dBm to -48 dBm at dc bias of 2.5 μA; and -72 dBm to 63 dBm at dc bias of 5 μA. In both plots, the hollow circles, squares and triangles represent the experimental results and solid lines are simulation plots. The input 1 dB compression points are located at about -60 dBm and -69 dBm for 2.5 and 5 μA dc bias, respectively. The dynamic range of the second and the third harmonics range from 30 to 60 dB.

Fig. 4.8 displays the simulation result for temperature of 5 K, but the dc bias current is very close to zero voltage maximum current I_c. Only low RF current can be supplied to the device (about 2.5 μA). From the dynamic range ($<$ 10 dB) of

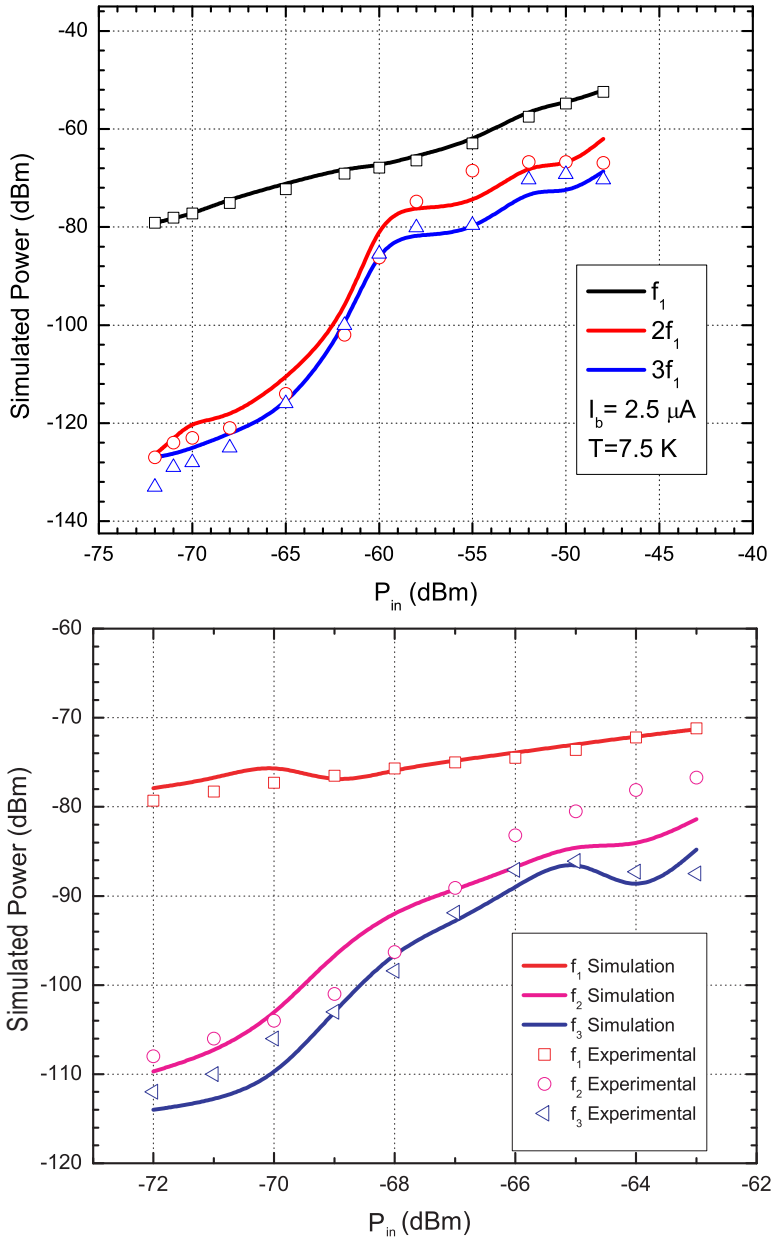

Figure 4.7: The comparison of the experimental results of the single tone of 12 MHz, and the simulation results based on harmonic balance method in solid lines, under the input power scanning, when the sample temperature is 7.5 K; the upper plot is under the dc bias of 2.5 μA and the lower plot is at 5.0 μA. The $I_c = 6.5\mu$A.

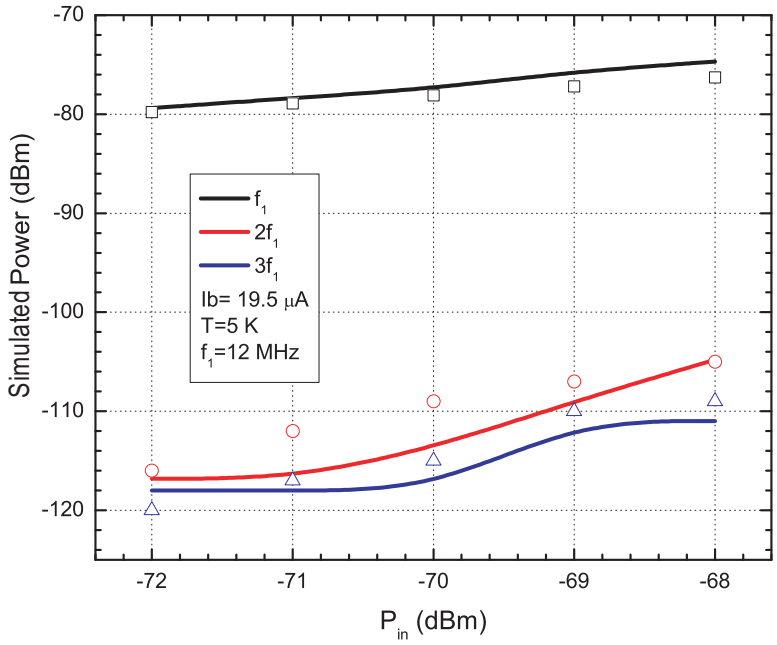

Figure 4.8: The comparison of the experimental results of the single tone of 12 MHz, and the simulation results based on harmonic balance method in solid lines, under the input power scanning, when the sample temperature is 5 K; under the dc bias of 19.5 μA. The $I_c = 20.5\mu$A.

the second and third harmonics before self-heating induced latching (refer to Fig. 3.6), we conclude that the nonlinearity at high bias ratio and lower temperature is actually much weaker than the cases demonstrated in Fig. 4.7. The linearity compression at the fundamental frequency is insignificant.

Tables 4.2 and 4.3 illustrate the simulation results obtained via two typical analysis methods, time domain and HB methods. The comparison to the experimental results under zero or nonzero dc bias suggest that HB method can be more accurate for highly nonlinear circuit, because it can readily take more components into account without causing complicated mathematic tasks. In both analyzes, their maximum differences to the corresponding experimental results are in the ranges of $\pm$ 5 dB, We suspect that it may arise from our nonlinear model. The model has at least one value uncertainty, i.e. R_s, which is not explicitly acting as a fixed value resistor, nor its physical process has been completely known. Nonetheless, we

Table 4.2: The Comparison of simulation results from time domain and HB analysis methods and experimental results for $f_1 = 20$ MHz, and $I_b = 0\mu$A, and $P_{in} = -40$ dBm.

	Time-Domain (dBm)	HB Method (dBm)	Measurement (dBm)
P_{f_1}	-56	-49	-49
P_{2f_1}	$<$ -85	-119	$<$ -85
P_{3f_1}	-64	-72.5	-71
P_{4f_1}	$<$ -85	-112	$<$ -85

Table 4.3: The Comparison of simulation results from time domain and HB analysis methods and experimental results for $f_1 = 20$ MHz, and $I_b = 1\mu$A, and $P_{in} = -40$ dBm.

	Time-Domain (dBm)	HB Method (dBm)	Measurement (dBm)
P_{f_1}	-50	-50	-56
P_{2f_1}	-67	-69	-67
P_{3f_1}	-72	-77	-79
P_{4f_1}	-71	-78	-79

are primarily seeking the nonlinear behavior under the strong electrical excitations. Both nonlinear circuit analysis, time domain and HB method, are complimentarily powerful tools to understand the experimental results.

4.4 Measurements of Two Tone Excitation

Two tone or multi-tone measurements are very efficient technique for testing intermodulation distortions (IMD) in communication systems, especially their microwave power amplifiers (PA) to drive the base station antenna. These tests are performed by applying two equal power, but closed spaced frequency (usually less

than 1% of their center frequency) RF/microwave power onto the DUT. The side bands are the odd number harmonics. The relative amplitude to that of the fundamental frequency components are the best evaluation to the (IMD) under different input power levels. Nonetheless, the nonlinearity in this category of devices is definitely undesirable.

On the other hand, strong nonlinearity is the key requirement for detectors and mixers. Testing two frequency mixing effect will be useful for predicting detection/conversion efficiencies in detector/mixer components. To this end, the frequency spacing can be larger to meet the intermediate frequency (IF) requirements. We have tested the two tone mixing effect stemming from the nonlinear kinetic inductance of SNSPD nanowires. Two sinusoidal wave were combined by a Pasternack power combiner, and fed into the packaged device at 4.2 K. Two basic observations: First, the number of intermodulation harmonics seems to correlate with the resonance frequency f_r as indicated in Fig. 4.3. When the input frequency is lower than f_r, the load of TL is inductive. Therefore Eq. (5) is valid. Fig. 4.9 (a) shows measurement in this case. As the input frequency is higher than fr, the load of TL turns into capacitive. In this case, we are unable to observe any lower harmonics, except those located in the vicinity of two input frequencies. Second, the two tone mixing is frequency dependent. Higher the frequency is, weaker the mixing (compare Fig. 4.9(b) and Fig. 4.9 (c)) results. The harmonics of mixing signals diminishes when their center frequency is close to 900 MHz given the power shown Fig. 4.9 (d). We believe that the nonlinearity can persistently exist if the capacitive load is suppressed by carefully redesigning the nanowire structure. Moreover, such capacitance may also be a strong limiting factor against the ultimate SNSPD counting rate. In other words, the capacitance load not only obscures the nonlinearity of kinetic inductance in NbN SNSPDs, but also imposes extra delay by about few nanoseconds to the photoresponse of a SNSPD in time domain.

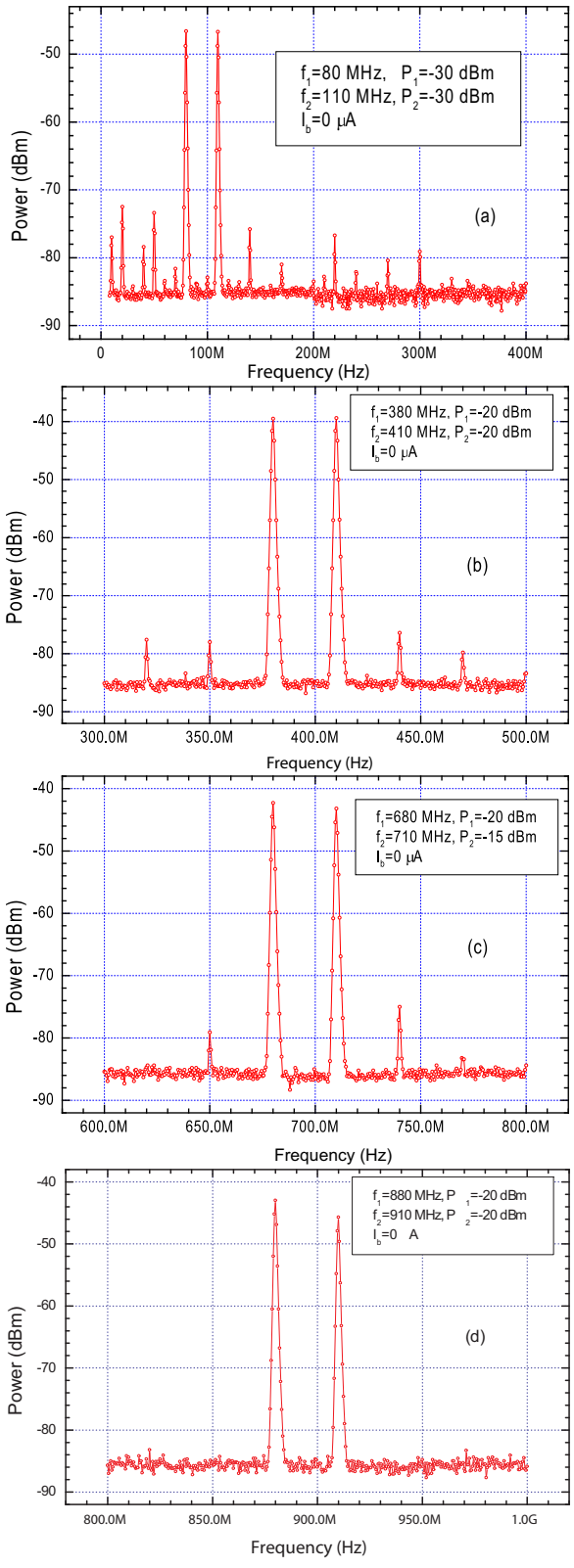

Figure 4.9: Two tone measurement with zero dc bias current in different frequency ranges (a) f_1=80 MHz and f_2=110 MHz; (b) f_1=380 MHz and f_2=410 MHz; (c) f_1=680 MHz and f_2=710 MHz; (d) f_1=880 MHz and f_2=910 MHz.

4.5 Summary

In the presence of large RF/microwave signals, the kinetic inductance L_k of SNSPD will be driven into strong nonlinear regime, where its parametric variations under different dc bias ratios are readily studied via measuring their higher order harmonics. First, the one port S-parameter measurement is performed at cryogenic temperatures, whose result shows the trend of nonlinear L_k under three different levels of RF/microwave excitation powers. Next, one-tone and two-tone measurements are undertaken separately. In the one-tone measurement with and without dc bias current, the measured harmonic amplitudes agree with what our mathematical model anticipates. For the two-tone measurements, our results indicate that a cut-off frequency of the nonlinearity at about 800 MHz. This is not only due to the capacitive reactance in parallel with the superconducting nanowire, but also due to other factors, including strong reflections, and quasiparticle conduction induced strong R_s fluctuations.

In order to gain quantitative insights into the nonlinearity, we have used two major methods, i.e. time domain and harmonic balance method to analyze the nonlinear microwave circuit, that models the SNSPD nanowires acting as the load of TL. The nonlinear L_k is described by the G-L relationship. Simulations via both time domain and HB methods have achieved satisfactory agreements with the measurements. The numerical results confirms that our modeling technique is able to account for the nonlinearities, even in the relatively strong regime. We anticipate that the aforementioned achievements allow us for seeking further optoelectronic mixing effects in the SNSPD nanowires by electrically pumping. The strong nonlinearity can be induced by RF power and DC bias current. The highest nonlinearity achievable is the point prior to the abrupt change of L_k as shown in Fig. 3.6. Notably, in a wider range of temperatures, it seems that one can always achieve the desirable nonlinearity point. The optoelectronic mixing measurement in the following chapter can manifest the role of temperature in achieving the single photon mixing effect.

Chapter 5

Quantum and Classical Optoelectronic Mixing in NbN Superconducting Nanowires

In the previous chapter, we have used time domain and harmonic balance method to analyze and simulate large RF signal excitations on the superconducting nanowire meander lines. In addition, based on the conclusion of chapter 3, we will develop optoelectronic mixings under classical intensity of the light. Furthermore, we anticipate to scale down the photon flux intensity into the single photon regime, to realize a single photon mixer based on the same structure that makes the SNSPD.

In the present chapter, we will start with some general introductions to the conception and importance of optoelectronic mixers; then we will briefly illustrate the types of widely used solid-state mixers. The quantum conversion matrix forms the theoretical background to account for the experimental results. Classical and quantum level mixings are reported in detail in the following sections.

The SNSPD has been studied extensively due to its high counting rate (> 100 MHz), low dark count rate (< 1 Hz), low jitter time (in picoseconds), and broad optical responsitivity ranging from 0.3 to 5 micron wavelengths [31, 51]. Recent efforts[56]-[57] to make SNSPDs have the photon number resolving capability, high

quantum efficiency, and high counting speed are of strong interest. However, the constriction, i.e. a certain type of non-uniformity along nanowires, has been found to prevent the SNSPD getting higher quantum efficiency [63]. The yield of SNSPD that is practically useful in a Quantum Key Distribution (QKD) system [68] is reduced accordingly. The main reason is that the gap between dc bias current to the maximum zero voltage current (I_c) is limited by the dc bias scheme, which is susceptible to latching [89] and exceptionally high dark count rates. The superconducting nanowire optoelectronic mixer offers ac bias as the electrical pump. Moreover, it is inherently sensitive to the single photons. To investigate this mixer may provide us a solution to the above problems.

The expected critical current versus that of the measured values, the comparison shows that the bulk value of the I_c should follow a $1-(T/T_c)^{3/2}$ trend, whereas the weaklink limited critical current is almost a linear function of temperature. Therefore, at higher temperatures, close to T_c, the discrepancy between the two I_cs are giving increased numbers. That suggests a suppressed kinetic inductance variation induced by the bias current. Therefore, the quantum efficiency of the detector must be limited. This explains the fact that in order to have better QE, one has to make the temperature of the thermal bath lower, however it is not too desirable to make it below certain temperature, e.g. 2 K, because the maximum current limited by the weaklinks is saturated, not much room is available to further improve the maximum current to compete with the bulk critical current. The dc bias current is apparently limited by the weaklinks during the sputtering of the ultra thin NbN films, 4 nm in the most SNSPDs nowadays.

To circumvent such problem, by applying an ac current, and taking advantage of the weaklink capacitance to bypass the dc barrier, we may be able to overcome the limitation, at least to some extent. To prove the idea, we start to measure the total current of the nanowire under the combination of dc and RF current bias. Fig. 5.1 shows the S-parameter measured in the power scan mode. We have tested the entire dc current bias range. The input power is at 11 MHz, and its power level

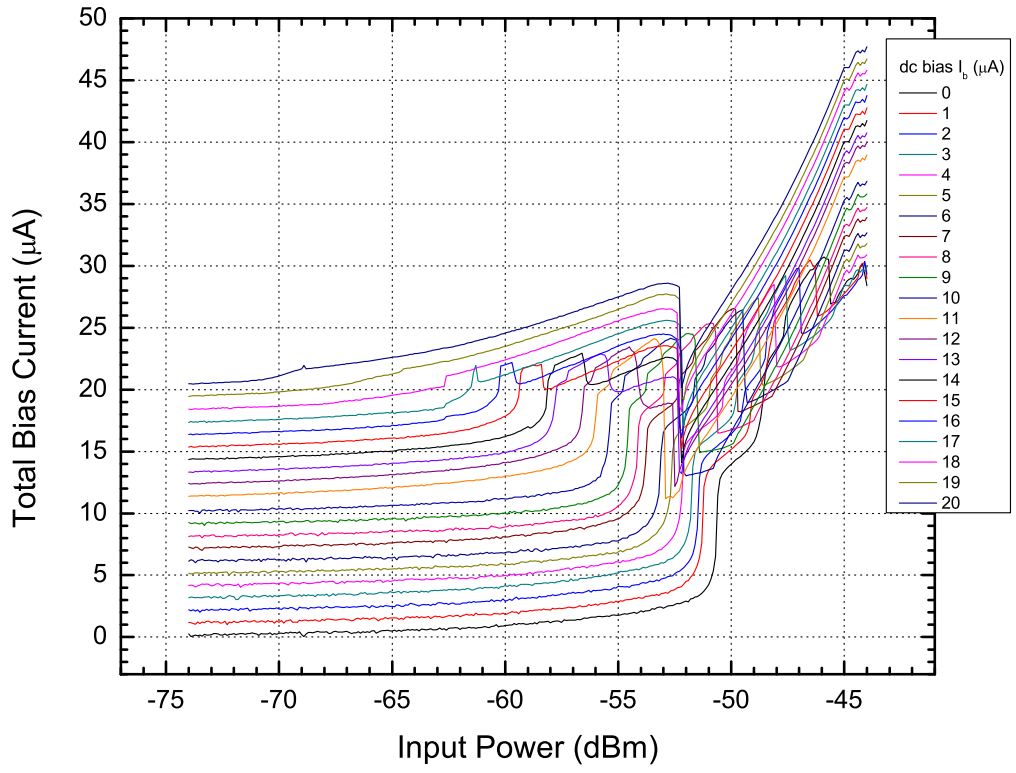

Figure 5.1: Total current measurement for 11 MHz RF power input under different levels of dc bias current.

ranges from -72 dBm to -42 dBm. The insertion loss of each power coupler has been deduced from the input power in the calculation. The above measurement suggests that the optoelectronic mixing effect is achievable under the combined dc and RF bias current.

One immediate advantage of such optoelectronic mixer is that for the SNSPD, the photon detection rate can break the limitation imposed by transient recovery time of the photoresponse (>10 ns). In comparison, to boost up the operating speed for APDs, the sinusoidally gated version has been introduced [124] in order to make it operate in the multi-hundreds of MHz clock, albeit a 40 ns dead time is still required to reduce the after pulse effect induced extra count. In this scheme, a sinusoidal signal whose frequency is usually in several hundreds to GHz is supplied to capacitively coupled to the anode of a reverse biased APD. After the a photon being absorbed and an avalanche event occurs, the output of the signal is passing a high-Q band-stop filter, by which the driving clock frequency is removed from the output frequency spectrum. The rest frequency components form the photon registration pulse, which has been amplified through a wide band low noise microwave amplifier. The APD used in this scheme has quantum efficiency of a few percent at 1550 nm wavelength. In fact, they are comparable with SNSPDs at the same wavelength. The QE of the APD is set to be this low is to avoid dark counts results from the afterpulse effect, because lower amplitude of the sinusoidal bias applied to the diode will less likely pump and inject hot-electrons into the deep defect states residing in the space charge area of the diode junction. To this end, the advantage of the higher clock rate has to pay the price of the reduced QE. Other problems include the relatively poor jitter time, due to the steepness of its dc I-V curve in comparison with superconducting SNSPDs; the required avalanche regardless how many photons contained in a given photon pulse. Therefore, we are not able to anticipate any photon number resolving capability in such detectors.

On the other hand, regarding SNSPDs, the formation of a hotspot along the nanowire occurs once a photon or a number of photons have been absorbed. The

voltage spike beyond a predefined threshold represents a registered photon click event. Although attempts have been made to correlate the amplitude of a given voltage spike, their amplitude depends on many factors, particularly the instantaneous bias level which is the consequence of all previous photon detection event, because the recovery from the previous photon response requires more than 10 nanosecond. The energy stored in the kinetic inductance needs to be released followed by a formation of another ready state to accept those newly incident photons. So we can see that the hotspot induced by the absorbed photons under proper dc bias conditions has both advantages and disadvantages, i.e. we need a hotspot to register one photon detection event; but the formation of the hotspot washes out the photon number contained in a given optical pulse. Suppose if we can detect the physical parameter in the superconducting nanowire without resort to the hotspot formation, we may be able to secure the photon number information carried by the coherent optical pulses.

In the following sections, we will first present an overview of different types of frequency mixers; then make an attempt to model the optoelectronic mixing by invoking the quantum detection exhibited in superconducting kinetic inductance [125]; in conjunction with conversion matrices method [126] to analytically derive the mixing product relations; followed by detailed descriptions of optoelectronic mixing measurements under two levels of optical intensity, i.e. in the classical and single photon regimes.

5.1 Overview of Different Types of Solid State Frequency Mixers

The solid state frequency mixer takes advantage of nonlinear effects of a certain device; such as semiconductor diodes, superconducting Josephson Junctions. It is compact and scalable. In general, three types of such mixers can be categorized and displayed in Fig. 5.2 based on their input and output formats. Here we define

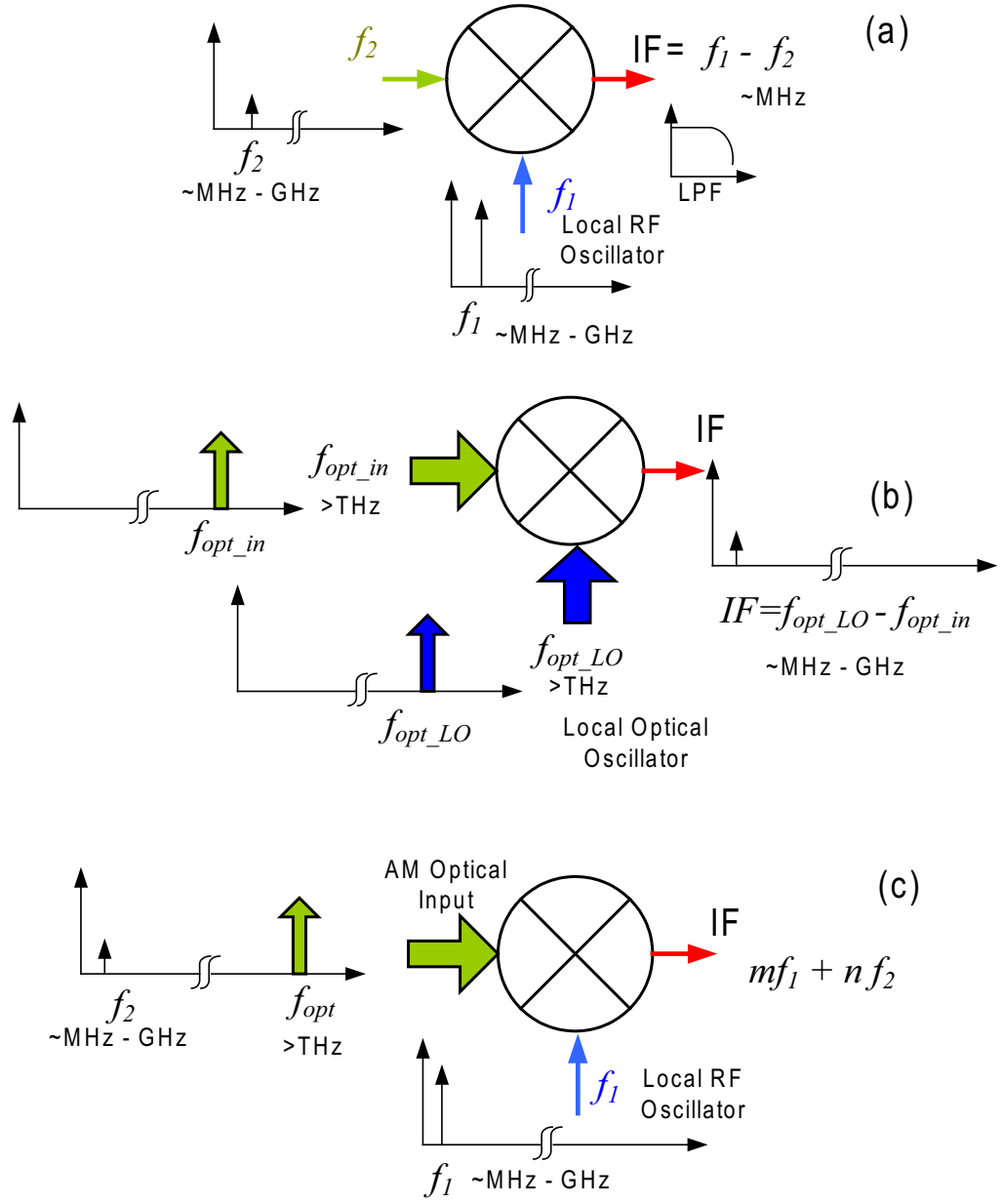

Figure 5.2: Diagrams for three types of mixers, (a) Electrical-electrical input with electrical output mixer, (b) Optical-optical with electrical output mixer; (c) Optical-electrical with electrical output mixer, where both m and n are integers.

the optical input, whose frequencies are usually above THz, as an electromagnetic wave irradiating on the mixer active area, such as a laser beam in free space and horn antenna radiations. The electrical input, whose frequencies are in the range below 100 GHz, can be guided in circuits, such as coplanar transmission lines.

The most common mixer is an RF mixer that converts a weak input IF signal down to a lower frequency (in most cases, a low pass filter (LPF) is adopted to filter out high frequency components). Fig. 5.2 (a) illustrates such type of mixer, which is characterized by all three ports are fed with pure electrical signals.

Another type of frequency mixer has two optical inputs at the signal and local oscillator (LO) ports. Their frequency difference ranges from a few GHz to some hundreds GHz. It is widely used in most optoelectronic applications as photomixers and heterodyne detectors. It is depicted in Fig. 5.2 (b). Hereafter we call it type II mixer. Both semiconductor and superconductor can be used to make the mixer. They have found applications in optical down conversion detection and mixing. Moreover, the superconductive mixers have been successfully studied, [106, 108, 127, 128] including both LTS and HTS based mixers. They were made in different structures [3, 129] and exhibited satisfied performances mostly in LTS, especially for NbN thin films. For instance, Superconductor-Insulator-Superconductor (SIS) mixers [130, 131] have demonstrated the best performance in the millimeter wave and submillimeter wave regions. Superconducting hot electron bolometric (HEB) mixers have the better noise equivalent power (NEP) over other heterodyne mixers above 1 THz [132]. The diffusion-cooled [133] and the phonon-cooled [134, 135] are two kinds of HEB mixers that have a cooling mechanism for hot electrons. The type II mixers is designed to match the transmission line. Their compact sizes allow them for high IF frequency output up to 100 GHz [132].

It is technically difficult to make the frequency difference of two optical frequencies below 1 GHz at telecommunication wavelength, e.g. at λ =1550 nm, the wavelength difference is only about 1/100 nm. So the type II mixer can not detect amplitude modulated (or intensity modulated) (AM) signals whose carrier f_{opt}

wavelength is in telecommunication regime. To tackle the difficulty, Fig. 5.2 (c) depicts an electrically pumped optoelectronic mixer. In the figure, the local oscillator port is excited by an RF signal f_1, where it mixes with the optical AM signal f_2. Alternatively, the mixer in Fig. 5.2 (c) can be made as an optically pumped optoelectronic mixer by swapping the local oscillator input to an AM optical signal. However, the latter will not be addressed in this work, because optically induced nonlinearity requires relatively high carrier power, especially in the superconductive mixer that is operated at the temperature far below T_c.

Although semiconductor optoelectronic mixers [136]-[142] have demonstrated a lot of attractive features, their noise level is still too high to be suitable for them to detect quantum signals, such as very weak optical power at the single photon level. On the other hand, the superconducting nanowire Device Under Test (DUT) in this work consists of a single photon detector and a optoelectronic mixer. This mixer/detector combo is sensitive to very weak optical signals. The square-law video detection takes place regardless in the absence or presence of dc bias, the former can serve as an implicit envelope detector, which is typified as no f_2 power above noise floor, due to the symmetry of the nonlinear inductance. The non-symmetrical nonlinear inductance can be readily realized by a non-zero dc bias. In the latter case, the explicit photo detection occurs, which is marked as a constant power level of f_2. In parallel, the optoelectronic mixer takes the detected optical envelope as f_2 to generate the intermodulation (IM) products with the LO f_1. These products are expressed in the form of $mf_1 + nf_2$, where integer numbers m and n can be either positive or negative or zero. Most the products are treated as IF signals in this work.

5.2 Experimental Techniques

Experimental setup for the testing platform is capable of measuring nonlinearity of any superconducting device, by exciting the device under test (DUT) with a

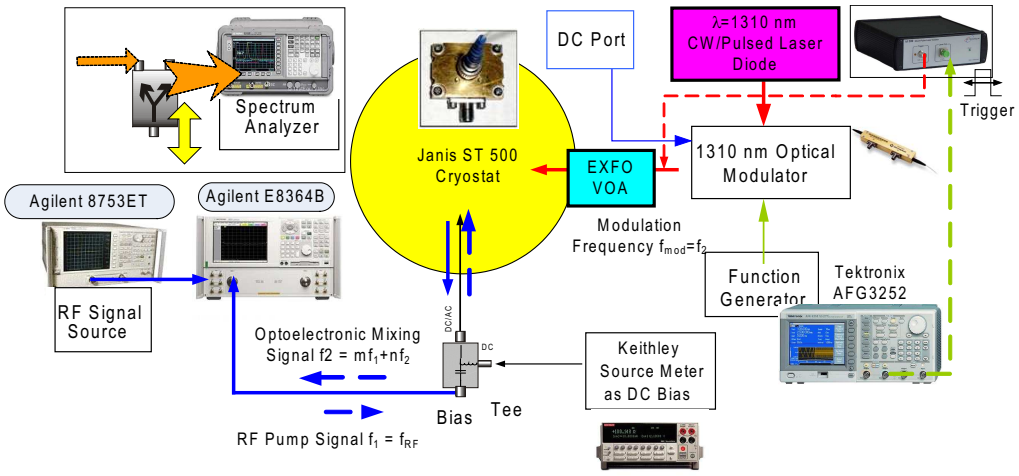

Figure 5.3: Experimental setup for the nonlinearity and optoelectronic mixing measurement.

monochromatically sinusoidal wave whose power level is time varying. The measured mixing products are therefore purely due to the excitation of the fundamental frequency, not by any spurious harmonic frequencies. The monochromatic excitation source is achieved by Agilent 8753ET. We operate it in the power scan mode at a given single frequency.

Fig. 5.3 depicts the experimental setup for this test. E8364B PNA is utilized as the key measurement equipment. We use its options of reconfigurable test set, to reconfigure the front test signal path, in order to take advantage of the flat noise floor and sensitivity of the PNA receivers. The PNA receiver has been source-calibrated to measure the absolute power level of each mixing product, which is undertaken in individual channels. In addition, the relatively higher insertion loss of PNA port coupler suppressing any unwanted harmonic from the excitation source. This becomes extremely important for measuring the mixing products with optical signals, when their intensity is below the single photon level. Alternatively, this testing setup can be used to characterize SNSPD by RF/microwave one/two-tone via a spectrum analyzer, e.g. Agilent E4405B (displayed in a dashed line box). Moreover, this setup not only measures the S-parameter at the fundamental frequency, but also at other frequencies, which is useful to gain insights into the nonlinearity

of SNSPD nanowires.

The optical signals can be prepared by either intensity modulated CW laser, or by triggering pulsed laser. A variable optical power attenuator (manufactured by EXFO) is employed to adjust average number of photons in each pulse, the repetition rate of the pulsed laser is determined by the triggering frequency produced from a function generator, in this work we employed Tektronix AFG3252.

5.3 Pulsed and Time Harmonic Waves Optical Sources

Time-harmonic optical irradiation, i.e. an intensity modulated coherence laser source, and pulsed optical irradiation, i.e. a pulsed coherent laser source are mathematically modeled as Sinusoidal and Gaussian waves in the time domain, respectively. Readers can refer to Refs. [108] and [106] for details. Fig. 5.4 illustrates both types of the optical irradiation, in which their power levels are tuned to contain the same amount of photon per pulse; and the power level of the time harmonic optical irradiation is normalized to be unity. Fig. 5.4(a) is the time domain power amplitude in one period. Each optical pulse is modeled by a Gaussian shape function; and each time harmonic is modeled by $1 + \sin \omega t$ like function. Fig. 5.4(b) is Fourier expansion of the repetitive temporal signal displayed in Fig. 5.4(a). The power spectrum of time-harmonic optical irradiation contains only one frequency component of the fundamental frequency. This is different from the pulsed optical irradiation, in which a series of power frequency components are in the presence. The pulsed optical irradiation is achieved by an id-Quantique id-301 DFB laser unit, which is designed for standard Quantum Key Distribution (QKD) systems. The unit is equipped with RF triggering port of 50 Ω. It accepts TTL standard triggering in the form of either square or sinusoidal wave. The full width at half maximum (FWHM) is 300 ps. The optical port is FC/PC connector. The standard output power has been pre-calibrated in the factory. The average optical power is

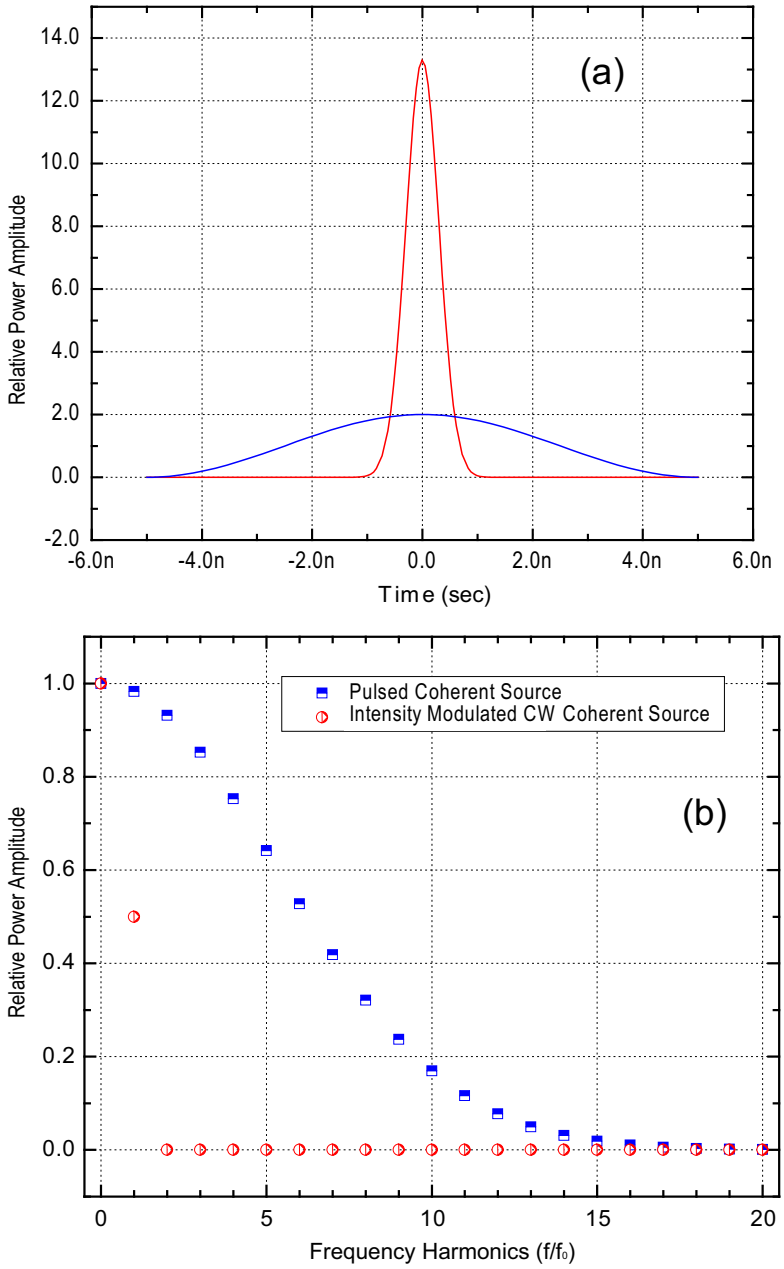

Figure 5.4: Wave form in the time and frequency domain for two types of optical intensity modulation, Gaussian and time harmonic (a) Time domain, (b) Frequency domain.

rated as -35 dBm when this laser unit is triggered at 1 MHz repetition rate. The polarization is not controlled for a Gaussian source like here.

The time harmonic irradiation is realized via a continuous wave (CW) laser diode modulated by a JDSU microwave (DC-20 GHz) optical intensity modulator. We apply a dc voltage at the V_π port to ensure the desired ON/OFF ratio, i.e. the lowest intensity should be more than 27 dB lower than the maximum output intensity. Note, since there is no absolute turning-off for the intensity modulator, there always has a weak optical-leak that is irradiating to the detector active area. The modulation depth is controlled by different levels of RF voltage applied at the RF port of the modulator. The modulation depth of this time harmonic irradiation is tuned to be one. The input optical signal is a continuous wave laser. The wavelength is selected to be 1310 nm. The input optical power is 850 μW, measured by a Newport optical power meter. The output signal is a polarized optical wave aligned to the crystalline direction of $LiNbO_3$.

5.4 Quantum Conversion Matrix Analysis

The detection and mixing are two closely related processes that occur simultaneously in a nonlinear device (see Sec. 5.07 in Ref. [4]). The main difference is primarily by how the output signal is used. When it is in the time domain, we call it detector. When in the frequency domain, we call it a mixer. In this section, we tried to analyze the optoelectronic mixing results. Both regimes of photon flux intensities are considered. Two assumptions are made during the following derivations

1. The kinetic inductance variation induced by the photon flux is the only mechanism to generate optoelectronic signals; Since the photon flux intensity is far below its optical critical power (defined in chapter 3); In addition, the working temperature of the optoelectronic mixer is far below T_c, so no bolometric effect is considered in our analysis;

2. The optoelectronic signal is so weak that such signal does not have any further nonlinear effect on the mixer. Here, it suggests that no higher orders of optoelectronic harmonics is above the noise level of our experimental measurement. In other words, the optoelectronic signal only has a linear transfer function.

We assume that the mixer is first acting as a kinetic inductance photodetector to convert photo power into optoelectronic signals. Bluzer have studied this type of detector theoretically in [125]. In his analysis, Rothwarf-Taylor rate equations were employed to calculate the photo induced quasiparticle density. However, our definition of current I_1 and I_2 is completely different from what was in [125].

Suppose the nanowire is dc biased with a constant current I_b, we define I_1 as the Cooper pair current / supercurrent injected into the superconducting nanowires; while I_2 is the supercurrent that leaves the nanowires. Without photon absorption, no nonequilibrium quasiparticle is generated, the values of I_1 and I_2 are therefore identical. So the relation $I_1 + I_2 = 2I_b$ holds. When the optical power is vertically coupled to the active area comprised of NbN nanowires, the absorbed photons cause destructive effect to the Cooper pair population, leading to the supercurrent difference between the total input and output supercurrent. The difference is due to the quasiparticle current induced by the depletion of Cooper pair population upon the absorption of photons. We define this current difference as the photocurrent $I_{ph} = I_1 - I_2$, which is the total nonequilibrium quasiparticle current. Unlike the semiconductor photocurrent, superconducting photocurrent can *not* be directly measured unless the nonequilibrium magnetic energy stored in the kinetic inductance of the NbN nanowire is released. Consequently, a voltage signal arising from time variation of the kinetic inductance becomes the only measurable. We can derive the similar photocurrent I_{ph} as in Ref. [125]

$$I_{ph} = \frac{I_b L_k}{(L_k + L_m)\, n_s} \eta_{eff} \tau_{eff}^{QP} N_\Phi \tag{5.1}$$

where τ_{eff}^{QP} is the effective quasiparticle lifetime; η_{eff} is the system level quantum efficiency including the system level optical coupling efficiency; n_s is the Cooper

pair density; L_k and L_m are kinetic and magnetic inductance, respectively; N_Φ is the photon density in the superconducting volume whose unit is $m^{-3} \cdot s{-}1$. The contributions to η_{eff} can thus be separated into optical absorption η_{abs} and breaking number of Cooper pairs. Considering $L_k >> L_m$; One absorbed photon can break multiple Cooper pairs and generate twice of $h\nu/\Delta$ quasiparticles. Then we are allowed to rewrite Eq. 5.1 as

$$I_{ph}(t) = \frac{4e^2}{m_e l^2} \eta_{abs} \tau_{eff}^{QP} \frac{\Phi(t)}{\Delta^\delta(T, \beta, I_0)} \wp(t) \tag{5.2}$$

where $\Phi(t) = L_k(t) I_b(t)$, $\wp(t)$ is the time varying optical power and can be expressed as a function of time harmonic or Gaussian pulse train [108]; $\Delta^\delta(T, \beta, I_0)$ is the nonequilibrium gap parameter, which is a function of temperature T, bias ratio β, and cw optical power intensity I_0; Its value can be computed by μ^* model developed in Chapter 3. m_e is electron mass; l is total length of the nanowire, i.e. 500 μm for this mixer. We have introduced a new term, total kinetic inductance flux $\Phi(t) = L_k(t) I_b(t)$. In order to take advantage of conversion matrices analysis method, we need to expand two terms in the product of $\Phi(t)$. Since we assume no harmonic product is generated by ω_2, the expansion of both terms can be written in the periodic pumping frequency f_1

$$L_k(t) = \sum_{n=-\infty}^{\infty} \tilde{L}_k^n \exp(jn\omega_1 t) \tag{5.3a}$$

$$I_b(t) = \exp(j\omega_0 t) \sum_{m=-\infty}^{\infty} \tilde{I}_m \exp(jm\omega_1 t) \tag{5.3b}$$

where $\omega_0 = (\omega_2 - \omega_1)$. So we can write $\Phi(t)$ as the product of Eqs. 5.3a and 5.3b

$$\Phi(t) = \exp(j\omega_0 t) \sum_{m=-\infty}^{\infty} \sum_{n=-\infty}^{\infty} \tilde{L}_k^n \tilde{I}_m \exp[j(m+n)\omega_1 t] \tag{5.4}$$

Then the voltage generated by the mixing of pumping RF power of f_1 with linear combination of photocurrent I_{ph} of f_2. The optical power can be expanded into single frequency components, but once each optical sinusoid is absorbed, only linear optoelectronic respond occurs, i.e. only single frequency optoelectronic signal is

produced. The voltage of the mixing products is

$$V(t) = \frac{d}{dt}\Phi(t) = \sum_{m=-\infty}^{\infty}\sum_{n=-\infty}^{\infty} j\left[(m+n)\omega_1 + \omega_0\right]\tilde{L}_k^n \tilde{I}_m \exp\left(\left[j(m+n)\omega_1 + \omega_0\right]t\right) \tag{5.5}$$

where

$$\tilde{L}_k^n = \frac{1}{T_1}\int_0^{T_1} L_k\left(\beta_b + \frac{I_{NL}(t)}{I_c^{GL}}\right)\exp\left(j2n\pi\frac{t}{T_1}\right)dt$$

Each $\tilde{L}_k^n$ can be readily evaluated by the simulation results of Harmonic Balance analysis reported in chapter 4. Now we are allowed to equate the right hand sides of Eq. 5.5 with $V(t) = \sum_{k=-\infty}^{\infty}\tilde{V}_k \exp\left[j\left(k\omega_1 + \omega_0\right)t\right]$ to obtain

$$\sum_{k=-\infty}^{\infty}\tilde{V}_k \exp\left(jk\omega_1 t\right) = \sum_{m=-\infty}^{\infty}\sum_{n=-\infty}^{\infty} j\left[(m+n)\omega_1 + \omega_0\right]\tilde{L}_k^n\tilde{I}_m \exp\left[j(m+n)\omega_1 t\right] \tag{5.6}$$

The above relation can be clearly expressed in the matrix products

$$\mathbf{V} = j\mathbf{\Omega}\mathbf{L}\mathbf{I} \tag{5.7}$$

Suppose the first N-terms are of the interest and we are able to write them in the matrix product format like

$$\begin{bmatrix} \tilde{V}_{-N} \\ \tilde{V}_{-N+1} \\ ... \\ \tilde{V}_N \end{bmatrix} = \begin{bmatrix} j\omega_{-N} & 0 & ... & ... \\ 0 & j\omega_{-N+1} & 0 & ... \\ ... & 0 & ... & 0 \\ 0 & ... & 0 & j\omega_N \end{bmatrix} \begin{bmatrix} \tilde{L}_k^0 & \tilde{L}_k^{-1} & ... & \tilde{L}_k^{-2N} \\ \tilde{L}_k^1 & \tilde{L}_k^0 & ... & L_k^{-2N+1} \\ ... & ... & ... & ... \\ \tilde{L}_k^{2N} & ... & ... & \tilde{L}_k^0 \end{bmatrix} \begin{bmatrix} \tilde{I}_{-N} \\ \tilde{I}_{-N+1} \\ ... \\ \tilde{I}_N \end{bmatrix} \tag{5.8}$$

in which we define $\omega_N = N\omega_1 + \omega_0$. Now we are able to list the first four opto-electronic mixing products induced by the fundamental frequency f_2 of the optical modulation signal as

$$\tilde{V}_0 = \tilde{V}_{f_2 - f_1} = j\omega_0\left(\tilde{L}_k^1\tilde{I}_1^* + \tilde{L}_k^{1*}\tilde{I}_1\right) \tag{5.9a}$$

$$\tilde{V}_1 = \tilde{V}_{f_2} = j\omega_2\left(\tilde{L}_k^0\tilde{I}_1 + \tilde{L}_k^2\tilde{I}_1^*\right) \tag{5.9b}$$

$$\tilde{V}_2 = \tilde{V}_{f_1+f_2} = j\left(\omega_0 + 2\omega_1\right)\left(\tilde{L}_k^1\tilde{I}_1^* + \tilde{L}_k^3\tilde{I}_1\right) \tag{5.9c}$$

$$\tilde{V}_3 = \tilde{V}_{2f_1+f_2} = j\left(\omega_0 + 3\omega_1\right)\left(\tilde{L}_k^2\tilde{I}_1 + \tilde{L}_k^4\tilde{I}_1^*\right) \tag{5.9d}$$

And the first two optoelectronic mixing products induced by the second frequency component ($2f_2$ due to the periodic optical singal) of the optical modulation signal as

$$\tilde{V}_0^{2f_2} = \tilde{V}_{2f_2-f_1} = j\left(2\omega_2 - \omega_1\right)\left[\tilde{L}_k^1\left(\tilde{I}_1^{*2f_2}\right) + \tilde{L}_k^{1*}\left(\tilde{I}_1^{2f_2}\right)\right] \tag{5.10a}$$

$$\tilde{V}_1^{2f_2} = \tilde{V}_{2f_2} = j2\omega_2\left[\tilde{L}_k^0\left(\tilde{I}_1^{2f_2}\right) + \tilde{L}_k^2\left({}^2\tilde{I}_1^{*2f_2}\right)\right] \tag{5.10b}$$

In the following sections, we will use Eqs. 5.9a - 5.9d and 5.10a - 5.10b to understand the voltage amplitudes of two sets of optoelectronic mixing experiments in the classical and quantum optical photon levels, respectively. Each of them contains six mixing product measurements.

5.5 Results of Classical Optoelectronic Mixing

To explore the optoelectronic mixing effects in SNSPD, we have performed the mixing tests under combinations of the thermal bath temperature T, bias current I_b, and the optical intensities I_0. The optical intensity is controlled by a EXFO Variable Optical Attenuator (VOA) as shown in Fig.5.3.

One RF power (f_1) is used as the local oscillator (LO) of a mixer. The values of mixing frequency pair are selected to avoid the degeneration of frequency components. After detailed numerical evaluation, only a few pairs fall into this criterion, e.g. 12 MHz and 100 MHz in this work. We make f_1=12 MHz, considering the RF power absorption rate due to nonlinear properties of the nanowire. Two types of optical wave excitations, i.e. time-harmonic and pulsed periodic irradiations have been adopted in the tests. The optical modulation frequency f_2 then is chosen to be 100 MHz, for both types of optical signals [1].

Fig. 5.5 (a)-(f) displays the optoelectronic mixing results measured when the ambient temperature was set to be 7.5 K. We use three levels of bias current,

[1]The choice of a mixing frequency pair is different from that of two-tone measurement. In most microwave nonlinear characterization tests, the frequency spacing between two equal power tones is less that 1% of the center frequency of the two tones.

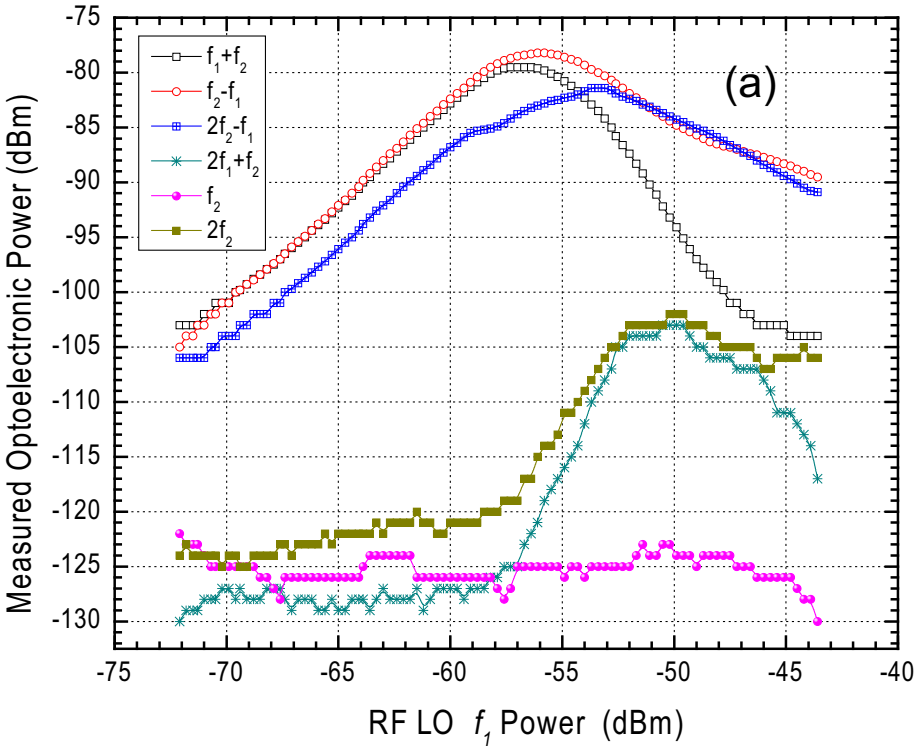
(a)
f1+f2
f2-f1
2f2-f1
2f1+f2
f2
2f2
Measured Optoelectronic Power (dBm)
RF LO f1 Power (dBm)
-75
-80
-85
-90
-95
-100
-105
-110
-115
-120
-125
-130
-75
-70
-65
-60
-55
-50
-45
-40

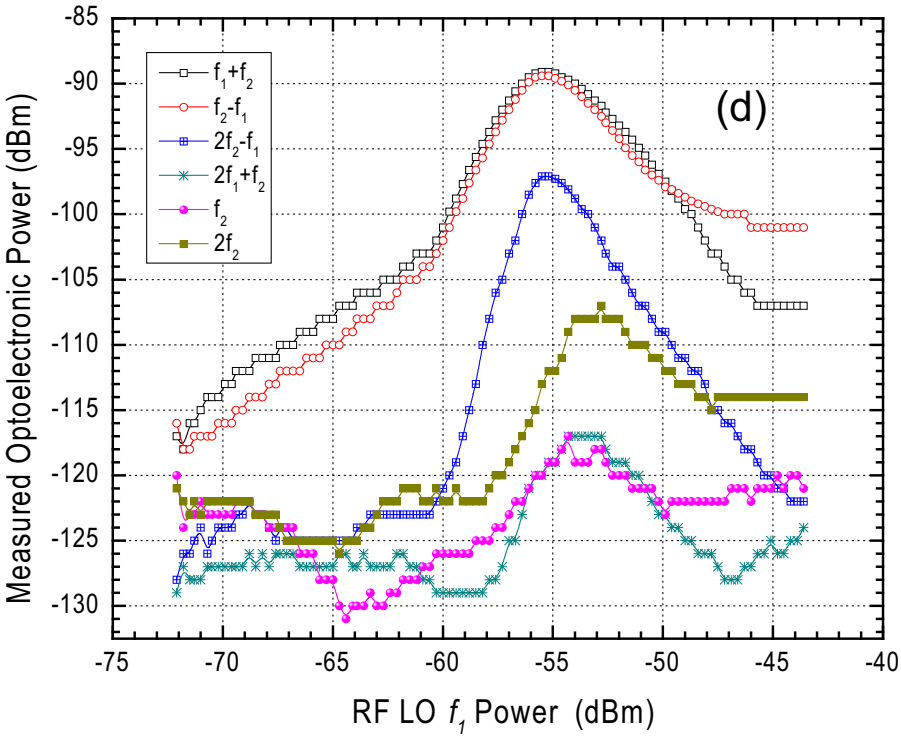
(d)
f1+f2
f2-f1
2f2-f1
2f1+f2
f2
2f2
Measured Optoelectronic Power (dBm)
RF LO f1 Power (dBm)
-85
-90
-95
-100
-105
-110
-115
-120
-125
-130
-75
-70
-65
-60
-55
-50
-45
-40

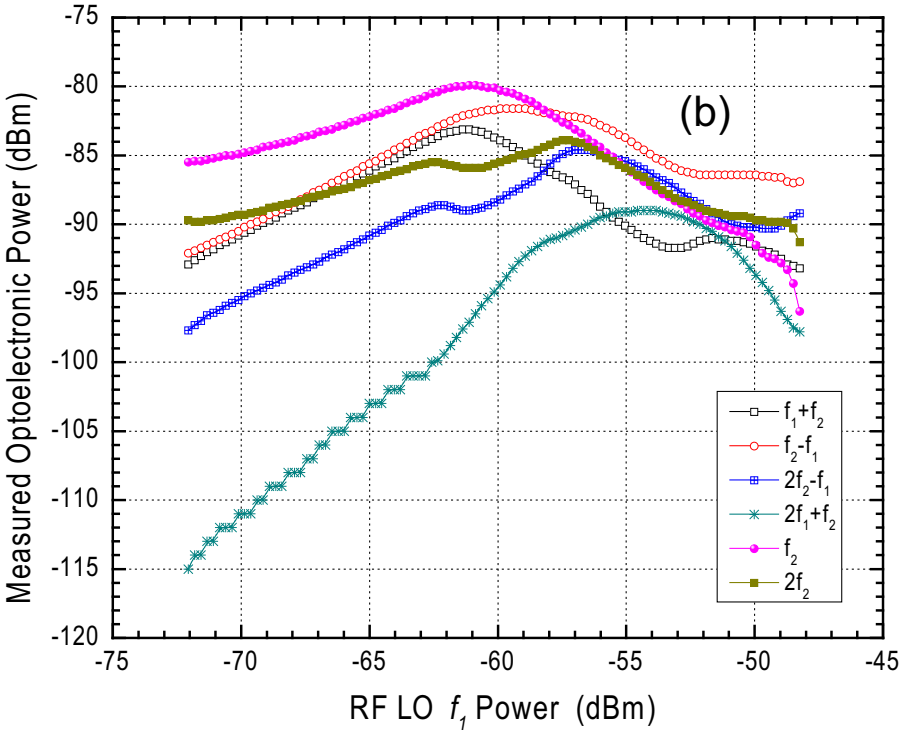
(b)
Measured Optoelectronic Power (dBm)
RF LO f_1 Power (dBm)
f_1+f_2
f_2-f_1
$2f_2-f_1$
$2f_1+f_2$
f_2
$2f_2$

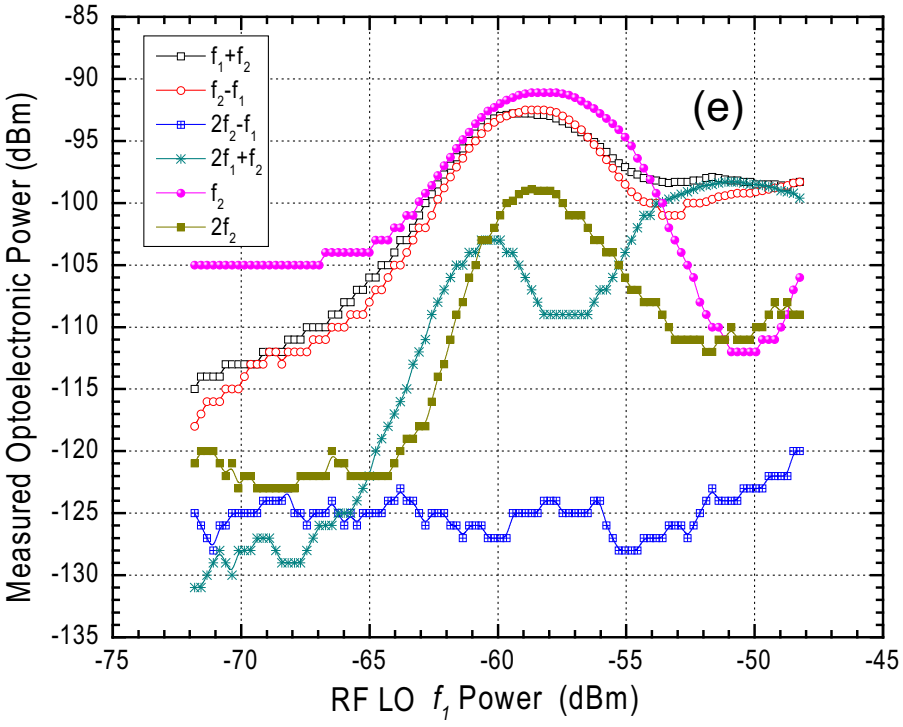
(e)
Measured Optoelectronic Power (dBm)
RF LO f_1 Power (dBm)
f_1+f_2
f_2-f_1
$2f_2-f_1$
$2f_1+f_2$
f_2
$2f_2$

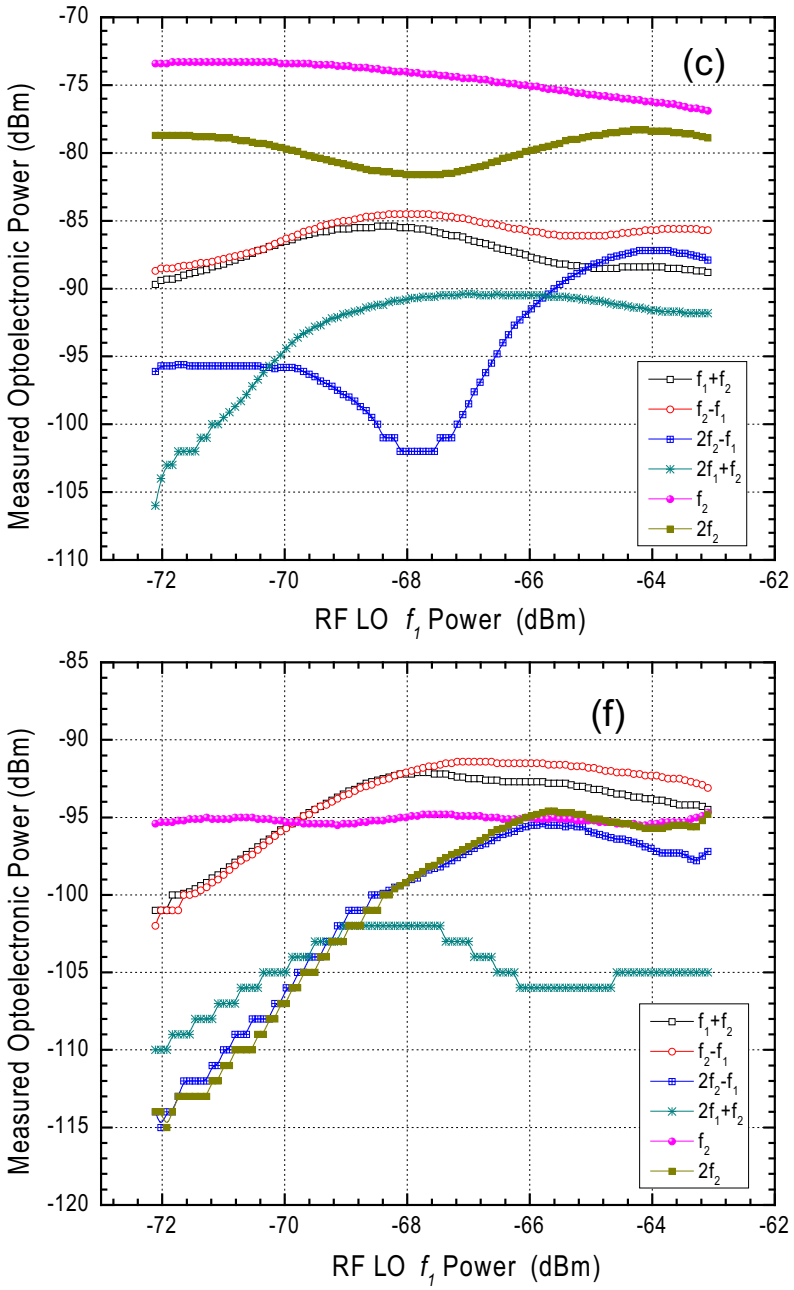

Figure 5.5: All measurements are undertaken at the temperature of 7.5 K. Plots (a) to (c) are optically excited by the pulsed laser whose repetition rate is set to 100 MHz; plots (d) to (f) are optically excited by a time harmonic irradiation, achieved via an intensity modulated CW laser whose modulate frequency is 100 MHz, and the modulation depth is close to one. The bias current for plots (a) & (d) is zero, plots (b) & (e) is 2.5 μA, and plots (c) & (f) is 5 μA, respectively.

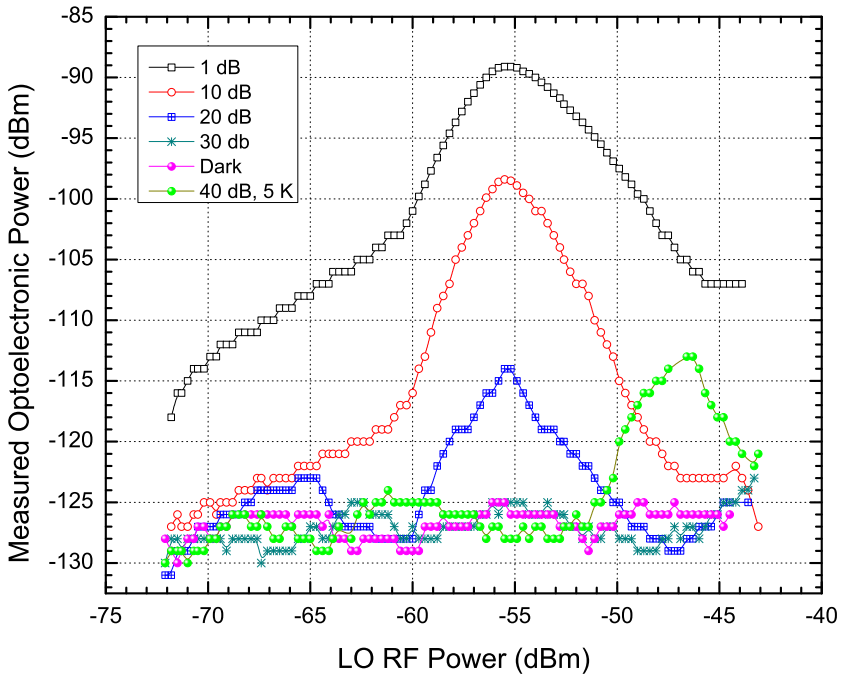

Figure 5.6: Optoelectronic mixing term $f_1 + f_2$ under different levels of optical power and two temperatures of 7.5 K and 5 K.

provided that the critical current at this temperature is 6.8 μA. From the quantum conversion matrix analysis, we choose the first four mixing components induced by the fundamental harmonic of photocurrent, i.e. $f_2 - f_1$, f_2, $f_1 + f_2$, $2f_1 + f_2$; the first two mixing components and $2f_2$ and $2f_2 - f_1$.

Fig. 5.5 (a) and (d) show the optoelectronic mixing components when the dc bias is zero. We are able to observe almost all mixing components that increase with the LO RF power to a peak and then decreases, although no appreciable $\tilde{V}_{f_2}$ and $\tilde{V}_{2f_2}$ components can be measured at lower pumping power. This is consistent with what Eq. 5.9b implies, because $\tilde{L}_k^0 = 0$ when dc bias is zero. The term $\tilde{L}_k^2$ in principle should also be zero, due to the even function of $L_k(t)$ under zero dc bias. However, this condition is only valid when a pure kinetic inductance is the nonlinear load of transmission line. For the SNSPD nanowire, when the pumping power is high, $\tilde{L}_k^2$ can be nontrivial, because the nonzero R_s in Fig. 4.6 modifies the symmetry of $L_k(t)$ induced by the strong RF pumping power.

Fig. 5.5 (b) and (e) display the mixing components when the dc bias current is 2.5 μA. At very low LO RF power, for the sinusoidal case, amplitude of f_2 keeps constant until about -65 dBm and starts follow the same trend as other mixing components. For the pulsed case, we only observe f_2 exhibits higher amplitude than the rest of mixing terms, which is due to nonzero $\tilde{L}_k^0$ contribute the most. The same rationale for $\tilde{V}_{2f_2}$ in Fig. 5.5 (b); but for the case in Fig. 5.5 (e), because the optical second harmonic is strongly suppressed, which results in no $\tilde{V}_{2f_2-f_1}$ output ($\tilde{I}_1^{2f_2} = 0$).

Fig. 5.5 (c) and (f) shows the optoelectronic mixing components when the dc bias current is very close to critical current, i.e. 5 μA. Now the amplitudes of f_2 remain almost constant for both types of optical signals. Mixing component $2f_2$ in Fig. 5.5 (c) is the second highest, due to the strong Fourier terms for L_k. In Fig. 5.5 (f), $\tilde{V}_{2f_2}$ and $\tilde{V}_{2f_2-f_1}$ are very low at at pumping power due to $\tilde{I}_1^{2f_2} \simeq 0$. Their increase with the increasing pumping power may result from other strong mixing effect.

We also measured the optoelectronic mixings under different photon flux intensities at 7.5 K and 5 K temperatures for a time-harmonic optical irradiation. Fig. 5.6 displays four levels of optical powers at 7.5 K. The dc bias current for this plot is zero. At 7.5 K, we are not able to identify 30 dB attenuation and dark photon flux. When the temperature is lowered to 5 K while still keeping zero dc bias , we can even measure optoelectronic mixings at attenuation level of 40 dB to the input optical power, which is corresponding to less than 10 photons per device area in one time harmonic cycle. This observation suggests that the reduced operating temperature is responsible for the enhanced sensitivity of the DUT, possibly because of the increased quasiparticle lifetime τ_{eff}^{QP}. The effective lifetime exponentially decreases with the DUT temperature. The detailed discussion about the quasiparticle lifetime and its interaction with phonons, readers can refer to [145].

5.6 Results of Single Photon Mixing

This section, we are going to report the single photon mixing, in which the photon flux is on average lower or very lower than one photon in a pulse. In addition, we also tried to include the sinusoidal modulation case, in the latter scenario, in each cycle the photon number on average is below one.

The theory of quantum mixing in a tunneling superconducting junctions were developed by Tucker, Feldman, *et al.* [23], [143]-[144]. Those quantum mixers are taking advantage of their dc nonlinearity. The assumption is made if the incident photon energy is higher than the dc nonlinearity width, then a quantum mixing effect is possible. The LO frequency of the quantum mixer must be close to its gap frequency $\omega_g = \Delta/\hbar$ (SNS junction). In the case of NbN based mixer, ω_g is in the order of 200 GHz. It is much higher than the repetition rate of the pulsed laser, which only ranges up to a few hundreds of MHz. Therefore, the mixer in this thesis is quite different from the ones mentioned above.

The LO is chosen considering the electrical absorption rate as the function of RF frequency, which in turn have been tested in the one tone measurement, and we conclude that lower frequencies favor the absorption of RF LO signals. Thus we use 12 MHz frequency as the LO frequency. For the mixing degeneracy, is another factor to consider when determining the optical modulation frequency for CW time harmonic as well as the repetition rate for pulsed lasers. Second, the photon signal actually has been included in an envelope of the incident electromagnetic field, instead of the high frequency itself, in other words, the detection, or demodulation of the envelope is actually the important process before any mixing occurs.

Fig. 5.7 illustrate single photon mixing results. All measurements are performed when the average photon number μ per pulse/period (for pulsed/time-harmonic source) is very close or less than one, and the frequency of optical signals is 100 MHz for both pulsed and time-harmonic based coherent photon sources. We tested different combinations of temperature T, bias current I_b, type of photon source and average photon number. The combination of various conditions is useful to show

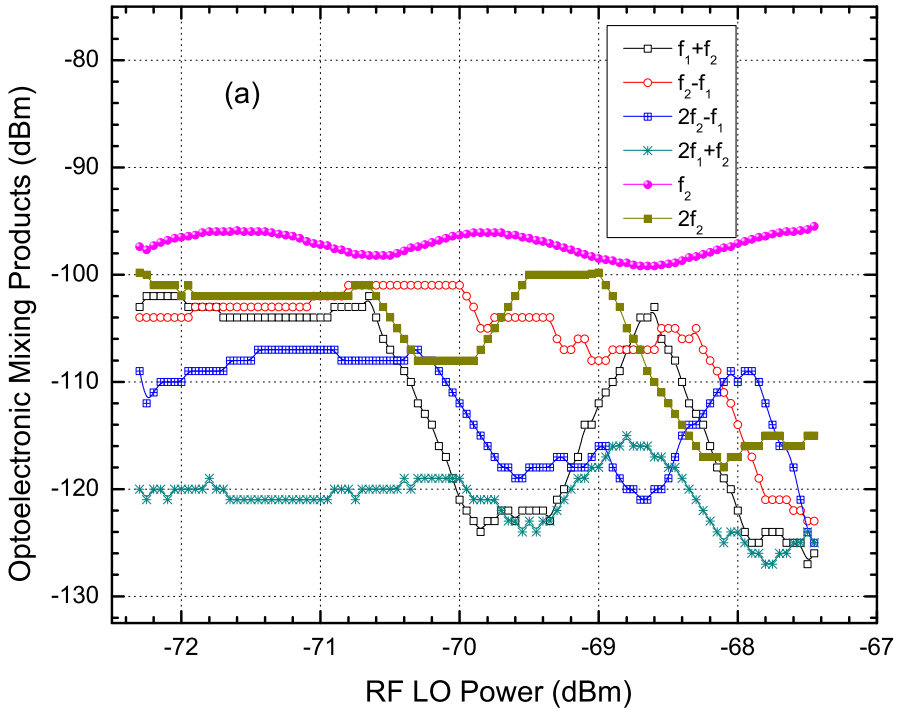
(a)
f1+f2
f2-f1
2f2-f1
2f1+f2
f2
2f2
Optoelectronic Mixing Products (dBm)
-80
-90
-100
-110
-120
-130
-72
-71
-70
-69
-68
-67
RF LO Power (dBm)

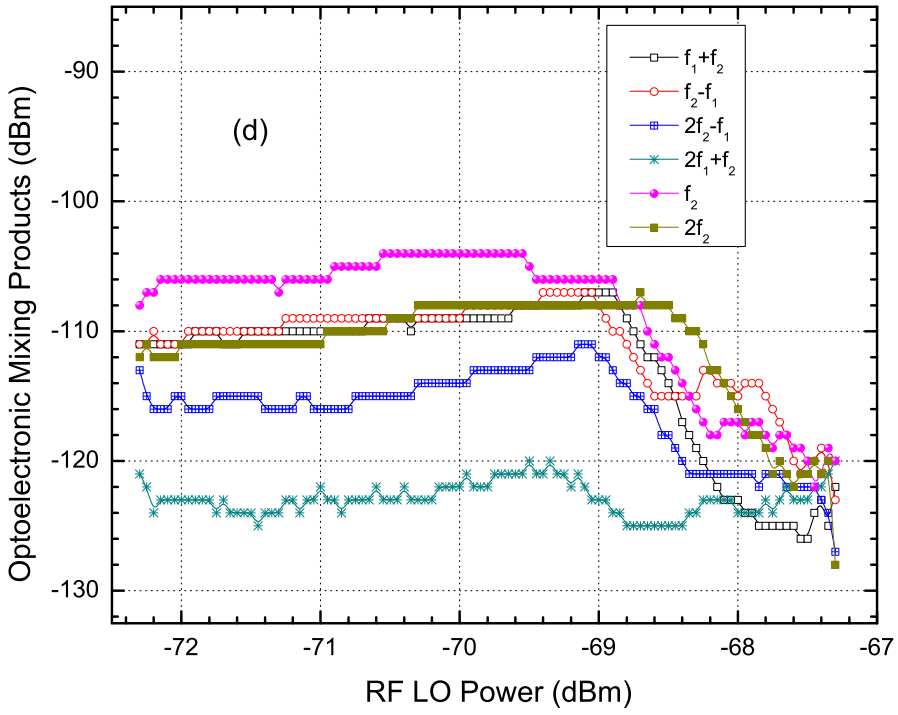
(d)
f1+f2
f2-f1
2f2-f1
2f1+f2
f2
2f2
Optoelectronic Mixing Products (dBm)
-90
-100
-110
-120
-130
-72
-71
-70
-69
-68
-67
RF LO Power (dBm)

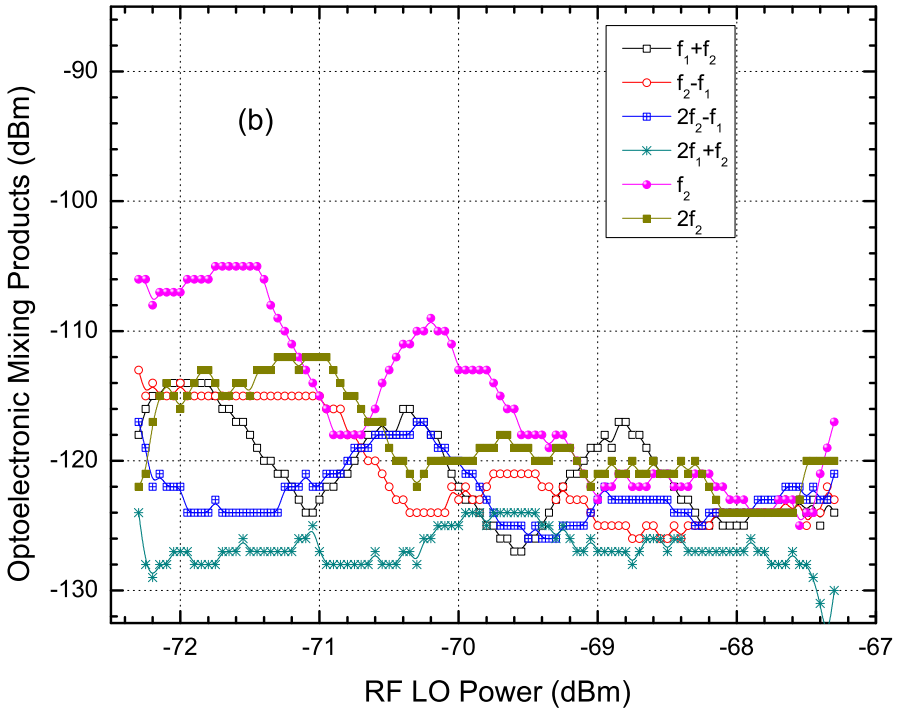
(b)
Optoelectronic Mixing Products (dBm)
RF LO Power (dBm)
f1+f2
f2-f1
2f2-f1
2f1+f2
f2
2f2
-90
-100
-110
-120
-130
-72
-71
-70
-69
-68
-67

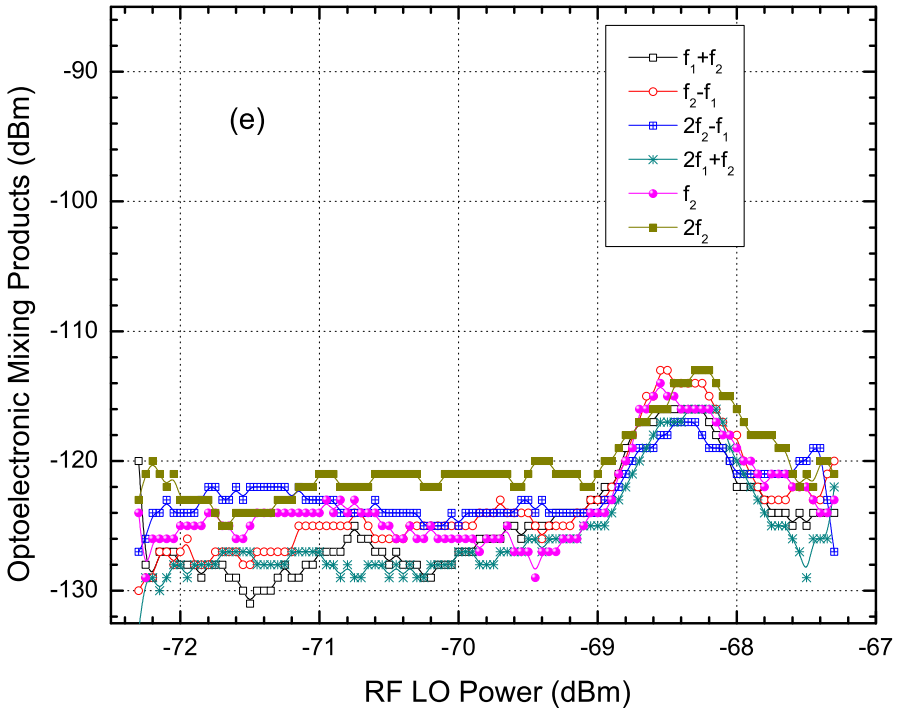
(e)
Optoelectronic Mixing Products (dBm)
RF LO Power (dBm)
f1+f2
f2-f1
2f2-f1
2f1+f2
f2
2f2
-90
-100
-110
-120
-130
-72
-71
-70
-69
-68
-67

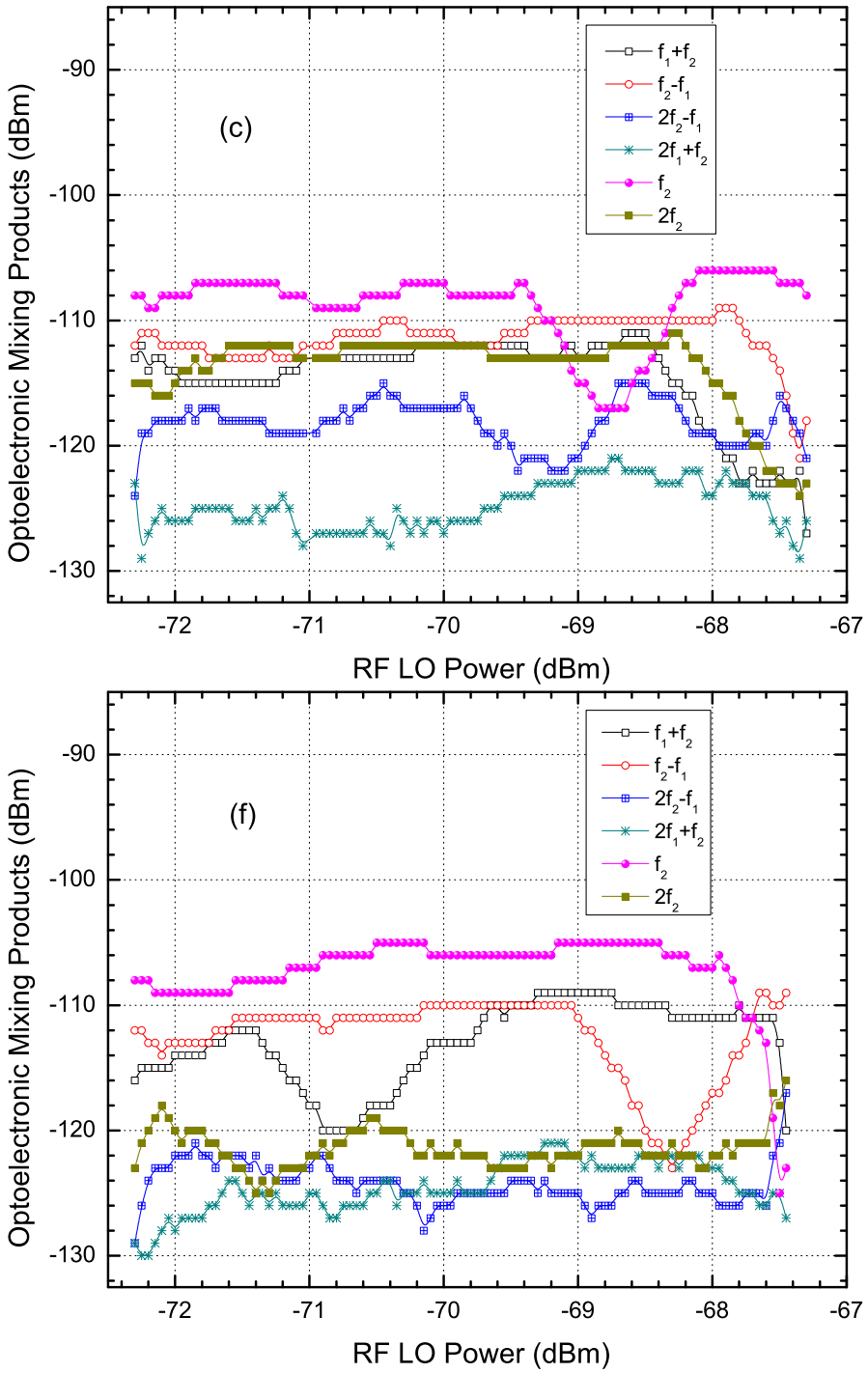

Figure 5.7: Single photon mixng results, (a) T =4.6 K, I_b =22 μA, pulsed, $\mu \approx 0.6$; plot (b) T =4.0 K, I_b =25.8 μA, pulsed, $\mu \approx 0.02$; plot (c), T =4.6 K, I_b =22 μA, pulsed, $\mu \approx 0.2$; plot (d) T =5.0 K, I_b =19.5 μA, pulsed, $\mu \approx 0.6$; plot (e) T =5.0 K, I_b =10 μA, pulsed, $\mu \approx 0.6$; and plot (f) T =4.6 K, I_b =22 μA, time-harmonic, $\mu \approx 1.5$; the critical current for T =5.0 K, 4.6 K, and 4.0 K are 21.7 μA, 25 μA, and 27.5 μA, respectively.

the contribution of each element to mixing product.

In the Fig. 5.7 (a), the highest power in the mixing product is f_2, which is governed by Eq. 5.9b. The first term in $\tilde{L}_k^0 \tilde{I}_1 + \tilde{L}_k^2 \tilde{I}_1^*$ has the dominant contribution, observing that $\tilde{L}_k^0 \gg \tilde{L}_k^2$, $\tilde{I}_1 = -\tilde{I}_1^*$. The lowest power of the mixing products is $2f_1 + f_2$, which governed by Eq. 5.9d. In the relation, we noticed that both $\tilde{L}_k^2$ and $\tilde{L}_k^4$ are even orders of the RF-pumped L_k Fourier terms. Due to the strong dc bias, the odd orders in the Fourier expansion of L_k are more favored. So the mixing product of $2f_1 + f_2$ has the lowest power output. Only at pumping power at 68.8 dBm, it has a small peak value at about -115 dBm. This is because of the value of R_s becomes significantly unstable when the RF LO power is higher than -70 dBm, leading to an extraordinarily strong nonlinearity in L_k. We can also see output power amplitudes of other mixing components except f_2 experiencing the same fluctuation, because $\tilde{L}_k^0$ is mostly determined by the dc bias, unless R_s becomes too large to cause permanent latching in the nanowire. The value of R_s is strongly affected by the total bias current of dc and absorbed RF pumping currents.

In the Fig. 5.7 (b), in order to increase the sensitivity of the mixer, more bias current is required with the help of temperature $T = 4.0$ K. Because dc bias ratio (94%) is so close to I_c, RF LO power at -71.5 dBm makes the best sensitivity to average photon per pulse at $\mu \approx 0.02$, most probably because the term $\tilde{L}_k^0$ has the significant contribution. The mixing products $\tilde{V}_{f_2-f_1} > \tilde{V}_{2f_1+f_2}$ is due to $\tilde{I} \gg {}^2\tilde{I}_1$. For the rest of mixing products, their relative output power levels are following the same rationale. In the Fig. 5.7 (c), all of the conditions are kept the same except for the average photon number per pulse is lowered three times. The significant changes on the output power levels of almost all six mixing products are, they all consistently decrease by about 10 dB in comparison to measured power levels in Fig. 5.7 (a). For $\tilde{V}_{2f_1+f_2}$, its reduction is slightly lower than the anticipated 10 dB, mainly because its power level almost touches the noise floor of our testing system. Therefore, this experimental result strongly imply that the photon induced photocurrent I_{ph} is reduced in responses to lower level of incoming photon flux.

In the Fig. 5.7 (d), the conditions are the same as the Fig. 5.7 (a), except for higher temperature, and dc bias ratio is less than 2% higher. However, the mixing products are systematically 10 dB lower than those in Fig. 5.7 (a), given the same photon flux level. This strongly suggests that the photon induced photocurrent is reduced due to quasi-particle life time is exponentially shorter at higher temperatures [125, 145]. Therefore, we anticipate much stronger single photon mixing in the milli-Kelvin temperatures.

In the Fig. 5.7 (e), we supply less than 50% ratio of dc bias, the rest conditions are the same as the Fig. 5.7 (d). The plot indicates that almost all of the mixing products within 10 dB dynamic range. We attribute this to the reduction of Fourier transformation terms of L_k at lower dc bias ratios.

In the Fig. 5.7 (f), we use time-harmonic single photon signal. It has been achieved by the optical intensity modulator. From Fig. 5.4, we know that it is very unlikely to have photocurrent induced by its $2f_2$ component. From the figure, just as we anticipate, $\tilde{V}_{2f_2}$ and $\tilde{V}_{2f_2-f_1}$ are all very close the noise floor, which agrees with the conversion matrices analysis. However, in order to obtain a pronounced mixing, the photon flux intensity has to be tuned higher, because the relative power spectrum for the same frequency component, time harmonic wave at f_2 is much lower than pulse photon source. Note, the shot noise in the long sinusoidal period may be dominant, which can result in very high noise floor displayed at the photon detection output. This has been verified in this test, where at least 3 times higher photon flux level is required to overcome the noise floor, compared to the pulsed photon source.

After the above discussions on various conditional combinations, we will focus on fixing temperature and bias current, only change the average photon number. Fig. 5.8 shows the mixing product whose frequency is f_2. This mixing product is of the special interest, because it is the optical repetition frequency. We vary the photon flux from complete dark to 0.6 photon per pulse at four steps, i.e. 0, 0.02, 0.2 and 0.6 photons per pulse, for 100 MHz repetitive Gaussian-pulsed laser source.

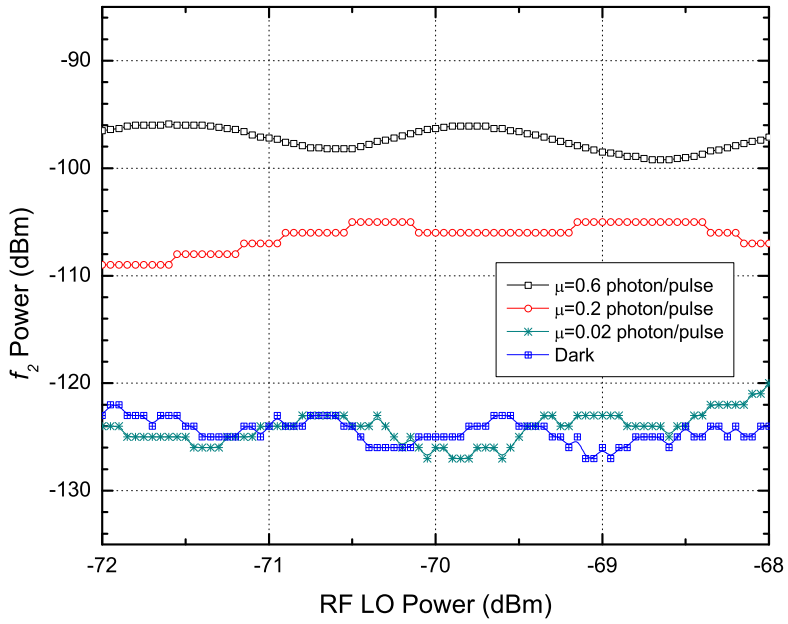

Figure 5.8: Single photon mixing at frequency of f_2 under different average photon levels as indicated in the plot; the bias current is 22 μA at temperature of 4.6K.

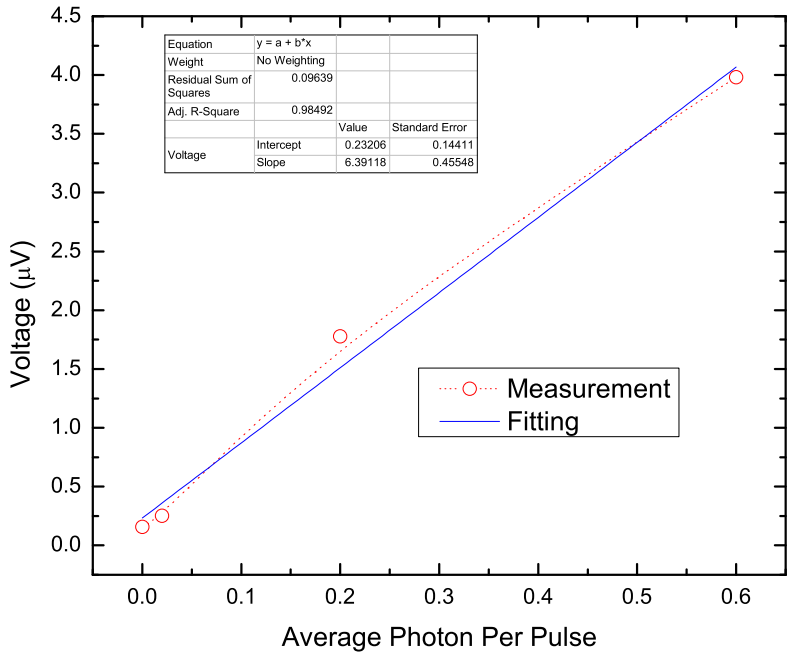

Figure 5.9: The output voltage amplitude of the single photon mixing at frequency of f_2 under different average photon numbers per pulse. The bias current is 22 μA at temperature of 4.6K; solid line is the linear fitting curve.

RF LO frequency is chosen to be at 12 MHz. At -69 dBm input, the mixing power output are -126 dBm, -122 dBm, -105 dBm, and -98 dBm, respectively.

Eq. 5.9b and Eq. 5.1 together expect a linear relation between the mixing voltage $|\tilde{V}_{f_2}|$ with respect to average photon number per pulse at a constant repetition rate. Fig. 5.9 illustrates the voltage amplitudes at 0, 0.02, 0.2 and 0.6 photons per pulse. The comparison to the linear fitting curve demonstrates that the output voltage of our single photon mixer agrees with the quantum conversion matrix analysis. As what we anticipate, the mixing output voltage is linearly proportional to average photon even in the quantum optical regime at 4.6 K. One will achieve better photon number resolution by lowering operating temperature, e.g. at 4.2 K.

5.7 Summary

In this chapter, we first discuss and compare different types of solid state frequency mixers. Then the electrically pumped optoelectronic mixer made of superconducting nanowires has been tested under two photon flux levels, in the classical and single photon regimes. In both cases, we perform our tests by varying combinations of conditions, including 1.) The intensity modulation by sine and Gaussian waves; 2.) Varying the attenuation levels of incident optical powers; 3.) Changing the operational temperatures; 4.) Scanning the RF power to the local oscillator port; 5.) Setting different ratios of dc bias current to critical/maximum current I_c. Quantum conversion matrix method is employed to explain the optoelectronic mixing effect in the superconducting nonlinear nanowires. The experimental results consistently confirms that the optoelectronic mixing occurs. In all tests, the optoelectronic mixing behaves like strong electrical and weak opto-to-electronic mixing, because only the pure electrical sinusoid can generate higher orders of harmonics.

Larger modulation index, appeared in the Gaussian wave modulation, results in a higher mixing outputs than that caused by time-harmonic one, given the same level of input average power of the optical signal. The experimental result also

suggests that the operating temperature is mainly responsible for increasing the mixing effect, possibly because the quasiparticle lifetime is strongly affected by its ambient temperature, for detailed theoretical background, readers can refer to [145]-[147]. This leads us to conceive the possibility of making it as a quantum optoelectronic mixer low temperatures (e.g. $\sim$ 4.2 K), when the photon flux on average less than one photon. This anticipation is verified after we performed the single photon mixing measurements.

Chapter 6

Conclusion

First we have reported a robust packaging of the device that allows us to perform the quantum and classical optoelectronic, and RF/microwave measurements. The thermal controlling, optical and electrical insertion loss are all satisfactory for the complete set of experimental operations. The circuit model to account for the photoresponse is presented and in particular we try to compare the experimental results by different interconnecting components. The simulation results enable us to attribute the limitations to the rising and falling time of the photoresponse pulse to the finite bandwidth in the cryogenic cables; as well as RF amplifiers.

Second, the small signal RF/microwave measurements are performed. We introduced a two step method to separate the superconducting kinetic inductance from other linear reactive elements. This method can be implemented to characterize many superconducting circuits, such as superconducting phase qubits. Based on this method, we systematically investigated Cooper pair density as modulated by the dc bias, in the presence and absence of optical irradiations.

Third, the large signal RF/microwave measurements including one-tone and two-tone measurements have unveiled the possibilities of achieving strong electrically induced nonlinearity in the SNSPD nanowires. Two typical methods of nonlinear microwave circuit analysis are implemented. The results of the simulation provides us with quantitative understanding to the nonlinearity.

Lastly, the optoelectronic mixing has been successfully found in the SNSPD nanowires as an electrically pumped optoelectronic mixer. The quantum conversion matrices analysis can account for the mixing products, in particular when the optical input signal is relatively weak, such as at the level of single photon flux intensity. The optoelectronic mixing effect has been experimentally confirmed, when the optical input is in either classical or single photon regime.

6.1 Summary of Contributions

The contributions of this thesis are categorized into four aspects: Firstly, the packaging and experimental setup for optoelectronic characterization; Secondly, investigation of static nonlinearity; Thirdly, electrically induced nonlinearity by large signal RF/microwave signals; Lastly, electrically pumped optoelectronic mixer. In the following subsections, we will elaborate them in more detail.

6.1.1 SNSPD Packaging and Optoelectronic Characterization

1. Established the experimental setup and procedure to perform optoelectronic characterization for SNSPDs, including dark count, quantum efficiency and detection efficiency. The experimental setup has fully considered optical, cryogenic; and microwave electrical integration. The packaging allows us to preform optoelectronic characterization; RF/microwave measurement; optoelectronic mixing including the classical light; and in the single photon regime. The cryogenic transmission line has low insertion loss at the gigahertz range.

2. The rising time and falling has been simulated as intrinsic time; the comparison to the two measurements under two cryogenic cables indicates that the speed of interconnecting components are crucial to achieve the highest rising time possible.

3. Relevant paper published, **Yan, Z.**, Majedi, A. H. and Safavi-Naeini, S. (2007) Physical Modeling of Hot-Electron Superconducting Single Photon Detectors, IEEE Transactions on Applied Superconductivity, vol. 17:3, pp. 3789-3794.

4. Relevant paper published, **Yan, Z.**, Akhlaghi, M. K. ; Orgiazzi, JL. ; and Majedi, A. H., (2009) Optoelectronic Characterization of Fiber-Coupled NbN Superconducting Nanowire Single Photon Detector, Journal of Modern Optics, vol. 56, pp. 380-4.

6.1.2 Static Nonlinearity in the Superconducting Nanowires

1. Devised a two-step measurement, in which the room-temperature measurement to separate non-superconductive elements from superconducting elements. The method becomes a practical set of experimental methods to explore the Cooper pair density at cryogenic temperatures, where a standard calibration can not be carried out;

2. Ultra small signal S-parameter measurement to characterize cryogenic nano device. The SNSPD L_k can be measured with the best accuracy under the highest bias ratio (close to 99%, less than 90% in reported literatures [63].);

3. DC characterization to recover four regimes by voltage bias. The attempt has been made to model the superconducting state; switched state conduction; and smoothly connect to the self-heating model

4. The strong-weaklinks inherent to NbN films is revealed. The linear temperature dependence of I_c is found experimentally; and studied on the basis of tunneling across the weaklink barriers;

5. Nonlinear property of kinetic inductance (KI) based on Ginsburg-Landau theory has been developed. First rigorous analytical relationship has been derived to express the variation of KI to the bias current ratio with respect

to its critical current. The KI parametric variation under bias current is compared to the experimental results. The comparison provides us deeper understanding of I_c against the bulk critical current.

6. Nonequilibrium chemical potential μ^* model and optical critical power analysis have been implemented to provide a relatively tangible theory background. We confirmed that it is a viable method to model the superconducting nanowire nonlinearity in the presence of cw optical powers.

7. Relevant paper published, **Yan, Z.** and Majedi, A. H., (2009) Experimental Investigations on Nonlinear Properties of Superconducting Nanowire Meanderline in RF and Microwave Frequencies, IEEE Transactions on Applied Superconductivity, vol.19:5, pp. 3722-3729.

8. Relevant paper published, **Yan, Z.** and Majedi, A. H., (2009) A Complete Set of Characterizations on the NbN Superconducting Nanowire Single Photon Detectors, in proceedings of TIC-STH Symposium on Superconductivity - From Physics to Engineering, Toronto, ON, Canada. pp. 1015-1020.

6.1.3 Strong Nonlinearity Induced by Large Electrical Signals

1. Equivalent circuit model containing the nonlinear component as the load of transmission line; Numerical simulations are performed to quantitatively study the matching of the nonlinear load; and its absorption of the RF power on the basis of G-L theorem.

2. The time domain analysis and harmonic balance method as time-frequency hybrid domain analysis are employed to simulate the reflected higher orders of harmonic as well as mixing products, generated by the input RF power and dc bias.

3. The harmonic balance method provides more complete analysis of the nonlinear circuitry as the load of TL; In particular, it becomes an efficient method to quantitatively study the quasi-particle conduction, which leads to the nonlinear resistance modeled by R_s in Fig. 4.6. The value of R_s is the most complicate parameter to be determined; and sometimes R_s strongly affects the pure Cooper nonlinearity described by the simple nonlinear kinetic inductance.

6.1.4 Classical and Quantum Optoelectronic Mixer

1. Propose and implement the electrically pumped optoelectronic mixer in the nanowires of SNSPD. Optoelectronic mixing effect has been experimentally confirmed and studied in the nanowires of SNSPD.

2. Exploit the quantum conversion matrix method to combine quantum kinetic inductance detection theory and nonlinear microwave circuit analysis. The method can quantitatively analyze the optoelectronic mixer, and calculate mixing products. The photocurrent derived by quantum kinetic inductance provides deeper insights on the parameters that determine the mixing effect.

3. First time to introduce the optoelectronic mixer that are sensitive to single photon level, so called single photon optoelectronic mixer.

4. The experimental setup can be used to test different combinations of conditions to locate the maximized single photon mixing.

5. Relevant paper published, **Yan, Z.** and Majedi, A. H., (2009) Optoelectronic Mixings in the NbN Superconducting Nanowire Single Photon Detectors, SPIE Proceedings, Vol. 7386, p.p. 73861U, 9 pages.

6. Contributed talk, **Yan, Z.** and Majedi, A. H. (2009) Single photon optoelectronic mixing in the NbN superconducting nanowires, presented in Single Photon Workshop 2009 - NIST, Boulder, Colorado, USA.

6.2 Future Research Perspectives

In the experimental aspect, the polarization, wavelength and temperature dependencies that affect the SNSPD QE are pending to be explored. The raw SNSPD packaging can be further optimized to increase the system quantum efficiency. The main improvement will be reducing the free space gap between the fiber tip to the active area. To achieve this, more accurate alignment stage has to be employed.

A pair of packaged SNSPDs is desirable for characterizing the entangled photon source, which is implemented by quantum dots or spontaneous parametric down conversion crystals. The packaged pair SNSPD can be achieved by modifying the current housing. So far, only one device is operable in the cryostat. Given the geometrical sizes of cold plate, it is possible to accommodate two SNSPDs together. The optical fiber integration and alignment will be more challenging, but the packaging principles keep unchanged.

The timing jitter characterization of SNSPD can be fulfilled once a short pulse width (<30 ps) laser is available. The jitter time is the very important parameter for SNSPD, particularly when it is used for the time correlation measurement of the entangled photon source; as well as in the practical QKD systems.

The single photon mixing requires time domain analysis; and more sophisticated electronic engineering is required, because the noise floor of the current setup still has about 30 dB room to reach the theoretical limit of the room temperature noise floor; The cryogenic amplifier can be used to lower the noise when novel mixing/detection scheme is attempted to improve the signal over noise ratio.

The hotwire self-heating model to account for the fourth regime in the dc I-V measurement. We anticipate this regime can be well modeled by a good physical modeling tool, such as COMSOL-multiphysics environment, which integrates a finite-element solver with physical partial differential equations.

The single photon detection theory on the basis of quantum optics and macroscopic quantum picture, or microscopic BCS theory is definitely desirable. So far

the hot spot model relies on a phenomenological interpretation that has some unsolved self-contradictory problems, e.g. there is no abrupt disappearance of single photon detection with wavelengths.

The optical cavity and surface plasmonic layer are two promising approaches to enhance the optical coupling. So far, more than 80 % of QE is reported at 1550 nm wavelength. They both require nanofabrication facilities and techniques. If these technical conditions are available, both approaches can be realized. Furthermore, integrated optical circuits, such as optical ridge waveguides, and polarizers may be also fabricated on the same chip. The packaging of the re-engineered detector on the chip can be tailored to comply the optoelectronic industrial standard.

APPENDICES

A Ginsburg Landau Theory and Kinetic Inductance in a dc Biased Superconducting Wire

The Cooper pair density is proportional to the wave function intensity, i.e. $\psi_\infty^2 = n_s^* = \frac{n_s}{2}$ and the mass of Cooper pairs (m^*) is twice of the normal electron mass (m_e), i.e $m^* = 2m_e$. The superconducting current J_S of the thin wire can be written as [1]

$$J_S = -\frac{2e}{m^*}\psi_\infty^2\left(\hbar\nabla\psi - \frac{2e}{c}\mathbf{A}\right) = 2e\left|\psi\right|^2 v_s \tag{A-1}$$

where c is the light speed in vacuum, $\left|\psi\right|^2$ is the effective Cooper pair density and has the relation $\left|\psi\right|^2 = \psi_\infty^2\left[1 - \left(\frac{\xi m^* v_s^2}{\hbar}\right)^2\right]$, and v_s is the speed of Cooper pairs. $\mathbf{A}$ is the magnetic potential. Note here we assume the magnetic field is weak, and it only acts as a small macroscopic perturbation to the entire superconducting ensemble. This assumption is more valid in the meander line structure because the dc current in the adjacent lines has opposite current direction. The static magnetic field induced by dc current cancels each other. Therefore, in the rest of derivations, we ignore the contribution from the term $\mathbf{A}$.

In order to find the maximum macroscopic velocity (v_m) of Cooper pairs when the superconducting current density reaches its critical value, i.e J_c, we start with the relation

$$\frac{\partial J_S}{\partial v_s} = 0 \tag{A-2}$$

After the maximum velocity has been obtained via (A-2), the superconducting current density can be rewritten in terms of v_m as

$$J_S = -2e\psi_\infty^2 \left(1 - \frac{v_s^2}{v_m^2}\right) v_s \tag{A-3}$$

Since the critical current density of the superconducting material (e.g. NbN) in the detector was process dependant, it is better to measure the current as the ratio to its critical current density at the given material. Therefore, we denote this ratio as

$$\beta = \frac{J_S}{J_c} = \frac{3}{2}\left(1 - \frac{v_s^2}{3v_m^2}\right)\frac{v_s}{v_m} \tag{A-4}$$

For the simplicity in the future calculation, we introduce a parameter χ to be the ratio of $\frac{v_s}{v_m}$, so (A-4) can be rewritten as

$$\beta = \frac{3}{2}\left[1 - \frac{\chi^2}{3}\right]\chi \tag{A-5}$$

The relation between χ and β can be solved analytically via (A-5), i.e $\chi(\beta)$. Thus, the kinetic inductivity Λ_k can be expressed in terms of β as

$$\Lambda_k(\beta) = \frac{m_e}{e^2 n_s^T \left(1 - \chi^2(\beta)\right)} \tag{A-6}$$

where m_e is the mass of the normal electron (9.1×10^{-31}) kg, the initial Cooper pair density without bias current n_s^T can be written as a function of temperature T

$$n_s^T = \frac{m_e}{2\mu_0 e^2 \lambda_L^2}\left[1 - \left(\frac{T}{T_c}\right)^{\alpha_0}\right] \tag{A-7}$$

in which λ_L is the London penetration depth, T_c is the critical temperature, α_0 is the temperature exponential and usually has the value of 4 for low temperature superconductors, e.g. NbN; μ_0 is permeability of free-space$(= 4\pi \times 10^{-7}\ H \cdot m^{-1})$.

The total kinetic inductance L_k over a segment of superconducting wire is stemming from the inertia of superconducting carriers. It can be expressed as

$$L_k(\beta) = \Lambda_k(\beta)\left(\frac{l}{wd}\right) \tag{A-8}$$

Fig. A-1 shows an the normalized kinetic inductance of a superconducting line, under different ratio (β) of the bias current to its critical current, $0 <= \beta <= 0.991$

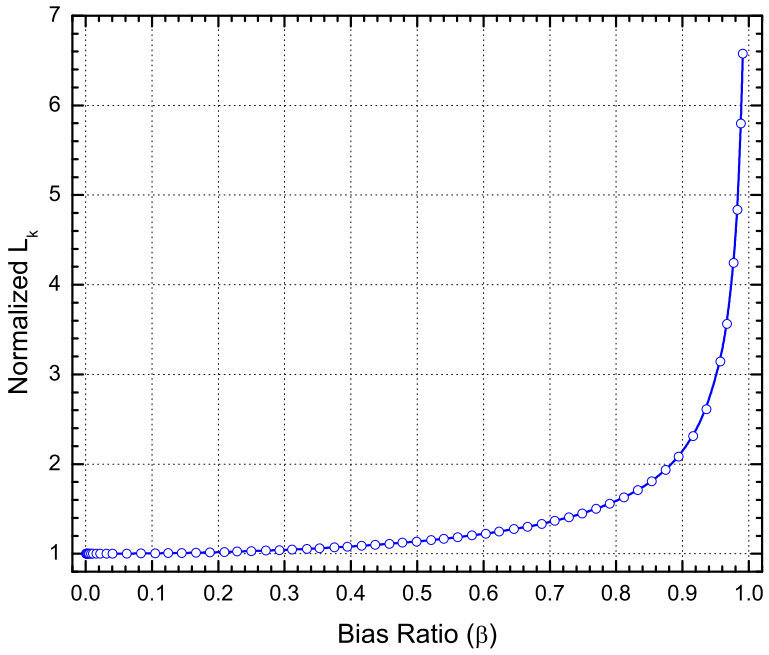

Figure A-1: The normalized kinetic inductance $L_k(\beta)$ to that of zero bias $L_k(0)$, β is the relative bias current as a ratio to that of bulk critical currentI_c.

in the plot. The maximum value of the kinetic inductance can be obtained by quasi-asymptotic method provided that the bias current always smaller than the critical current, i.e by setting both conditions $\beta \approx 1$ and $\beta < 1$ be true.

After the discussing of the kinetic inductance with respect to the different bias current density. Eq. (A-9) illustrates the output voltage being measured by virtue of the time variation of magnetic energy stored in the total inductance, which includes in the contribution from both superconducting kinetic inductance (L_k) and normal magnetic inductance (L_m) as

$$V_s(t) = \frac{\partial}{\partial t}\left[\left(L_m + L_k\right) i_b\right] \tag{A-9}$$

where i_b is the bias current and close to its critical current I_c.

Since the detector is biased at the constant current density, we can assume $L_m\left(\frac{\partial}{\partial t} i_b\right) = 0$. In addition, the magnetic inductance term L_m is determined by the geometrical parameters of the meander line as well as the mutual current flowing

directions along the adjutant meander lines. we have measured it in the room temperature and it is less than 1 nH, considerably smaller than L_k. It is basically a constant with respect to time varying. We can also have $\frac{\partial}{\partial t}(L_m I_b) = 0$. Therefore, (A-9) can be reduced to

$$V_s(t) = i_b \left(\frac{l}{Wd}\right) \frac{\delta L_k(\beta)}{\delta t} \tag{A-10}$$

where $\delta L_k(\beta)$ is the kinetic inductance variation from the initial state determined by the bias current via equation (A-6) to its maximum value as shown in the Fig. A-1. By assuming $\beta(t_0 + \delta t) \approx 1$, the kinetic inductance variation time δt is also a function of the bias current ratio β. It will be discussed in Appendix B.

B Time Delay of Superconducting Energy Gap Relaxation

In order to find the induced voltage by the time varying of kinetic inductance(see Eq. A-10), we need to find the the time delay δt during the kinetic inductance change δL_k from the initial value to the maximum inductance as shown in Fig. A-1 by the incident photon wave. Zhang *et. al* [148], [149] had the experiments on the delay time associated with the relaxation time constant of non-equilibrium superconducting state when normal electrons are injected by external current bias.

However, we assume that the bias current ratio is always lower than unity. Thus we envision a modified equation to evaluate kinetic inductance variation time δt . We associate this time variation with the time required when the energy gap Δ_0 reduces to zero with respect to the dc bias current ratio β as

$$\delta t = 2\tau_d \int_0^1 \frac{x^4}{\frac{3\sqrt{3}}{2}\beta^2 + x^6 - x^4} dx \tag{B-1}$$

in which τ_d is the superconducting energy gap relaxation time and can be evaluated as

$$\tau_d = \frac{2.41\tau_\Delta}{\sqrt{1 - \frac{T}{T_c}}} \tag{B-2}$$

where τ_Δ is the inelastic electron-phonon collision time.

Fig. B-1 shows the calculated plot of the delay time of band gap relaxation to the incident laser pulse excitation. As we can see from the figure, higher bias current reduces the total time delay. This can be justified by noting that higher bias current corresponding to higher kinetic energy of the Cooper pairs and lower paired electron density predicted by (A-4). Thus the transition into normal electron state from superconducting state becomes easier and faster than that in lower dc bias current cases.

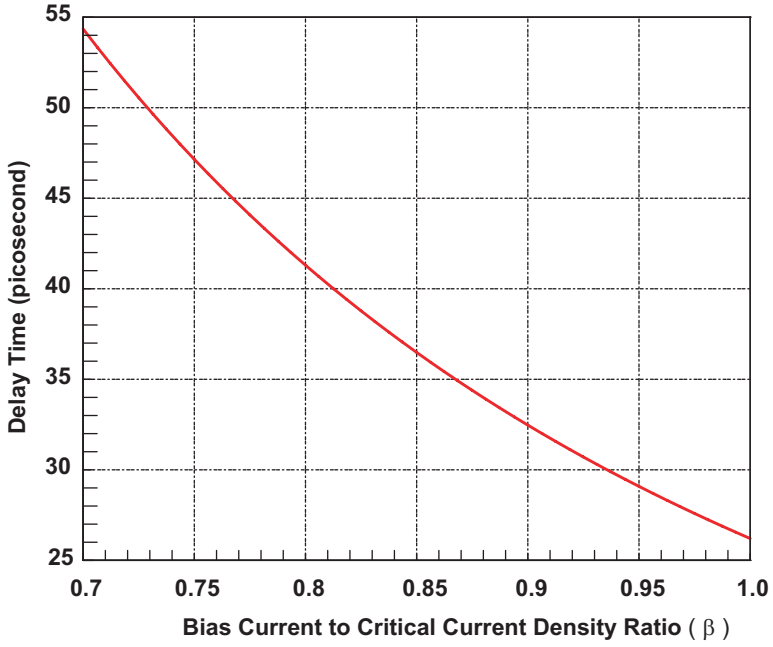

Figure B-1: The time delay (δt) for the changing of the superconductivity in response to the incident photon excitation under different bias current conditions.

C Transmission Line Effect in the Time Domain

A general model to simulate the experimental configuration (illustrated in Fig. 4.2) requires not only to consider the nonlinear load [150] of the TL (the equivalent circuit for this load is demonstrated by Fig. 4.1), but also time varying TL effect induced by the external perturbations to its characteristic impedance. The time varying TL effect can be either linear or nonlinear [151], and often requires time domain analysis [152]-[158]. The time varying TL effect has be exploited in refs [159] and [160], in which the linear time varying TL effect have been proposed to make sensors.

Schutt-Aine *et al.* [161] studied the complete time varying model for a TL and its two loads at both ends. Both loads are also excited by an RF source separately. Their mathematical relations form a general framework for our circuit model with some simplifications being made: First, we mainly focus on the nonlinear load of an ideal TL with 50 Ω characteristic impedance. Second, the other end of the TL is assumed to be perfectly matched; Lastly, we assume that the TL and all of the interconnection components, except for the nonlinear load, are time invariant.

These assumptions are valid given the facts that, (1) the cryogenic cable is coaxial type. Hence, only TEM mode electromagnetic wave is supported by such cable. All of the measurement equipment and interconnection components are chosen for 50 Ω only; (2) The EM interference from the environment is negligible by careful EMI design of our setup [1]; (3) No electromagnetic energy is coupled to any point of the TL and interconnections. By these idealizing attempts, we are able to write the time domain two-port TL S-parameter matrix $S_{TL}(t)$ to be

$$S_{TL}(t) = \begin{bmatrix} S_{11}(t) & S_{12}(t) \\ S_{21}(t) & S_{22}(t) \end{bmatrix} = \begin{bmatrix} 0 & \delta(t-t_0) \\ \delta(t-t_0) & 0 \end{bmatrix}$$

where $\delta(t-t_0)$ is the Dirac Delta function; $t_0 = \frac{L_{TL}}{v_{ph}}$ is the phase delay due to the finite length of the TL L_{TL}; and v_{ph} is the phase velocity of TEM mode wave

[1] For technical details about our EMI design, readers can refer to chapter 2.

propagating along the TL. So the time domain reflection $b_1(t)$ measured by a 50Ω equipment based on the simplified relation in [161] (we adopt the same symbolic definition as used in this reference) can be expressed like

$$b_1(t) = S_{12}(t) * \{\Gamma_2(t)[S_{21}(t) * g_1(t)]\} = \delta(t-t_0) * \{\Gamma_2(t)[\delta(t-t_0) * g_1(t)]\}$$

in which $g_1(t)$ is the input power from source; and "*" represents the convolutional integration. Consider the transient reflection from the TL load port, denoted as $\Gamma_2(t)$, only valid when $t > t_0$ due to the energy casuality; and manipulate the time frame reference. The steady state $b_1(t)$ can be rewritten as

$$b_1(t) = \delta(t-t_0) * [\Gamma(t) V_i(t)]$$

where $V_i(t) = g_1(t-t_0)$ is the time delayed input signal from the source; and $\Gamma(t) = \Gamma_2(t) h(t-t_0)$ in which $h(t-t_0)$ is the Heaviside function.

We merely use single frequency sinusoidal signal; and our goal is to measure and simulate the reflected power spectrum induced by the input RF power. The phase information of the reflected signal with respect to that of the input is beyond the scope of our interest. The time delay only modifies the phase of a sinusoidal function, but does not change the its amplitude and period. The input and output spectra of the measurements are only discrete single frequencies.

Therefore, we can calculate the reflected voltage in the time domain from the nonlinear load point, and ignore the transmission line effect explicitly. Note when no directional coupler is employed to separate the reflected signal from the incident one, the TL effect can lead to a slight amplitude inaccuracy for the fundamental tone, but have no effect on all of the higher orders of the harmonics. This is advantageous for the construction of our circuit model, because the reflected fundamental tone is many magnitudes lower than the input RF signal; and it is primarily a linear effect from the superconducting nanowire.

References

[1] M. Tinkham, *Introduction to superconductivity*, New York: McGraw Hill, 1996. sec. 1.1, 4.4 and 10.1.

[2] Bardeen, L. N. Cooper and J. R. Schrieffer, "Theory of superconductivity," *Physical Review*, vol. 108, pp. 1175-1203, 1957.

[3] P. L. Richards and Tek-Ming Shen, "Superconductive devices for millimeter wave detection, mixing, and amplification," *IEEE Trans. Electron Devices*, vol. 27, pp. 1909-1920, 1980.

[4] T. Van Duzer, "Josephson digital devices and circuits," *IEEE Trans. Microwave Theory Tech.*, vol. MTT-28, pp. 490-500, 05. 1980.

[5] B. D. Josephson, "Supercurrents through barriers," *Adv. Phys.*, vol. 14, pp. 419-451, 1965.

[6] K. K. Likharev and V. K. Semenov, "RSFQ logic/memory family: a new Josephson-junction technology for sub-terahertz-clock-frequency digital systems," *Applied Superconductivity, IEEE Transactions on*, vol. 1, pp. 3-28, 1991.

[7] S. Wuensch, E. Crocoll, M. Schubert, G. Wende, H. -. Meyer and M. Siegel, "Design and development of a cryogenic semiconductor amplifier for interfacing RSFQ circuits at 4.2 K," *Supercond Sci Technol*, vol. 20, pp. 356-61, 11. 2007.

[8] A. Lupascu, E. F. C. Driessen, L. Roschier, C. J. P. M. Harmans and J. E. Mooij, "High-contrast dispersive readout of a superconducting flux qubit using a nonlinear resonator," *Phys. Rev. Lett.*, vol. 96, pp. 127003-1, 03/31. 2006.

[9] M. Wenin, R. Roloff and W. Potz, "Robust control of Josephson charge qubits," *J. Appl. Phys.*, vol. 105, pp. 084504 (7 pp.), 04/15. 2009.

[10] J. M. Martinis, S. Nam, J. Aumentado and C. Urbina, "Rabi Oscillations in a Large Josephson-Junction Qubit," *Phys. Rev. Lett.*, vol. 89, pp. 117901, 2002.

[11] J. Martinis, "Superconducting phase qubits," *Quantum Information Processing*, vol. 8, pp. 81-103, 06/01. 2009.

[12] F. W. Strauch and C. J. Williams, "Theoretical analysis of perfect quantum state transfer with superconducting qubits," *Physical Review B*, vol. 78, pp. 094516, 2008.

[13] B. Mao, W. Qiu and S. Han, "Measurement of integrated low frequency flux noise in superconducting flux/phase qubits," *in Solid-State Quantum Computing, 2008*, pp. 22-5.

[14] E. M. Tolkacheva, D. V. Balashov, M. I. Khabipov and A. B. Zorin, "Single flux quantum circuits with damping based on dissipative transmission lines," *Supercond Sci Technol*, vol. 21, pp. 125010 (6 pp.), 12. 2008.

[15] H. Kanter and A. H. Silver, "Self-pumped Josephson parametric amplification," *Appl. Phys. Lett.*, vol. 19, pp. 515-17, 1971.

[16] A. N. Vystavkin, V. N. Gubankov, L. S. Kuzmin, K. K. Licharev and V. V. Migulin, "On microwave parametric interactions in josephson junctions," *in Proceedings of the 3rd Biennial Cornell Electrical Engineering Conference on High Frequency Generation and Amplification Devices and Application*, pp. 315-24, 1971.

[17] M. J. Feldman, P. T. Parrish and R. Y. Chiao, "Parametric amplification by unbiased Josephson junctions," *J. Appl. Phys.*, vol. 46, pp. 4031-42, 1975.

[18] H. K. Olsson and T. Claeson, "Low-noise Josephson parametric amplification and oscillations at 9 GHz," *J. Appl. Phys.*, vol. 64, pp. 5234-43, 1988.

[19] B. Yurke, M. L. Roukes, R. Movshovich and A. N. Pargellis, "A low-noise series-array Josephson junction parametric amplifier," *Appl. Phys. Lett.*, vol. 69, pp. 3078-80, 1996.

[20] M. A. Castellanos-Beltran and K. W. Lehnert, "Widely tunable parametric amplifier based on a superconducting quantum interference device array resonator," *Appl. Phys. Lett.*, vol. 91, pp. 083509-1, 08/20. 2007.

[21] P. L. Richards and Tek-Ming Shen, "Superconductive devices for millimeter wave detection, mixing, and amplification," *Electron Devices, IEEE Transactions on*, vol. 27, pp. 1909-1920, 1980.

[22] A. D. Semenov, G. N. Gol'tsman and R. Sobolewski, "Hot-electron effect in superconductors and its applications for radiation sensors," *Supercond Sci Technol*, vol. 15, pp. 1-16, 04/. 2002.

[23] R. Tucker and M. J. Feldman, "Quantum detection at millimeter wavelengths," *Reviews of Modern Physics*, vol. 57, pp. 1055-113, 10. 1985.

[24] J. Clarke, G. I. Hoffer, P. L. Richards and N. -. Yeh, "Superconductive bolometers for submillimeter wavelengths," *J. Appl. Phys.*, vol. 48, pp. 4865-4879, 1977.

[25] P. L. Richards, "Bolometers for infrared and millimeter waves," *J. Appl. Phys.*, vol. 76, pp. 1-24, 1994.

[26] A. T. Lee, P. L. Richards, Sae Woo Nam, B. Cabrera and K. D. Irwin, "A superconducting bolometer with strong electrothermal feedback," *Appl. Phys. Lett.*, vol. 69, pp. 1801-3, 1996.

[27] A. Bezryadin, C. N. Lau and M. Tinkham, "Quantum suppression of superconductivity in ultrathin nanowires," Nature, vol. 404, pp. 971-4, 2000.

[28] G.N. Gol'tsman, O. Okunev, G. Chulkova, A. Lipatov, A. Semenov, K. Smirnov, B. Voronov, A. Dzardanov, C. Williams and R. Sobolewski, "Picosecond superconducting single-photon optical detector," *Appl. Phys. Lett.*, vol. 79, pp. 705-707, 2001.

[29] A.D. Semenov, G.N. Gol'tsman and A. Korneev, "Quantum detection by current carrying superconducting film," *Physica C: Superconductivity*, vol. 351, pp. 349-356, 2001.

[30] G. Gol'tsman, O. Minaeva, A. Korneev, M. Tarkhov, I. Rubtsova, A. Divochiy, I. Milostnaya, G. Chulkova, N. Kaurova, B. Voronov, D. Pan, J. Kitaygorsky, A. Cross, A. Pearlman, I. Komissarov, W. Slysz, M. Wegrzecki, P. Grabiec and R. Sobolewski, "Middle-Infrared to Visible-Light Ultrafast Superconducting Single-Photon Detectors," *IEEE Trans. Appl. Supercond.*, vol. 17, pp. 246-251, 2007.

[31] G.N. Gol'tsman, K. Smirnov, P.Kouminov, B.Voronov, N. Kaurova, V. Drakinsky, J. Zhang,A.Verevkin, and Roman Sobolewski, "Fabrication of Nanostructured Superconducting Single-Photon Detectors," *IEEE Trans. on Appl. Supercond.*, vol. 13, pp. 192-195, June. 2003.

[32] K. W. Yang, E. Dauler, A. Ferri, A. Pearlman, A. Verevkin, G. Gol'tsman, B. Voronov, R. Sobolewski, W. E. Keicher and K. K. Berggren, "Fabrication development for nanowire GHz-counting-rate single-photon detectors," *IEEE Trans. Appl. Supercond.*, vol. 15, pp. 626-630, 2005.

[33] C. H. Bennett, F. Bessette, G. Brassard, L. Salvail and J. Smolin, "Experimental quantum cryptography," *J. Cryptol.*, vol. 5, pp. 3-28, 1992.

[34] L. Coiace, G. Masini, F. Galluzzi, G. Assanto, G. Capellini, L. Di Gaspare, E. Palange and F. Evangelisti, "Metal-semiconductor-metal near infrared light detector based on epitaxial Ge on Si," in *Proceedings of the 1998 International Symposium on Information Theory, CLEO/EUROPE'98*, Sep 14-18 1998, pp. 134.

[35] J.H.J. de Bruijne, A.P. Reynolds, M.A.C. Perryman, F. Favata and A. Peacock, "Analysis of astronomical data from optical superconducting tunnel junctions," *Opt. Eng.*, vol. 41, pp. 1158-1169, June 2002.

[36] W. Becker, A. Bergmann, G. Biscotti and A. Ruck, "Advanced time-correlated single photon counting technique for spectroscopy and imaging in biomedical systems," *in Commercial and Biomedical Applications of Ultrafast Lasers IV, Jan 27-29 2004*, 2004, pp. 104-112.

[37] T. Isoshima, Y. Isojima, K. Hakomori, K. Kikuchi, K. Nagai and H. Nakagawa, "Ultrahigh sensitivity single-photon detector using a Si avalanche photodiode for the measurement of ultraweak biochemiluminescence," *Rev. Sci. Instrum.*, vol. 66, pp. 2922-2926, 1995.

[38] A. Korneev, A. Lipatov, O. Okunev, G. Chulkova, K. Smirnov, G. Gol'tsman, J. Zhang, W. Slysz, A. Verevkin and R. Sobolewski, "GHz counting rate NbN single-photon detector for IR diagnostics of VLSI CMOS circuits," *Microelectronic Engineering*, vol. 69, pp. 274-278, September, 2003.

[39] A. Lipatov, O. Okunev, K. Smirnov, G. Chulkova, A. Korneev, P. Kouminov, G. Gol'tsman, J. Zhang, W. Slysz, A. Verevkin and R. Sobolewski, "An ultrafast NbN hot-electron single-photon detector for electronic applications," *Superconductor Science and Technology*, vol. 15, pp. 1689-1692, 2002.

[40] B. S. Robinson, A. J. Kerman, E. A. Dauler, R. J. Barron, D. O. Caplan, M. L. Stevens, J. J. Carney, S. A. Hamilton, J. K. W. Yang and K. K. Berggren, "781 Mbit/s photon-counting optical communications using a superconducting nanowire detector," *Opt. Lett.*, vol. 31, pp. 444-446, 2006.

[41] Alexei Trifonov, Darius Subacius, Audrius Berzanskis and Anton Zavriyev, "Single Photon Counting at Telecom Wavelength and Quantum Key Distribution," *J. of Modern Optics*, vol. 51, pp. 1399-1415, June–July. 2004.

[42] A. Pearlman, A. Cross, W. Slysz, J. Zhang, A. Verevkin, M. Currie, A. Korneev, P. Kouminov, K. Smirnov, B. Voronov, G. Gol'tsman and R. Sobolewski, "Gigahertz counting rates of NbN single-photon detectors for quantum communications," *IEEE Trans. Appl. Supercond.*, vol. 15, pp. 579-82, June, 2005.

[43] Boileau, R. Laflamme, M. Laforest and C. R. Myers, "Robust Quantum Communication Using a Polarization-Entangled Photon Pair," *Phys. Rev. Lett.*, vol. 93, pp. 220501, November 26, 2004.

[44] B. Cabrera, R. M. Clarke, P. Colling, A. J. Miller, S. Nam and R. W. Romani, "Detection of single infrared, optical, and ultraviolet photons using superconducting transition edge sensors," *Appl. Phys. Lett.*, vol. 73, pp. 735-7, 08/10. 1998.

[45] A. J. Miller, S. W. Nam, J. M. Martinis and A. V. Sergienko, "Demonstration of a low-noise near-infrared photon counter with multiphoton discrimination," *Appl. Phys. Lett.*, vol. 83, pp. 791-793, 2003.

[46] L. Hao, J.C. Gallop, C. Gardiner, P. Josephs-Franks, J.C. Macfarlane, S.K.H. Lam and C. Foley, "Inductive superconducting transition-edge detector for single-photon and macro-molecule detection," *Supercond Sci Technol*, pp. 1479-1482, 2003.

[47] E. N. Grossman, D. G. McDonald and J. E. Sauvageau, "Far-infrared kinetic-inductance detectors," *IEEE Trans. Magn.*, vol. 27, pp. 2677-2680, 1991.

[48] C. M. Bridge, M. Cropper, G. Ramsay, M. A. C. Perryman, J. H. J. de Bruijne, F. Favata, A. Peacock, N. Rando and A. P. Reynolds, "STJ observations of the eclipsing polar HU Aqr," *Monthly Notices of the Royal Astronomical Society*, vol. 336, pp. 1129-38, 11/11. 2002.

[49] J. H. J. De Bruijne, A. P. Reynolds, M. A. C. Perryman, F. Favata and A. Peacock, "Analysis of astronomical data from optical superconducting tunnel junctions," *Optical Engineering*, vol. 41, pp. 1158-1169, 2002.

[50] I. Prochazka, "Semiconducting single photon detectors: The state of the art," *in NATO Advanced Research Workshop Advanced Materials for Radiation Detectors and Sensors: Wide-Gap Semiconductors and Superconductors and E-MRS 2004 Fall Meeting Symposium E, 6-10 Sept. 2004*, 2005, pp. 1524-32.

[51] R. Sobolewski, A. Verevkin, G.N. Gol'tsman, A. Lipatov and K. Wilsher, "Ultrafast Superconducting Single-Photon Optical Detectors and their Applications," *IEEE Trans. Appl. Supercond.*, vol. 13, pp. 1151-1157, June. 2003.

[52] K. M. Rosfjord, J. K. W. Yang, E. A. Dauler, A. J. Kerman, V. Anant, B. M. Voronov, G. N. Gol'tsman and K. K. Berggren, "Nanowire Single-photon detector with an integrated optical cavity and anti-reflection coating," *Optics Express*, vol. 14, pp. 527-534, 2006.

[53] A. Engel, A. Semenov, H. Hubers, K. Ilin and M. Siegel, "Dark counts of a superconducting single-photon detector," *Nuclear Instruments & Methods in Physics Research, Section A (Accelerators, Spectrometers, Detectors and Associated Equipment)*, vol. 520, pp. 32-5, 03/11. 2004.

[54] A. Engel, A. Semenov, H. Hubers, K. Il'in and M. Siegel, "Superconducting single-photon detector for the visible and infrared spectral range," *J. of Modern Optics*, vol. 51, pp. 1459-1466, 2004.

[55] Xiaolong Hu, C. W. Holzwarth, D. Masciarelli, E. A. Dauler and K. K. Berggren, "Efficiently Coupling Light to Superconducting Nanowire Single-Photon Detectors," *IEEE Trans. Appl. Supercond.*, vol. 19; pp. 336-340, 2009.

[56] E. A. Dauler, A. J. Kerman, B. S. Robinson, J. K. W. Yang, B. Voronov, G. Goltsman, S. A. Hamilton and K. K. Berggren, "Photon-number-resolution with sub-30-ps timing using multi-element superconducting nanowire single photon detectors," *Journal of Modern Optics*, vol. 56, pp. 364, 2009.

[57] F. Marsili, D. Bitauld, A. Fiore, A. Gaggero, R. Leoni, F. Mattioli, A. Divochiy, A. Korneev, V. Seleznev, N. Kaurova, O. Minaeva and G. Goltsman, "Superconducting parallel nanowire detector with photon number resolving functionality," *Journal of Modern Optics*, vol. 56, pp. 334, 2009.

[58] S. Miki, M. Fujiwara, M. Sasaki and Z. Wang, "NbN superconducting single-photon detectors prepared on single-crystal MgO substrates," IEEE Trans. Appl. Supercond., vol. 17, pp. 285-288, 2007.

[59] S. Miki, M. Fujiwara, M. Sasaki, B. Baek, A. J. Miller, R. H. Hadfield, S. W. Nam and Z. Wang, "Large sensitive-area NbN nanowire superconducting single-photon detectors fabricated on single-crystal MgO substrates," *Appl. Phys. Lett.*, vol. 92, pp. 061116, 2008.

[60] M. Tarkhov, J. Claudon, J. P. Poizat, A. Korneev, A. Divochiy, O. Minaeva, V. Seleznev, N. Kaurova, B. Voronov, A. V. Semenov and G. Gol'tsman, "Ultrafast reset time of superconducting single photon detectors," *Appl. Phys. Lett.*, vol. 92, pp. 241112-3, 06/16. 2008.

[61] M. J. Stevens, R. H. Hadfield, T. Gerrits, T. S. Clement, R. P. Mirin and S. W. Nam, "Infrared wavelength-dependent optical characterization of NbN nanowire superconducting single-photon detectors," *Journal of Modern Optics*, vol. 56, pp. 358, 2009.

[62] G.N. Gol'tsman, A. Korneev, I. Rubtsova, I. Milostnaya, G. Chulkova, O. Minaeva, K. Smirnov, B. Voronov, W. Slysz, A. Pearlman, A. Verevkin and R. Sobolewski, "Ultrafast superconducting single-photon detectors for near-infrared-wavelength quantum communications," *Physica Status Solidi C*, pp. 1480-8, 2005.

[63] A. J. Kerman, E. A. Dauler, J. K. W. Yang, K. M. Rosfjord, V. Anant, K. K. Berggren, G. N. Gol'tsman and B. M. Voronov, "Constriction-limited detection efficiency of superconducting nanowire single-photon detectors," *Appl. Phys. Lett.*, vol. 90, pp. 101110, 5 March 2007.

[64] J. K. W. Yang, A. J. Kerman, E. A. Dauler, B. Cord, V. Anant, R. J. Molnar and K. K. Berggren, "Suppressed Critical Current in Superconducting Nanowire Single-Photon Detectors With High Fill-Factors," *IEEE Trans. Appl. Supercond.*, vol. 19; pp. 318-322, 2009.

[65] R. H. Hadfield, P. A. Dalgarno, J. A. O'Connor, E. Ramsay, R. J. Warburton, E. J. Gansen, B. Baek, M. J. Stevens, R. P. Mirin and S. W. Nam, "Sub-micrometer photoresponse mapping of nanowire superconducting single-photon detectors," *Appl. Phys. Lett.*, vol. 91, pp. 241108, 10 December 2007.

[66] M. J. Stevens, R. H. Hadfield, R. E. Schwall, Sae Woo Nam and R. P. Mirin, "Quantum dot single photon sources studied with superconducting single photon detectors," *IEEE Journal of Selected Topics in Quantum Electronics*, vol. 12, pp. 1255-68, 11. 2006.

[67] C. Liang, K. F. Lee, M. Medic, P. Kumar, R. H. Hadfield and S. W. Nam, "Characterization of fiber-generated entangled photon pairs with superconducting single-photon detectors," *Optics Express*, vol. 15, pp. 1322-1327, 2007.

[68] R. J. Collins, R. H. Hadfield, V. Fernandez, S. W. Nam and G. S. Buller, "Low timing jitter detector for gigahertz quantum key distribution," *Electron. Lett.*, vol. 43, pp. 180-182, 2007.

[69] R. H. Hadfield, J. L. Habif, J. Schlafer, R. E. Schwall and Sae Woo Nam, "Quantum key distribution at 1550 nm with twin superconducting single-photon detectors," *Appl. Phys. Lett.*, vol. 89, pp. 241129-1, 2006.

[70] B. S. Robinson, A. J. Kerman, E. A. Dauler, R. J. Barron, D. O. Caplan, M. L. Stevens, J. J. Carney, S. A. Hamilton, J. K. W. Yang and K. K. Berggren, "781 Mbit/s photon-counting optical communications using a superconducting nanowire detector," *Opt. Lett.*, vol. 31, pp. 444-446, 2006.

[71] J. Kitaygorsky, J. Zhang, A. Verevkin, A. Sergeev, A. Korneev, V. Matvienko, P. Kouminov, K. Smirnov, B. Voronov, G. Gol'tsman and R. Sobolewski, "Origin of dark counts in nanostructured NbN single-photon detectors," *IEEE Trans.Appl.Supercond.*, vol. 15, pp. 545-8, 06, 2005.

[72] A. Semenov, A. Engel, H. Hubers, K. Il'in and M. Siegel, "Spectral cut-off in the efficiency of the resistive state formation caused by absorption of a single-

photon in current-carrying superconducting nano-strips," *European Physical Journal B*, vol. 47, pp. 495-501, 2005.

[73] J. S. Langer and V. Ambegaokar, "Intrinsic Resistive Transition in Narrow Superconducting Channels," *Phys. Rev.*, vol. 164, pp. 498-510, Dec. 1967.

[74] C. N. Lau, N. Markovic, M. Bockrath, A. Bezryadin and M. Tinkham, "Quantum phase slips in superconducting nanowires," *Phys. Rev. Lett.*, vol. 87, pp. 217003-1, 11/19. 2001.

[75] W. J. Skocpol, M. R. Beasley and M. Tinkham, "Self-heating hotspots in superconducting thin-film microbridges," *J. Appl. Phys.*, vol. 45, pp. 4054-66, 1974.

[76] M. W. Johnson, A. M. Herr and A. M. Kadin, "Bolometric and nonbolometric infrared photoresponses in ultrathin superconducting NbN films," *J. Appl. Phys.*, vol. 79, pp. 7069-7074, May 1, 1996.

[77] R. Leoni, A. Gaggero, F. Mattioli, M. Castellano, P. Carelli, F. Marsili, D. Bitauld, M. Benkahoul, F. Lévy and A. Fiore, "Characterization of Superconducting Single Photon Detectors Fabricated on MgO Substrates," *J. Low Temp. Phys.*, vol. Volume 151, pp. 580-584, 2008.

[78] Z. Yan, A. H. Majedi and S. Safavi-Naeini, "Physical Modeling of Hot-Electron Superconducting Single-Photon Detectors," *Applied Superconductivity, IEEE Transactions on*, vol. 17, pp. 3789-3794, 2007.

[79] R. H. Parmenter, "Nonlinear electrodynamics of superconductors with a very small coherence distance," *RCA Review*, vol. 23, pp. 323-352, 1962.

[80] J. Halbritter, "rf residual losses, surface impedance, and granularity in superconducting cuprates," *J. Appl. Phys.*, vol. 68, pp. 6315-6326, 12/15. 1990.

[81] M. A. Golosovsky, H. J. Snortland and M. R. Beasley, "Nonlinear microwave properties of superconducting Nb microstrip resonators," *Phys. Rev. B*, vol. 51, pp. 6462, 03/01. 1995.

[82] B. Abdo, E. Segev, O. Shtempluck and E. Buks, "Unusual nonlinear dynamics observed in NbN superconducting microwave resonators," *Journal of Physics: Conference Series*, vol. 43, pp. 1346-9, 2006.

[83] E. Segev, B. Abdo, O. Shtempluck and E. Buks, "Extreme nonlinear phenomena in NbN superconducting stripline resonators," *Physics Letters A*, vol. 366, pp. 160-4, 06/18. 2007.

[84] J. C. Booth, K. Leong, S. A. Schima, J. A. Jargon, D. C. DeGroot and R. Schwall, "Phase-sensitive measurements of nonlinearity in high-temperature superconductor thin films," *Applied Superconductivity, IEEE Transactions on*, vol. 15, pp. 1000-1003, 2005.

[85] B. Abdo, E. Arbel-Segev, O. Shtempluck and E. Buks, "Observation of bifurcations and hysteresis in nonlinear NbN superconducting microwave resonators," *IEEE Trans. Appl. Supercond.*, vol. 16, pp. 1976-87, 12. 2006.

[86] A. J. Kerman, E. A. Dauler, W. E. Keicher, J. K. W. Yang, K. K. Berggren, G. Gol'tsman and B. Voronov, "Kinetic-inductance-limited reset time of superconducting nanowire photon counters," *Appl. Phys. Lett.*, vol. 88, pp. 111116, 13 March 2006. 2006.

[87] B. Abdo, E. Segev, O. Shtempluck and E. Buks, "Signal amplification in NbN superconducting resonators via stochastic resonance," *Physics Letters* A, vol. 370, pp. 449-53, 10/29. 2007.

[88] A. D. Semenov, P. Haas, B. Gnther, H. -. Hbers, K. Il'in, M. Siegel, A. Kirste, J. Beyer, D. Drung, T. Schurig and A. Smirnov, "An energy-resolving superconducting nanowire photon counter," *Superconductor Science and Technology*, vol. 20, pp. 919-924, 2007.

[89] J. K. W. 1. Yang, A. J. Kerman, E. A. Dauler, V. Anant, K. M. Rosfjord and K. K. Berggren, "Modeling the electrical and thermal response of superconducting

nanowire single-photon detectors," *IEEE Trans. Appl. Supercond.*, vol. 17, pp. 581-5, 06. 2007.

[90] M. Tinkham, J. U. Free, C. N. Lau and N. Markovic, "Hysteretic I-V curves of superconducting nanowires," *Physical Review B*, vol. 68, pp. 134515-1, 10/01. 2003.

[91] D. M. Pozar, *Microwave Engineering*. New York ; Chichester, England: John Wiley & Sons, 1998. ch-6.

[92] K. S. Keskar, T. Yamashita, Y. Onodera, Y. Goto and T. Aso, "rf reactively sputtered superconducting NbN_x films," *Japn. J. Appl. Phys.*, vol. 45, pp. 3102-3105, 1974.

[93] Y. M. Shy, L. E. Toth and R. Somasundaram, "Superconducting properties, electrical resistivities, and structure of NbN thin films," *J. Appl. Phys.*, vol. 44, pp. 5539-5545, Dec. 1973.

[94] J. Tyan and J. T. Lue, "Grain boundary scattering in the normal state resistivity of superconducting NbN thin films," *J. Appl. Phys.*, vol. 75, pp. 325-331, January 1, 1994.

[95] R. T. Kampwirth and K. E. Gray, "NbN materials development for practical superconducting devices," *IEEE Trans. Magn.*, vol. 17, pp. 565-8, Jan. 1981.

[96] K. E. Gray, R. T. Kampwirth, D. M. Capone II and R. Vaglio, "Microscopic investigation of NbN sputtered films," *Physica B & C*, vol. 135B+C, pp. 164-7, Dec. 1985.

[97] V. Ambegaokar and A. Baratoff, "Tunneling between superconductors," *Phys. Rev. Lett.*, vol. 10, pp. 486-489, Jun. 1963.

[98] V. Ambegaokar and A. Baratoff, "Erratum: tunneling between superconductors," *Phys. Rev. Lett.*, vol. 11, pp. 104, Jul., 1963.

[99] C. C. Chin, D. E. Oates, G. Dresselhaus and M. S. Dresselhaus, "Nonlinear electrodynamics of superconducting NbN and Nb thin films at microwave frequencies," *Physical Review B (Condensed Matter)*, vol. 45, pp. 4788-98, 03/01. 1992.

[100] B. Abdo, E. Segev, O. Shtempluck and E. Buks, "Nonlinear dynamics in the resonance line shape of NbN superconducting resonators," *Phys. Rev. B*, vol. 73, pp. 134513-11, 2006.

[101] B. Bonin and H. Safa, "Power dissipation at high fields in granular RF superconductivity," *Supercond Sci Technol*, vol. 4, pp. 257-61, 06. 1991.

[102] T. P. Orlando, E. J. McNiff Jr., S. Foner and M. R. Beasley, "Critical fields, Pauli paramagnetic limiting, and material parameters of Nb_3Sn and V_3Si," *Physical Review B (Condensed Matter)*, vol. 19, pp. 4545-61, 05/01. 1979.

[103] D. E. Oates, A. C. Anderson, C. C. Chin, J. S. Derov, G. Dresselhaus and M. S. Dresselhaus, "Surface-impedance measurements of superconducting NbN films," *Phys. Rev. B*, vol. 43, pp. 7655-63, 04/01. 1991.

[104] M. Lindgren, M. Currie, C. A. Williams, T. Y. Hsiang, P. M. Fauchet, R. Sobolewski, S. H. Moffat, R. A. Hughes, J. S. Preston and F. A. Hegmann, "Ultrafast photoresponse in microbridges and pulse propagation in transmission lines made from high-Tc superconducting Y-Ba-Cu-O thin films," *IEEE Journal of Selected Topics in Quantum Electronics*, vol. 2, pp. 668-78, 1996.

[105] R. H. Hadfield, A. J. Miller, S. W. Nam, R. L. Kautz and R. E. Schwall, "Low-frequency phase locking in high-inductance superconducting nanowires," *Appl. Phys. Lett.*, vol. 87, pp. 203505-1, 11/14. 2005.

[106] A. H. Majedi, S. K. Chaudhuri and S. Safavi-Naeini, "Analysis of photo-excited thin superconducting films for optoelectronic device applications," *IEEE Trans. Appl. Supercond.*, vol. 11, pp. 4095-4101, 2001.

[107] Y. Liu, J. F. Whitaker, C. Uher, S. Y. Hou and J. M. Phillips, "Pulsed terahertz-beam spectroscopy as a probe of the thermal and quantum response of $YBa_2Cu_3O_{7-\delta}$ superfluid," *Appl. Phys. Lett.*, vol. 67, pp. 3022-3024, 11/13. 1995.

[108] A. H. Majedi, S. K. Chaudhuri and S. Safavi-Naeini, "Optical-microwave interaction modeling in high-temperature superconducting films," *IEEE Trans. Microwave Theory Tech.*, vol. 49, pp. 1873-81, 10/. 2001.

[109] C.S. Owen and D. J. Scalapino, "Superconducting State under Influence of External Dynamic Pair Breaking," *Phys. Rev. Lett.*, vol. 28, pp.1559-1561, 1972.

[110] C. Bell and G. Wade, "Iterative Traveling-Wave Parametric Amplifiers," *Circuit Theory, IRE Transactions on*, vol. 7, pp. 4-11, Mar. 1960.

[111] K. P. Grabowski, "A Nondegenerate Traveling-Wave Parametric Amplifier," *Microwave Theory and Techniques, IEEE Transactions on*, vol. 10, pp. 103-107, Mar. 1962.

[112] V. Uzunoglu, "Parametric Amplification (Correspondence)," *Microwave Theory and Techniques, IEEE Transactions on*, vol. 11, pp. 211-211, May 1963.

[113] Z. Heshmati, I. C. Hunter and R. D. Pollard, "Microwave Parametric Frequency Dividers With Conversion Gain," IEEE Trans. Microwave Theory Techn., vol. 55, pp. 2059-2064, Oct. 2007.

[114] E. Segev, B. Abdo, O. Shtempluck and E. Buks, "Utilizing nonlinearity in a superconducting NbN stripline resonator for radiation detection," *IEEE Trans. Appl. Supercond.*, vol. 17, pp. 271-4, 06. 2007.

[115] E. Segev, B. Abdo, O. Shtempluck and E. Buks, "Stochastic resonance with a single metastable state: thermal instability in NbN superconducting stripline resonators," *Physical Review B*, vol. 77, pp. 012501-1, 2008.

[116] F. M. Tesche, "Development and use of the BLT equation in the time domain as applied to a coaxial cable," *IEEE Trans. Electromagn. Compat.*, vol. 49, pp. 3-11, 2007.

[117] S. Selleri and G. Pelosi, "Time-domain analysis of a transmission line closed on a lumped nonlinear load," *Microwave Opt Technol Lett*, vol. 25, pp. 367-368, 2000.

[118] R. G. Hicks and P. J. Khan, "Numerical technique for determining pumped nonlinear device waveforms," *Electron. Lett.*, vol. 16, pp. 375-6, 1980.

[119] R. G. Hicks and P. J. Khan, "Numerical analysis of nonlinear solid-state device excitation in microwave circuits," *IEEE Trans. Microwave Theory Tech.*, vol. MTT-30, pp. 251-9, 1982.

[120] S. Iezekiel, C. M. Snowden and M. J. Howes, "Harmonic balance model of laser diode," *Electron. Lett.*, vol. 25, pp. 529-30, 1989.

[121] V. Rizzoli, F. Mastri, F. Sgallari and G. Spaletta, "Harmonic-balance simulation of strongly nonlinear very large-size microwave circuits by inexact Newton methods," *Microwave Symposium Digest, 1996. , IEEE MTT-S International*, vol. 3; pp. 1357-1360, 1996.

[122] S. A. Winkler, K. Wu and A. Stelzer, "A novel hybrid analysis approach for subharmonic self-oscillating mixers combining volterra series and conversion matrix methods," *in 37th European Microwave Conference*, pp. 1413-16, 2007.

[123] A. Kheirdoost, A. Banai and F. Farzaneh, "An Analytical Approach in Analysis of Local Oscillator Near-the-Carrier AM Noise Suppression in Microwave Balanced Mixers," *Microwave Theory and Techniques, IEEE Transactions on*, vol. 57, pp. 760-766, 2009.

[124] Z. L. Yuan, B. E. Kardynal, A. W. Sharpe and A. J. Shields, "High speed single photon detection in the near infrared," *Appl. Phys. Lett.*, vol. 91, pp. 041114-1, 2007.

[125] N. Bluzer, "Analysis of quantum superconducting kinetic inductance photodetectors," *J. Appl. Phys.*, vol. 78, pp. 7340-51, 12/15. 1995.

[126] S. A. Maas, *Nonlinear Microwave and RF Circuits.* ,2nd Edition, Boston ; London: Artech House, 2003.

[127] A. H. Majedi, D. Saeedkia, S. K. Chaudhuri and S. Safavi-Naeini, "Physical modeling and frequency-response analysis of a high-temperature Superconducting terahertz photomixer," *IEEE Trans. Microwave Theory Tech.*, vol. 52, pp. 2430-7, 10/. 2004.

[128] A. H. Majedi, S. K. Chaudhuri and S. Safavi-Naeini, "Kinetic inductive model of a millimeter-wave high-temperature superconducting optoelectronic mixer," *IEEE Trans. Appl. Supercond.*, vol. 14, pp. 1974-82, 2004.

[129] Y. Taur, "Josephson-junction mixer analysis using frequency-conversion and noise-correlation matrices," *IEEE Trans. Electron Devices*, vol. ED-27, pp. 1921-8, 10. 1980.

[130] Y. Uzawa, A. Kawakami, A. Saito, M. Takeda and Z. Wang, "A submillimetre-wave SIS mixer using NbN/MgO/NbN trilayers grown epitaxially on an MgO substrate," *Supercond Sci Technol*, vol. 15, pp. 1760-1765, 2002.

[131] S. Withington, P. Kittara and G. Yassin, "Non-linear two-frequency analysis of SIS mixers through harmonic balance," in *5th European Workshop on Low Temperature Electronics, June 19, - June 21, 2002* pp. Pr3/165-Pr3/168, 2002.

[132] S. Miki, A. Kawakami, Y. Uzawa and Z. Wang, "Improvement of Phonon Diffusion Efficiency in Phonon-Cooled NbN Hot Electron Bolometer Mixers," Jpn. J. Appl. Phys., vol. 42, pp. 3383, January 2003.

[133] D. E. Prober, "Superconducting terahertz mixer using a transition-edge microbolometer," *Appl. Phys. Lett.*, vol. 62, pp. 2119-2121, April 26, 1993.

[134] A. D. Semenov, H. Hubers, H. Richter, M. Birk, M. Krocka, U. Mair, K. Smirnov, G. N. Gol'tsman and B. M. Voronov, "2.5 THz heterodyne receiver with NbN hot-electron-bolometer mixer," *in EUCAS 2001*, pp. 448-53, 2002.

[135] A. D. Semenov, G. N. Gol'tsman and R. Sobolewski, "Hot-electron effect in superconductors and its applications for radiation sensors," *Supercond Sci Technol*, vol. 15, pp. 1-16, 04. 2002.

[136] D.K.W. Lam, and R.I. Macdonald, "GaAs optoelectronic mixer operation at 4.5 GHz". *IEEE Trans. Electron Dev.*, ED-31, pp.1766-1768, 1984.

[137] H.-U., Daniel, B. Maurer, M. Steiner, and H. Walther, "Schottky diode mixer for visible laser light and microwave harmonics up to 0.43 THz," *Appl. Phys. Lett.*, vol. 41, pp. 313-315, 1982.

[138] Donald, D.K., Bloom, D.M. and David, F.K. "Efficient simple optical heterodyne receiver; DC to 80 GHz", in *Proceedings of SPIE, International Society of Optical Engineers*, vol. 545, pp. 29-34, 1985.

[139] Q.V. Davis, and W.K. Kulczyk, "Optical and electronic mixing in an avalanche photodiode", *Electron. Lett.*, vol. 6, pp. 25-26, 1970.

[140] A. Chu, H.R. Fetterman, D.D. Peck and P.E. Tannenwald, "Heterodyne experiments from millimeter wave to optical frequencies using GaAs MESFETs above f_T," in *IEEE 1982 Microwave and millimeter-wave monolithic circuits sqmp. digest.* IEEE, New York, pp. 25-27, 1982.

[141] Z. Urey, D. Wake, D. J. Newson, and I. D. Henning, "Comparison of InGaAs transistors as optoelectronic mixers," *Electron. Lett.*, vol. 29, pp. 1796-1798, 1993.

[142] Y. Betser, D. Ritter, C.-P. Liu, A. J. Seeds, and A. Madjar, "A single stage three terminal heterojunction bipolar transistor optoelectronic mixer," *J. Lightwave Technol.*, vol. 16, pp. 605-609, 1998.

[143] J. R. Tucker, "Quantum limited detection in tunnel junction mixers," *IEEE J. Quant. Electron.*, vol. QE-15, pp. 1234-58, 11. 1979.

[144] M. J. Feldman, "Some analytical and intuitive results in the quantum theory of mixing," *J. Appl. Phys.*, vol. 53, pp. 584-92, 01. 1982.

[145] S. B. Kaplan, C. C. Chi, D. N. Langenberg, J. J. Chang, S. Jafarey and D. J. Scalapino, "Quasiparticle and phonon lifetimes in superconductors," *Physical Review B (Solid State)*, vol. 14, pp. 4854-73, 12/01. 1976.

[146] M. Johnson, N. Bluzer, M. Reyzer, T. H. Geballe, S. R. Greenfield, J. J. Stankus, M. D. Fayer and C. Herring, "Photoresponse of nb films; observation of biexponential recovery times of the superconducting state," *in 1990 Applied Superconductivity Conference*, 1991, pp. 1523-7.

[147] E. Menshchikov, I. Gogidze, A. Sergeev, A. Elantev, P. Kuminov, G. Goltsman and E. Gershenzon, "Superconducting fast detector based on the nonequilibrium inductance response of a film of niobium nitride," *Technical Physics Letters*, vol. 23, pp. 486-488, 1997.

[148] Jin Zhang, W. Slysz, A. Verevkin, O. Okunev, G. Chulkova, A. Korneev, A. Lipatov, G.N. Gol'tsman and R. Sobolewski, "Response Time Characterization of NbN Superconducting Single-Photon Detectors," *IEEE Trans. on Appl. Supercond.*, vol. 13, pp. 180-183, June. 2003.

[149] J. Zhang, W. Slysz, A. Pearlman, A. Verevkin, R. Sobolewski, O. Okunev, G. Chulkova and G.N. Gol'tsman, "Time delay of resistive-state formation in superconducting stripes excited by single optical photons," *Phys. Rev. B*, vol. 67, pp. 132508, April 1, 2003.

[150] A. R. Djordjevic, T. K. Sarkar and R. F. Harrington, "Analysis of lossy transmission lines with arbitrary nonlinear terminal networks," *IEEE Trans. Microwave Theory Tech.*, vol. MTT-34, pp. 660-6, 06. 1986.

[151] D. E. Oates, P. P. Nguyen, G. Dresselhaus, M. S. Dresselhaus, C. W. Lam and S. M. Ali, "Measurements and modeling of linear and nonlinear effects in striplines," *J. Supercond.*, vol. 5, pp. 361-9, 08. 1992.

[152] A. R. Djordjevic, T. K. Sarkar and R. F. Harrington, "Time-domain response of multiconductor transmission lines," *Proc IEEE,* vol. 75, pp. 743-64, 06. 1987.

[153] T. K. Sarkar, T. Rahalarabi, R. F. Harrington and A. R. Djordjevic, "Theoretical and experimental characterization of multiconductor transmission lines," *in 1987 IEEE International Symposium on Circuits and Systems*, 1987, pp. 511-13.

[154] J. Schutt-Aine and R. Mittra, "Nonlinear transient analysis of coupled transmission lines," *IEEE Transactions on Circuits and Systems*, vol. 36, pp. 959-67, 1989.

[155] T. Dhaene, L. Martens and D. De Zutter, "Transient simulation of arbitrary nonuniform interconnection structures characterized by scattering parameters," IEEE Trans. Circuits Syst. I Fundam. Theor. Appl., vol. 39, pp. 928-37, 11. 1992.

[156] T. Dhaene, L. Martens and D. De Zutter, "Generalized iterative frequency domain deconvolution technique," *in 1993 IEEE Instrumentation and Measurement Technology Conference*, pp. 85-7, 1993.

[157] T. Dhaene, L. Martens and D. De Zutter, "Calibration and normalization of time domain network analyzer measurements," *IEEE Trans. Microwave Theory Tech.*, vol. 42, pp. 580-9, 1994.

[158] Te-Wen Pan, Ching-Wen Hsue and Jhin-Fang Huang, "Time-domain reflectometry using arbitrary incident waveforms," *IEEE Trans. Microwave Theory Tech.*, vol. 50; pp. 2558-2563, 2002.

[159] K. Green and R. Sobolewski, "Extending scattering-parameter approach to characterization of linear time-varying microwave devices," *IEEE Trans. Microwave Theory Tech.*, vol. 48, pp. 1725-1731, 2000.

[160] D. Saeedkia, A. H. Majedi, S. Safavi-Naeini and R. R. Mansour, "Frequency and time-varying scattering parameters of a photo-excited superconducting microbridge," *IEEE Microwave and Wireless Components Letters*, vol. 15, pp. 510-12, 2005.

[161] J. Schutt-Aine and R. Mittra, "Scattering parameter transient analysis of transmission lines loaded with nonlinear terminations," *IEEE Trans. Microwave Theory Tech.*, vol. 36, pp. 529-36, 1988.